ALMA MATER STUDIORUM
UNIVERSITÀ DEGLI STUDI DI BOLOGNA

Dipartimento di Fisica e Astronomia

Dottorato di ricerca in Astronomia
Ciclo XXIX

Tesi di Dottorato

COSMIC-LAB: UNDERSTANDING THE DYNAMICAL EVOLUTION OF DENSE STELLAR SYSTEMS

CANDIDATO:
Emiliano Alessandrini

RELATORE:
Barbara Lanzoni

CO-RELATORE:
Francesco Rosario Ferraro

COORDINATORE:
Francesco Rosario Ferraro

Esame finale anno 2016

Settore concorsuale: 02/C1 – Astronomia, Astrofisica, Fisica della Terra e dei Pianeti
Settore scientifico-disciplinare: FIS/05 – Astronomia e Astrofisica

Contents

Abstract

In this Thesis, we study the dynamics of blue straggler stars (BSSs) in globular clusters (GCs) by means of direct N-body simulations. These stars have a present mass $m_{\rm BSS} \simeq 1.2 M_{\odot}$ that is higher than the average star mass in a GC. For this reason, during the evolution of the host cluster, they suffer from dynamical friction (DF), which is the slowing down of a heavy particle orbiting a sea of lighter particles due to the cumulative effect of two-body interactions. This dynamical process causes the sinking of heavy objects toward the cluster centre and their segregation in the internal regions, leaving the outskirts of the cluster significantly depleted of these stars. Due to this phenomenon, BSSs are considered to be probe particles of the internal dynamics of GCs. In particular, three different shapes for the BSS normalized radial distribution (BSS-nRD) have been observed in GCs, and Ferraro et al. (2012) interpreted this feature as the probe of different dynamical evolution histories among coeval GCs. The proposed scenario is that, as the cluster evolves dynamically and BSSs migrate toward the cluster internal regions, a central peak in the radial distribution of these objects forms and grows with time, while at intermediate radii the depletion of (the migrated) BSSs causes the formation of a minimum in the distribution. As time passes, the migration toward the centre affects progressively more external BSSs, causing the growing of the central peak in their distribution and the simultaneous migration of the minimum toward larger radii. The distance of the minimum from the cluster centre is then used by Ferraro et al. (2012) as a clock hand able to provide the dynamical age of GCs, thus defining the *dynamical clock* scenario. While the proposed scenario seems to properly account for the observational data, on one side, the minimum measurements suffer from some statistical inconvenients, on the other side, appropriate N-body simulations are needed to investigate in full details the physical processes behind the clock and to provide an absolute calibration of it (in fact, at the moment this tool only allows a relative ranking of GCs in terms of their dynamical ages).

The purpose of this Thesis is to describe the processes connected to the BSS segregation in GCs, by indentifying all the ingredients that contribute in shaping the radial distribution of these objects during the dynamical evolution of the clusters. To this aim, expanding on the analysis by Ciotti (2010), we used the DF theory

in a joined analytical-numerical approach, providing a method to calculate the DF timescale in a system of field particles distributed with a mass spectrum. In particular, we searched for some non-monotonic radial behaviour of this quantity (due to the combination of the various mass components and their tendency to energy equipartition) that could account for the observed bimodality in the BSS-nRD. Our analysis showed that the DF timescales is always a monotonic function of the radius, being mainly shaped by the mass density profile (which, in turn, is monotonic with the radial distance).

Afterward, we moved to model GCs through direct N-body simulations, following the approach of progressively increase the level of realism (and complication) of the simulations. We first ran a set of simulations with 10^4 particles and modeled the mass spectrum with only three mass populations. Then, we followed the evolution of the BSS-nRD focusing on the position of the minimum and on the formation of the central peak.

Our models always show the formation of a central peak in the BSS-nRD. Moreover, a longlasting bimodal shape arises for almost all the studied cases, althought the detection of the minimum appears to be sometime challenging due to statistical noise and the lowest concentrated case shows no bimodality, with only a central peak forming and disappearing toward the end of the run. We also ran a simulation with an increased number of particles ($N = 10^5$), which has shown, compared to the previous cases, a more gradual evolution of the BSS-nRD shape, with a central peak and a bimodality gradually appearing as the dynamical evolution proceeds, coupled with a more stable migration of the minimum outward.

This motivated us to run $N = 10^5$ simulations with a realistic mass spectrum following a Kroupa (2001) Initial Mass Function, and admitting the presence of a population of neutron stars (NSs) and stellar-mass black holes (BHs). We focused on the influence of the heavy remnants on the BSS segregation. Moreover, we defined a new parameter (named A^+), defined as the area between the cumulative radial distributions of BSSs and reference stars, as a hand of the dynamical clock alternative to $r_{\rm min}$.

Our results show that a subsystem of stellar-mass BHs (which rapidly collapse toward the cluster centre and decouple from the rest of the stars) substantially inhibits the mass segregation process of BSSs (and, more in general, of all the mass populations in the cluster). The time evolution of the new parameter A^+ revealed that this quantity is a very good tracer of the BSS segregation process and of the overall cluster evolution, strongly depending on the presence and fraction of BHs. We also found that A^+ assumes comparable values in all the runs when its time evoultion is expressed in units of the core-collapse (CC) time of the system, suggesting that, with a proper calibration, it can be used as an indicator of the time-remaining to cluster CC.

An observational determination of the new parameter A^+ for a set of 25 GCs has been carried out, confirming what guessed from the previous results. In fact, the values of A^+ have been found to well correlate with the observed position of the minimum of the BSS-nRDs (with the advantage of being easier to measure) and even more tightly with the central relaxation time of the observed clusters. This last result opens the future possibility that A^+, after a proper calibration, could provide a more precise measure of the central relaxation time of GCs.

Undoubtedly, the cluster models built so far still suffer from the lacking of one fundamental ingredient: a population of primordial binaries. We just started to work on an improved cluster model made of 10^5 stars with a mass spectrum, a population of NSs and BHs and a fraction of primordial binaries ($f_{\rm bin} = 3\%$). In particular, since mass-transfer BSSs are known to form in binary system, a proper modeling of a BS as a binary system is desirable in the direction of a more realistic description of the dynamics of these objects. For this reason, from the primordial binary population, we searched those systems with orbital parameters comparable with observed BSSs, with the aim to follow their evolution with time and study the extent to which their binary nature could affect their segregation. However, we just started the analysis of the output and the work is still in progress.

The Thesis is organized as follows: in Chapter 1 we introduce some properties of GCs, briefly describing their dynamical evolution. We also dedicate the final part of the Chapter to BSSs, listing their most important observational features. In Chapter 2 we present the analysis of the DF timescale in multi-mass systems by means of a semi-analytical approach, while our first work in the direction of using N-body simulations to study the BSS segregation process is discussed in Chapter 3. Chapter 4 concerns the N-body simulations admitting NSs and BHs, and the behaviour of the new parameter A^+ in simulated systems, while its observational measurements on a sample of 25 GCs is the topic of Chapter 5. Chapter 6 summarizes the main results of our study.

Chapter 1

Introduction

1.1 Globular clusters

1.1.1 Observational properties

Globular clusters (GCs) are gravitationally bound stellar systems consisting of a few $10^5 - 10^6$ stars. The Milky Way (MW) contains about 150 GCs, which can be considered as fossil witnesses of the formation epoch of our Galaxy. Indeed, stars in GCs are known to be very old, with an estimated age between 10 and 13 *Gyr* (e.g., Gratton et al., 1997; Chaboyer et al., 1998; Marín-Franch et al., 2009). They metal poor stellar systems ([Fe/H]< -1 for the bulk of Galactic GCs), essentially free of dust and gas.

For many decades, GCs have been considered Simple Stellar Populations (SSPs), formed by coeval stars with the same chemical composition, and such a feature makes these systems perfect laboratories to test stellar evolution models. This paradigm has recently been challenged by the observational evidence of the presence of multiple stellar populations (MSPs) in these systems (e.g., Bedin et al., 2004; Gratton, Sneden & Carretta, 2004; Piotto et al., 2007; Carretta et al., 2009b,a; Milone et al., 2008). However, their homogeneity in the iron abundance (Carretta et al., 2009b) is the proof of their inhability to retain supernovae ejecta. Hence, at least as a first approximation, GCs can still be considered as SSPs and remain the best observational tools to verify the predictions of stellar evolution models (see Kalirai & Richer, 2010).

GCs can be divided in two different sub-systems on the basis of their kinematics, spatial distribution and metallicity (Zinn, 1985). Indeed, the metal-rich clusters (with [Fe/H]≥ -0.8) are typically distributed in the Galactic plane, throughout the disk, with a typical rotation velocity of about 150 $km\ s^{-}1$. These are therefore called disk GCs, or G clusters. Instead, the group of metal-poor ([Fe/H]< -0.8) systems

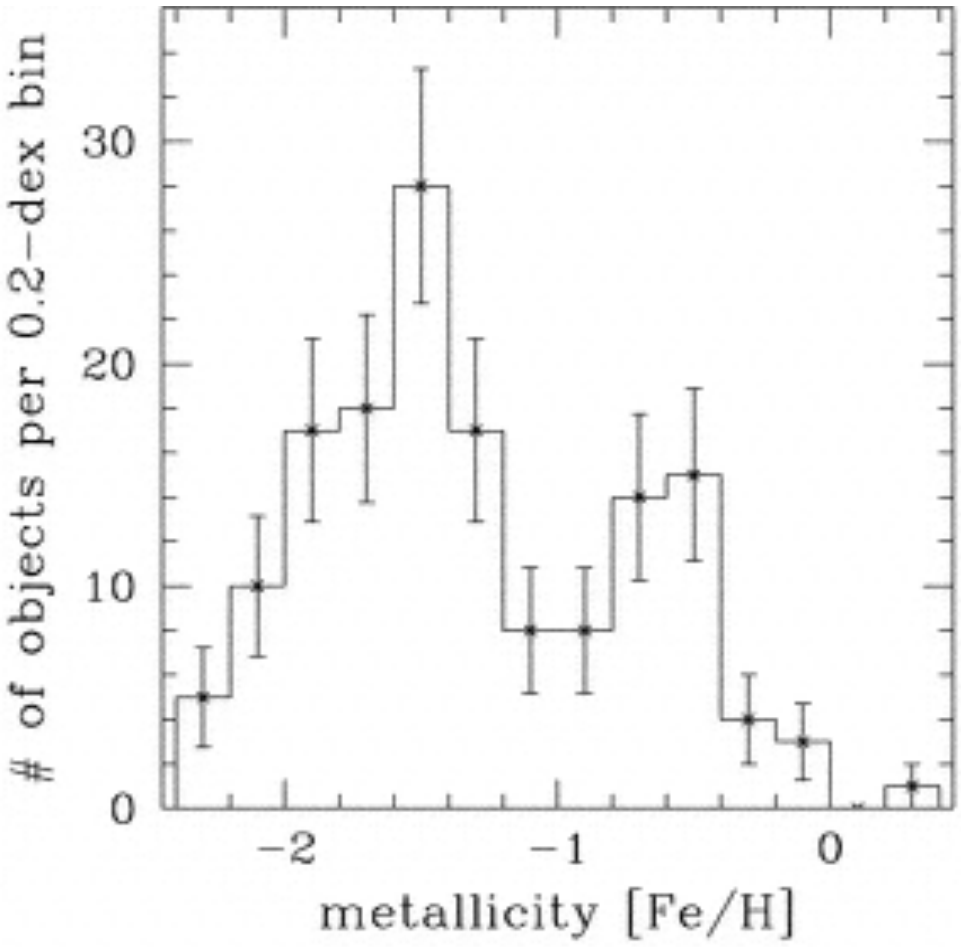

Figure 1.1: Metallicity distribution of MW GCs. From of VanDalfsen & Harris (2004)

has a spherical distribution within the Galactic halo, with a velocity dispersion $\sigma \sim 50\ km\ s^{-}1$ (Armandroff, 1989). These are thus called halo GCs, or F clusters. Figure 1.1 shows the bimodality in the metallicity distribution of MW GCs, that supports the distinction into halo and disk-GCs; the peak around [Fe/H] ~ -1.6 is related to the metal-poor component, while the peak around [Fe/H] ~ -0.6 to the metal-rich one.

1.1.2 Internal dynamics

The dynamics of GCs has been matter of interest and investigations during the last 70 years, because they are indeed perfect and unique laboratories for testing our understanding of the processes occurring in dissipationless self-gravitating systems (see Meylan & Heggie, 1997, and reference therein).

GCs are multi-particle systems and their internal dynamics is mainly led by the two-body encounters between their stars. In such interactions, stars exchange

energy with each other and the cumulative effect is to completely lose trace of their orbital initial condition in a time-scale that is shorter than the age of the host system. This diffusive process is called *two-body relaxation* (Binney & Tremaine, 2008). In a stellar system having a crossing time t_{cross}, two-body relaxation occurs on a timescale defined as:

$$t_{2b} = n_{2b}\, t_{cross},$$

where n_{2b} is the number of crossings required for a star to change its velocity by of order itself and t_{2b} is the so called *two-body relaxation time*. For a stellar system made by N stars of identical mass, t_{2b} can be expressed with a simple approximation (Binney & Tremaine, 2008):

$$t_{2b} \simeq \frac{0.1N}{\ln N} t_{cross}.$$

This expression of the relaxation time, gives the time-scale after which the velocity of a star in a system of N particles can be no longer estimated by considering the gravitational potential as generated by a smooth distribution of stars. It is the time-scale over which a star orbiting a system, feels the "granularity" term of the potential, due to the other single stars, taken one by one (Ciotti, 2000). For those systems with many particles and much older than their crossing time, encounters between stars are unimportant (this is the case of galaxies, with $N \approx 10^{11}$ and an age which is few hundreds time higher than their crossing time). For the case of GCs, however, the number of particles is much smaller than for a galaxy ($N \approx 10^5 - 10^6$) and their crossing time is $t_{cross} \approx 1 Myr$, implying that their age is thousands of times higher: hence, for a GC, encounters between stars strongly influence the dynamics of the system, and its structure as well, and they have to be taken into account for modeling the dynamical evolution of these systems. In GCs, the constituent particles move under the influence of the gravitational field generated by a collection of point masses, rather than a smooth mass distribution. More in general, such systems are called *collisional* ((while galaxies are *collisionless*). As a general statement, collisional (collisionless) systems are much older (younger) than their relaxation time.

The dynamical evolution of a GC can be divided into three different phases. The first phase is the early evolution, which occurs on the first few Myr. It is characterized by the expulsion of the primordial residual gas in which a young cluster is still embedded in the very early stages of its life, along with mass loss due to the evolution of the most massive stars in the cluster (for example, the expulsion of Type II supernova ejecta). Basing his calculation on the virial theorem, Hills (1980) claimed that clusters in equilibrium lose impulsively more than half of their mass and, in response to their mass loss, they rapidly expand and dissolve. This result has been confirmed during the next two decades, when semi-analytic calculations

(e.g., Applegate, 1986; Chernoff & Shapiro, 1987) and numerical simulations (e.g., Chernoff & Weinberg, 1990; Fukushige & Heggie, 1995; Portegies Zwart et al., 1998) showed that mass loss due to stellar evolution triggers an expansion, which can lead to a rapid cluster dissolution. In particular, Chernoff & Shapiro (1987) and Chernoff & Weinberg (1990) showed that mass loss due to stellar evolution can cause the rapid dissolution of clusters with a low initial concentration and/or a flat stellar initial mass function (IMF), while Fukushige & Heggie (1995) explored the mechanism behind the dissolution and showed it to be the result of a loss of equilibrium as the cluster expands and reaches structural properties for which no virial equilibrium is possible, rather than of a loss of stability, as previously stated. These results have been confirmed and somehow also refined by Boily & Kroupa (2003a,b) who showed, by means of numerical simulations, that a cluster can lose up to 70 % of its mass without undergoing complete dissolution. However, in most cases a cluster undergoes significant expansion and needs to be initially much more compact than observed today to survive this phase (Baumgardt & Kroupa, 2007).

Since mass loss due to stellar evolution comes from the most massive stars in the cluster, the expanding reaction of the cluster can be stronger (and the dissolution time-scale shorter) if the cluster is primordially mass-segregated. Vesperini, McMillan & Portegies Zwart (2009) showed that the strength of the initial cluster expansion is higher as the degree of initial mass segregation increases. As a result, clusters differing only in the degree of initial mass segregation can have very different lifetimes. Mackey et al. (2007, 2008) showed that the stronger early expansion of mass-segregated clusters, along with the subsequent heating from a population of stellar-mass black holes, can account for the radius–age trend observed for massive clusters in the Magellanic Clouds. More recently, Haghi et al. (2014) showed that some of the very extended globular clusters in the outer halo of the Milky Way may have been born with primordial mass segregation.

Finally, since early cluster dissolution preferentially destroys low-mass clusters, the initial phase may play an important role in the evolution of the mass function of globular cluster systems, which, as a result, significantly flattens in the low-mass end (see Vesperini, 2010, and references therein).

The second phase of dynamical evolution of a GC starts when the expansion due to the mass loss from stellar evolution ends. This phase is mainly characterized by the two-body relaxation process, which shapes the structural properties of the system. For instance, during this phase, the cluster develops two distinct regions, an inner isothermal sphere (the core) and an outer halo (Spitzer, 1987). The inner region is characterized by an almost uniform density profile, and contains typically about half of the cluster mass, while the surrounding halo is populated by stars preferentially moving in radial orbits. The first important effect of two-body relaxation is the mass loss due to escaping stars: in fact, as a star exchanges energy

with other stars in the cluster due to close and distant encounters, it can reach an energy higher than the one needed to escape from the cluster. This process plays a key role in the lifetime of those systems that survive the early mass loss phase due to stellar evolution, directly modifying the mass function of the cluster (e.g., Vesperini & Heggie, 1997); however, for isolated clusters (i.e., those clusters not suffering an external tidal field), the mass loss due to two-body relaxation is highly reduced and the dissolution timescale is extremely long (e.g., Giersz & Heggie, 1994; Heggie, 2001; Baumgardt, Hut & Heggie, 2002; Heggie & Hut, 2003). In particular, Baumgardt, Hut & Heggie (2002) have shown that it takes about a thousand of initial half-mass relaxation times for a cluster to lose about half of its initial mass.

If an external tidal field is introduced, on the other hand, a large number of studies show that the mass-loss rate is significantly enhanced, due to the lowering of the escape speed and the truncation of the cluster size (e.g., Chernoff & Weinberg, 1990; Vesperini & Heggie, 1997; Aarseth & Heggie, 1998; Takahashi & Portegies Zwart, 2000). In particular, Fukushige & Heggie (2000) and Baumgardt (2001) showed that, when the tidal field is properly modelled, a star can escape from the cluster only through a Lagrangian point. This process requires more time with respect to the "escape everywhere" case, delaying significantly the dissolution of the system.

In addition to mass loss due to two-body relaxation, especially for clusters on eccentric orbits, there is another mass-loss process occurring in this phase: the tidal shocks due to passages near the bulge and through the disk of the host galaxy. These passages, indeed, inject energy into the cluster and speed up the process of mass loss due to two-body relaxation (e.g., Gnedin & Ostriker, 1997; Gnedin, Lee & Ostriker, 1999). However, this kind of mass-loss mechanism is independent of stellar mass and, in general, does not influence the slope of the mass function, unless it is combined with mass segregation (e.g., Vesperini & Heggie, 1997).

While two-body relaxation proceeds and stars exchange energy among each others, the various mass components manifest the tendency to energy equipartition, so that, low-mass stars enhance their velocities, preferentially occupying the outer regions of the cluster, while high-mass stars slow down and sink toward the centre due to dynamical friction (DF; see Chapter 2 for a detailed treatment of this process), occupying the cluster core. This process leads to a stratification of the various mass populations, from high-mass to low-mass stars as the radial distance from the centre increases. As a consequence, low-mass stars spend more time than high-mass ones in the external escaping region of the cluster, dominating the population of escaping stars and causing a flattening of the cluster mass function (e.g., Vesperini & Heggie, 1997; Baumgardt & Makino, 2003; Trenti, Vesperini & Pasquato, 2010).

This second phase of GC dynamical evolution ends with the most violent and important process in their lifetime: the core-collapse (CC). First studied by Hénon

(1961) this process, also known as "gravothermal catastrophe", has subsequently been explored in a large number of investigations (Hénon, 1961; Lynden-Bell & Wood, 1968; Larson, 1970a,b; Lynden-Bell & Eggleton, 1980, see also Heggie & Hut, 2003 for a review and references). In particular, Lynden-Bell & Wood (1968), using thermodynamical concepts, gave the theoretical explanation of this phenomenon: the core of the system is "hotter" than the halo (i.e., core stars have larger velocity dispersion than halo-stars) so that there is an outward flux of heat; the core loses energy, contracts, and becomes hotter as a consequence of the virial theorem. Without intervention by an energy source balancing the loss of energy from the core, this process accelerates, leading to a smaller and smaller core and a diverging central density in a finite time.

The supporting energy source are known to be binary stars, either primordial or dynamically formed during close encounters between single stars: they can provide the energy needed to halt CC and support the core afterward in time (see, e.g., Heggie & Hut, 2003, and references therein). The first works invoking binary stars as additional sources of energy are those by von Hoerner (1960) and Hénon (1961). A detailed physical explanation, however, came more than a decade later, with Heggie (1975) showing that binary stars with binding energy higher than the "temperature" of the system, will, on average, increase their binding energy and release the energy lost to the star cluster. Finally, we highlight that during the phase that leads to the cluster CC, both the central (especially) and the half-mass relaxation time (much less) decrease with time.

The third and last phase in the cluster dynamical evolution is the one starting right after CC, thus called the *post core collapse* (PCC) phase. It is characterized by a "freezing" of all the physical quantities of the cluster (central and half-mass relaxation times, Lagrangian radii, etc.), which do not change significantly, in a continuos slowly fluctuating dynamical state (Spitzer, 1987). In particular, in this phase the cluster experiences the so called *gravothermal oscillations* first predicted by Bettwieser & Sugimoto (1984): after CC, the central density undergoes nonlinear oscillations, in a steady-behaviour. Investigations about the stability conditions of this process have been carried out few years later by Goodman (1987), who provided quantitative criteria for the core and the whole system to be stable during this process, further confirmed by Cohn, Hut & Wise (1989) and Makino (1996). However, the theoretical understanding of the onset of gravothermal oscillations is still a matter of debate (Breen & Heggie, 2012b,a).

Observational studies have shown that about 20% of Galactic GCs have cuspy surface-brightness profiles and identified these objects as clusters in the PCC phase (Djorgovski & King, 1986; Chernoff & Djorgovski, 1989; Djorgovski & Meylan, 1994). As predicted by Chernoff & Shapiro (1987), PCC clusters are preferentially located near the Galactic centre (Chernoff & Djorgovski, 1989, where the tidal field

is stronger: this implies that GCs have smaller sizes and, thus, shorter relaxation times that more rapidly drive them towards CC.). However, we finally emphasize that a reliable classification of clusters as PCC based on their structural properties is still hazardous. Trenti, Vesperini & Pasquato (2010), for instance, showed how a system in its gravothermal oscillation phase can look like a non-PCC cluster from the point of view of its concentration.

1.1.3 King models

Until the late 80s, the surface-brightness profiles of GCs were fitted successfully with equilibrium models based on lowered Maxwellians and commonly known as King models (King, 1966); these dynamical models take into account the three most important elements of globular cluster structure: dynamical equilibrium, two-body relaxation and tidal truncation. Mathematically speaking, King models are based on the following distribution function:

$$f(E) = \begin{cases} \rho_0 (2\pi\sigma^2)^{-3/2} (e^{E/\sigma^2} - 1) & \text{if } E > 0 \\ 0 & \text{if } E \leq 0 \end{cases}$$

where ρ_0 is the central density, σ is the one-dimensional velocity dispersion and E the relative energy per unit mass in the relative potential $\Psi(r)$, so that (Binney & Tremaine, 2008):

$$E = \Psi(r) - \frac{v^2}{2}.$$

This distribution function resembles the isothermal sphere at small radii, where the majority of stars have large values of the relative energy E, but is less dense than the isothermal sphere at large radii, so that its total mass is finite. The physical basis for this distribution function is the presence of a galactic tidal field, which "delete" from the system those stars crossing the tidal cut-off radius (r_t), truncating the cluster.

The tidal radius r_t is the radius at which the potential is determined by the total mass of the cluster:

$$\Phi(r_t) = -\frac{GM(r_t)}{r_t},$$

where G is the gravitational constant and $M(r_t)$ is the mass of the cluster within the tidal radius (i.e. the total mass of the system). The central potential is then $\Phi(0) = \Phi(r_t) - \Psi(0)$. The bigger the value of $\Psi(0)$, the greater the tidal radius, the total mass and $|\Phi(0)|$. This model has a characteristic scale length, called *King radius*:

$$r_{\mathrm{K}} = \sqrt{\frac{9\sigma^2}{4\pi G\rho_0}},$$

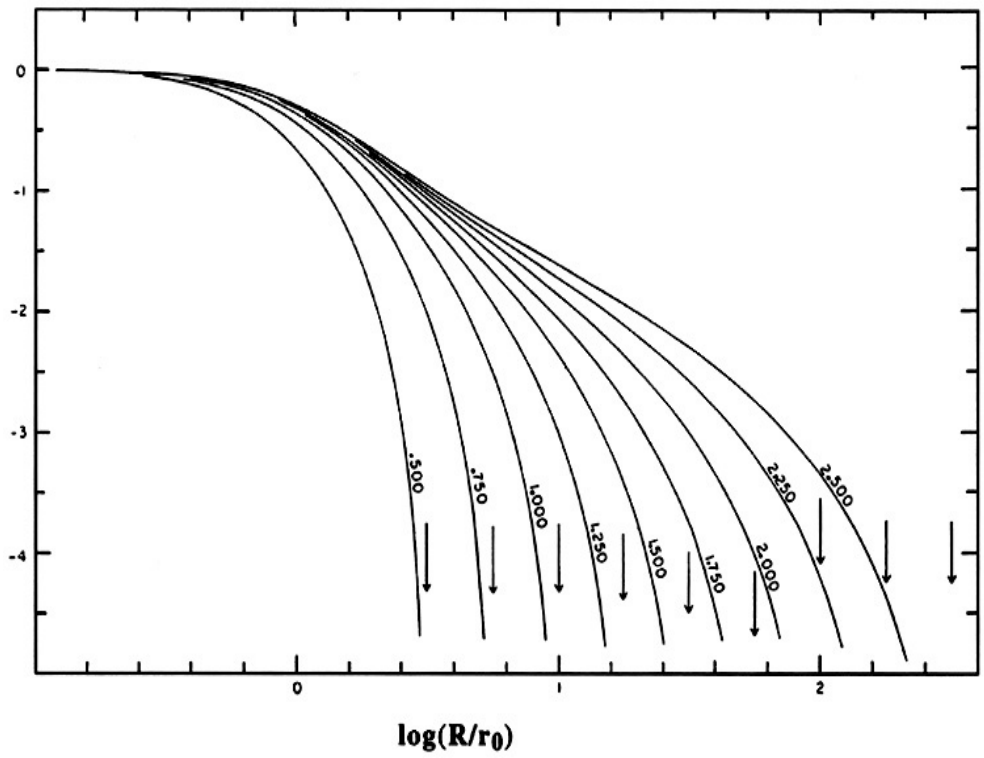

Figure 1.2: Logarithm of the projected density (normalized to its central value) for King models. Different curves are obtained for different values of W_0 (the labels on each curve mark the corresponding values of the concentration parameter c). The radius is normalized to the King radius, indicated here as r_0. From King (1966)

which is the radius at which the projected density reaches roughly half of its central value.

This is a family of one-parameter dynamical models. In particular, for different values of $\Psi(0)$, or, as it is commonly used, $W_0 \equiv \Psi(0)/\sigma^2$, different King models (i.e., different density profiles) are obtained. In Figure 1.2 the projected density profiles of King models with different values of W_0 are shown. The profiles in the figure clearly show the core-halo structure mentioned in Sect. 1.1.2, with a flat core surrounded by an extended halo of decreasing density at larger radii. In particular, by increasing the value of W_0, the density profile more rapidly drops at large radii, which corresponds to a decrease of the concentration parameter c, defined as the logarithm of the ratio between the halo size and the core size: $c = \log(r_t/r_c)$.

King models are widely used to reproduce the observed surface brightness profile of GCs, even though recent results have shown that the Wilson (1975) models provide improved fits in the outer parts of some observed clusters (Di Cecco et al., 2013). However, King models are currently used for fitting procedures, still showing equivalent results as the Wilson model in many cases (e.g., Miocchi et al., 2013;

Wang & Ma, 2013).

1.1.4 N-body modeling

GCs are made of N individual stars (with $N = 10^5 - 10^6$). This implies that the study of the motion of the stars in such systems is the so called *N-body problem*. In other words, studying the dynamics of the stars in a GC corresponds to determine the motion of N points with masses m_i, position vectors $\mathbf{r}_i$ and velocity vectors $\mathbf{v}_i, with i = 1, ...N$. The force acting on the $i - th$ particle due to the gravitational attraction of all the other $N - 1$ particles is:

$$m_i \ddot{\mathbf{r}}_i = \sum_{j=1,\ j\neq i}^{N} \frac{G m_i m_j}{r_{ij}^2} \frac{\mathbf{r}_j \mathbf{r}_i}{r_{ij}}.$$

where $\mathbf{r}_i$ is the position vector of the $i - th$ particle. The problem is then of the $6N$ order (three coordinates for the position and three for the velocity of each one of the N particles).

It is well known that for $N \geq 2$, the N-body problem is generally not analytically solvable, i.e., it cannot be reduced to $6N - 1$ independent integrations. However, once a set of initial conditions is specified (for instance the initial positions and velocities of all particles) it exists a unique solution, which for N larger than 2 requires numerical integration to be determined.

Nowadays computer simulations are the most powerful tool for the study of the dynamics of systems with a large number of particles. They can be divided into two big families, depending on the nature of the system they reproduce: on one side, the direct N-body simulations, for collisional systems; on the other side, the collisionless ones. Both kinds of simulations have their specific integration methods developed during the years.

The first kind of simulations use the most accurate method for solving the N-body problem: the direct summation. This method consists in computing the force acting on each particle by summing all the contributions from any other particle (Aarseth, 1999; Spurzem, 1999), with no simplifying assumptions. Both close and distant interactions are explicitly taken into account. These codes are used to study the dynamics of collisional systems, since the motion of a single particle is strongly influenced by each single encounter with the other stars (see Sect. 1.1.2). Among these codes, we mention the `NBODY` code series developed by Sverre Aarseth during the years (see Aarseth, 1999, for a review) and now arrived at its Graphic Processing Unit (GPU) version (Nitadori & Aarseth, 2012), which has been extensively used in this Thesis.

For collisionless systems, on the other hand, the encounters between stars are

unimportant, so that the numerical codes treating these kinds of systems approximate the particles surrounding any given object in groups according to their spatial distribution, and compute the force exerted by the whole group (instead of considering the contribution of each particle within the group). Among these methods, there are two main ones: the tree codes (Barnes & Hut, 1986; Springel, Yoshida & White, 2001) and the Fast Multipole Method (FMM) (Greengard & Rokhlin, 1987, 1997). The former arranges particles in cells and computes the force contributions from these cells using truncated multipole expansions, and is usually adopted for large gravitational system simulations; the latter, uses multipole expansions to calculate the potential field, and becomes particularly suitable for systems with an homogeneous density distribution. In this class, we mention also the particle-mesh method (Hockney, 1965; Hockney & Eastwood, 1988; Fellhauer et al., 2000), in which the field is computed on a regular grid rather than with a multipole expansion by solving a field equation for the potential.

A different class of approximated methods includes Monte Carlo (MC) and Fokker-Planck (FP) methods. MC methods (Hénon, 1975; Giersz, 1998; Joshi, Rasio & Portegies Zwart, 2000) treat the N-body system as a continuous system in which particles are replaced by spherical shells of matter. Assuming equilibrium in a smooth spherical potential, the global evolution of the system is followed. FP methods (Cohn, 1980; Murphy, Cohn & Durisen, 1991) use a similar approach, but follow the evolution of the system by direct integration of the Fokker-Planck equation, using distribution functions instead of particles.

In direct N-body methods, the number of force computations per particle is $N(N-1)/2$ so that the scaling is $O(N^2)$ with the number of particles, per timestep. The scaling rises to $O(N^3)$ by considering that a realistic simulation lasts for at least a relaxation time, which is proportional to the particle number. The computational costs for direct N-body simulations are therefore extremely high. The algorithms can be parallelized, but in practice load imbalances may saturate the gain in efficiency, so some of the most CPU-demanding simulations have been carried out on special purpose hardware, such as the GRAPE (Makino & Taiji, 1998), where the chip architecture has been optimized to compute gravitational interactions, thus delivering Teraflops performance. On the other hand, approximate methods as the tree code, usually scale as $O(N \log N)$, but the approximations introduce some errors which, in the worst cases, can lead to paradoxes (as the "exploding galaxy"; Salmon & Warren, 1994). Moreover, force errors from the tree code may lead to violation of momentum conservation. Typical implementations of the tree code solve this problem with multipole expansion of the potential. However, systems with several hundred thousands of collisionless particles can be easily simulated on a GigaFlops workstation for a Hubble time using this method. For a comparison between direct and approximate methods see, e.g., Aarseth (2003) and Trenti & Hut (2008).

A further challenging point of the N-body simulations consists in the huge range of length and timescales characterizing common astrophysical problems. In the case of GCs, for instance, length scales span the range from kilometres to parsecs (a factor of more than 10^{13}) and time-scales span the range from milliseconds to the lifetime of the Universe (a factor of more than 10^{20}). As a result, special integration methods have been developed for the purpose.

We remark finally that computer N-body simulations are developing as a fundamental aspect of the Astrophysical research, often used as an extention of previous theoretical calculations. They can be applied to reproduce observed phenomena, as well as to investigate unobservable circumstances and make possible predictions. Joined with the continuos hardware and software advances, they are one of the most useful tools to our understanding of more and more complex phenomena in astrophysics.

1.2 Blue Straggler stars

1.2.1 Definition

Blue straggler stars (BSSs) are commonly defined as those objects that, in an optical color magnitude diagram (CMD), are located along an extrapolation of the main sequence (MS), in a region brighter and bluer (hotter) than the turnoff (TO) point. They were first discovered by Sandage (1953) in the outskirts of the Galactic GC M3 (see Figure 1.3) and then detected in the external region of other dense GCs, or in relatively loose clusters (thus generating the idea that low-density environments were their *natural habitats*). The picture dramatically changed in the early 90s, when high spatial resolution observations clearly showed that this was just an observational bias (see the case of NGC 6397; Auriere, Lauzeral & Ortolani, 1990). In particular, the advent of the Hubble Space Telescope (HST), providing both high resolution and ultraviolet (UV) facilities, allowed to properly image and systematically discover BSSs also in the highly-crowded central regions of dense GCs (note, in fact, that BSSs are hot stars, of $\sim$ 7000 K, best detectable at UV wavelengths, where giant stars fade substantially). The largest compilations of BSSs to date have been collected for nearly 60 Galactic GCs surveyed with the HST/WFPC2 (see Piotto et al., 2004; Leigh, Sills & Knigge, 2007; Moretti, de Angeli & Piotto, 2008), and about 40 clusters (Leigh, Sills & Knigge, 2011; Simunovic & Puzia, 2016) observed with the HST/ACS and the HST/WFC3 (Sarajedini et al., 2007; Piotto, 2015). These compilations, together with deep investigations in open clusters (e.g., Geller & Mathieu, 2011; Gosnell et al., 2014, 2015) and in dwarf spheroidals (Mapelli et al., 2009; Monelli et al., 2012), have significantly contributed to form the nowadays largely accepted idea that BSSs are a stellar population common to any stellar

system and that they preferentially populate the highest density cluster regions.

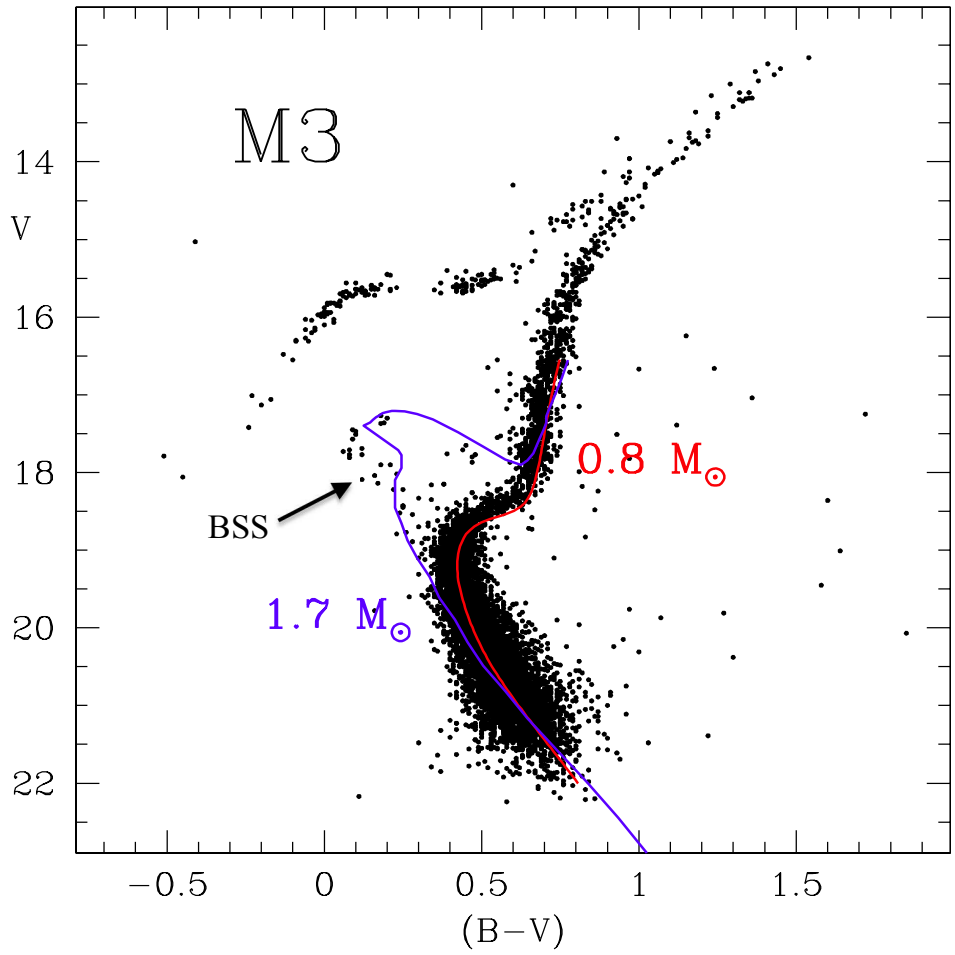

Figure 1.3: Optical CMD of the globular cluster M3, with the location of BSSs indicated by the arrow. The theoretical track corresponding to $0.8M_{\odot}$ well reproduces the main evolutionary sequences of the cluster, while BSSs populate a region of the CMD where core hydrogen-burning stars of $\sim 1.7M_{\odot}$ are expected. From Buonanno et al. (1994).

1.2.2 BSS formation mechanisms

Not only their location in the CMD, but also direct mass measuremets (Shara, Saffer & Livio, 1997; Gilliland et al., 1998; Fiorentino et al., 2014) suggest that they are more massive ($M_{\rm BSS} \sim 1.2M_{\odot}$) than the current cluster population ($m0.8M_{\odot}$). However, since GCs are completely devoid of gas and any recent star formation event can be realistically ruled out, the formation of BSSs can be explained only by assuming that some mechanisms able to increase the initial mass of single stars is at work. While these processes are not completely understood yet, the main leading scenarios, at present, are mass transfer (MT) in binary systems (McCrea, 1964; Zinn

& Searle, 1976), possibly up to the complete coalescence of the two companions, and the merger of stars induced by direct collisions (COL; Hills & Day, 1976).

With the aim of understanding how BSSs form and if their formation mechanisms depend on some cluster physical properties, the most recent catalogs have been used to search for correlations between the number or the fraction of observed BSSs, and several parameters tracing the cluster structure (as luminosity, mass, central density, etc.), as well as for correlations with the collision rate and binary fraction. Though not conclusive, this approach has provided a number of interesting results. For instance, no correlation has been found with the collisional parameter (e.g. Piotto et al., 2004; Davies, Piotto & de Angeli, 2004; Leigh, Sills & Knigge, 2007; Leigh et al., 2013), while a strong correlation has been revealed between the number of BSSs in cluster cores and the core mass (Knigge, Leigh & Sills, 2009; Leigh et al., 2013). These facts have been interpreted as the evidence of a binary (instead of a collisional) origin of BSSs, even in the densest environments, like the centre of post-core collapsed (PCC) clusters (Knigge, Leigh & Sills, 2009). However, by studying a sample of 24 GCs, Milone et al. (2012) found a nice correlation between the BSS specific frequency and the binary fraction in cluster cores. This has been confirmed also by Leigh et al. (2013), who, however, obtain a much stronger correlation between the number of core BSSs and the cluster core mass. Interestingly, in the Milone et al. (2012) plot, PCC clusters lie well outside the relation. This likely reflects the role that internal dynamics plays on the binary and BSS content of GCs. In fact, binary systems are subject to frequent dynamical interactions with other binaries, single stars and even multiple systems. These interactions can either bring to stellar collisions, or significantly alter the physical properties of binaries, even promoting mass transfer activity. Hence, binaries and interactions play a crucial role in both the MT and the COL scenarios and it is probably impossible to separate the two effects just on the basis of the observed binary fraction. An exception could be represented by low density environments, where the efficiency of dynamical interactions is expected to be negligible. Very interestingly, indeed, a clear correlation between the binary and the BSS frequency has been found in a sample of 13 low density GCs ($\log \nu_0 < 3$ in units of $L_\odot/\mathrm{pc}^3$; Sollima et al., 2008, see Figure 1.4). This is the cleanest evidence that the unperturbed evolution of primordial binaries is the dominant BSS formation process in low-density environments (also consistently with the results obtained in open clusters; e.g. Mathieu & Geller, 2009).

Signatures of the two different formation processes have been searched also by means of spectroscopic studies (aimed at revealing chemical and/or rotational differences between the two classes; see Ferraro et al., 2006a; Lovisi et al., 2010, 2012; Mucciarelli et al., 2014; Simunovic & Puzia, 2014, and through theoretical and numerical investigations (e.g., Davies, Piotto & de Angeli, 2004; Leigh et al., 2013;

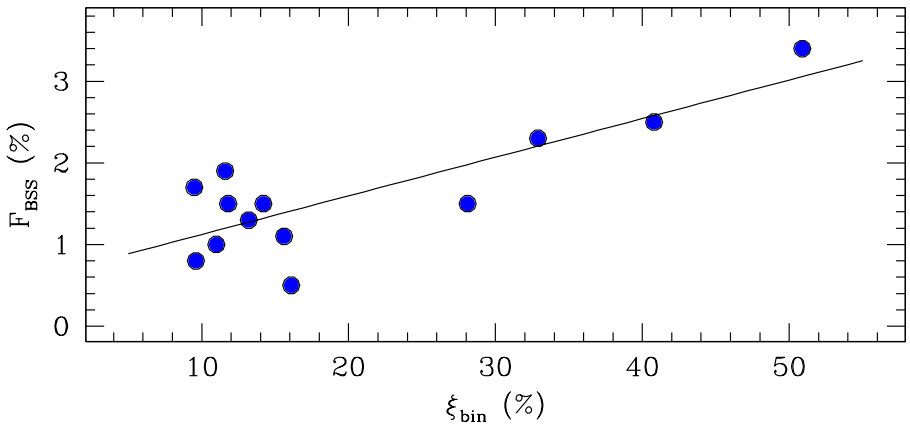

Figure 1.4: BSS specific frequency as a function of the core binary fraction measured in a sample of low-density GCs. The best-fit linear correlation is also plotted (solid line). From Sollima et al. (2008).

Chatterjee et al., 2013a; Sills et al., 2013; Xin et al., 2015), but no efficient way to disentangle MT-BSSs from COL-BSSs is known so far and this is still an open issue.

1.3 BSSs as dynamical probes

Independently of their formation mechanism, being more massive than the average cluster stars, BSSs suffer from the effect of DF, that makes them sink towards the cluster centre (e.g., Mapelli et al., 2004; Ferraro et al., 2012). In turn, the frequent stellar interactions occurring in the ultra-dense cores of Galactic GCs can promote both the formation and the hardening of binary systems, thus contributing to generate MT-BSSs. All these considerations clearly show that BSSs are powerful probes of GC internal dynamics and of its impact on standard stellar evolution (Bailyn, 1995; Ferraro et al., 2012, and reference therein). The main results obtained by exploting BSSs as dynamical probes are summarized in the following sections.

1.3.1 Double BSS sequences and core collapse

By using an exceptional set of 44 high-resolution images obtained with the HST-WFPC2, Ferraro et al. (2009) obtained a very high-precision CMD of the central region of the Galactic GC M30. The CMD revealed the existence of two well-separated and almost parallel sequences of BSSs (Figure 1.5). The two sequences are similarly populated, consisting of 21 and 24 stars, respectively. *This is the very first time that such a feature has been detected in any stellar system, and it could be the signature of the cluster core collapse imprinted onto the BSS population.*

The comparison with evolutionary models of BSS formed by direct collisions of

two MS stars (Sills, Karakas & Lattanzio, 2009) shows that the blue-BSS sequence is well fit by collisional isochrones with ages of $1 - 2$ Gyr (black solid lines in Fig. 1.6). Instead, the red-BSS population is far too red to be properly reproduced by collisional isochrones of any age, and its origin should therefore be different. Binary evolution models (Tian et al., 2006) have shown that during the mass-transfer phase (which can last several Gyr, i.e., a significant fraction of the binary evolution time-scale), the binary population defines a sort of "low-luminosity boundary" located ~ 0.75 mag above the zero-age MS in the BSS region. This is just where the red-BSS sequence is observed (red dashed line in Fig. 1.6). Hence, the BSS along the red-sequence could be binary systems still experiencing an active phase of mass-exchange.

Due to the normal stellar evolution, all BSSs will evolve toward the red giant branch (RGB) phase. In particular, the evolved blue-BSSs will populate the region between the two observed sequences and fill the gap. Hence, the fact that two well-separated chains of stars are observed supports the hypothesis that both the blue- and the red-BSS populations have been *generated by a recent and short-lived event, instead of a continuous formation process*. Quite interestingly, M30 is classified as a PCC cluster in the original compilation of Djorgovski & King (1986), and Ferraro et al. (2009) confirmed this finding by carefully re-determining the cluster density profile from deep HST images and detecting a steep power-law cusp in the innermost 5 arcsec $-$ 6 arcsec (~ 0.2 pc). During the CC phase the central stellar density rapidly increases, bringing to a concomitant enhancement of gravitational interactions (in fact, the collisional parameter scales as $\Gamma \propto \rho_0^{1.5} r_c^2$, where r_c is the core radius). In turn, these can trigger the formation of new BSSs, both via direct stellar collisions and via mass transfer activity in dynamically shrunk binary systems. All together these considerations support a scenario where the the BSSs along the blue sequence have been generated by the same dynamical event (the CC): the blue-BSSs arose from the enhanced stellar collision activity, while the red-BSSs are the result of the evolution of binary systems which first sank into the cluster center because of the DF (or they were already present into the cluster core), and then have been driven into the mass-transfer regime by hardening processes induced by gravitational interactions during the CC phase. According to this scenario, *the double BSS sequence detected in M30 dates the occurrence of the core collapse event back to 1-2 Gyr ago. If the proposed scenario is correct, this discovery opens the possibility of defining a powerful "clock" to date the occurrence of this dramatic event in a star cluster history* (see also Section 1.3.2).

Interestingly, analogous double BSS sequences have been observed also in two additional GCs experiencing core collapse or post-CC phases, namely NGC 362 (Dalessandro et al., 2013b) and NGC 1261 (Simunovic, Puzia & Sills, 2014).

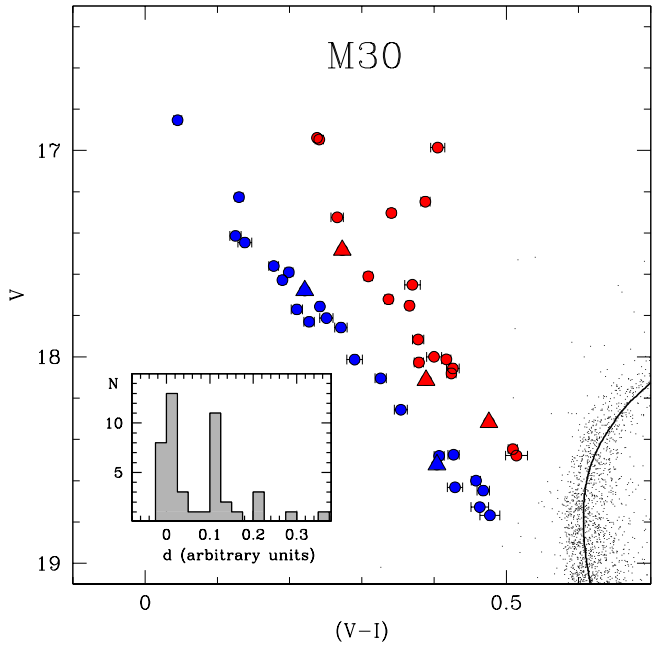

Figure 1.5: Optical CMD of M30 zoomed in the BSS region. The two distinct sequences of BSSs are highlighted as blue and red symbols. The inset shows the distribution of the geometrical distances of BSSs from the straight line that best fits the blue BSS sequence. Two well-defined peaks are clearly visible, confirming that the two sequences are nearly parallel to each other. From Ferraro et al. (2009).

1.3.2 The BSS radial distribution and the "dynamical clock"

By combining UV HST observations and wide-field optical observations from the ground, Ferraro et al. (1997) studied the radial distribution of the BSS population in the GC M3, finding a completely unexpected results: BSSs appeared to be more centrally concentrated than RGB stars in the cluster central regions, and less concentrated in the outskirts. This is shown in Figure 1.7, where $R_{\rm BSS}$ is the "double normalized ratio" (Ferraro et al., 1993), defined as:

$$R_{\rm BSS} = \frac{N_{\rm BSS}(r)/N_{\rm BSS}^{\rm tot}}{L^{\rm sampled}(r)/L_{tot}^{\rm sampled}}. \tag{1.1}$$

$N_{\rm BSS}(r)$ is the number of BSSs counted in a given radial bin, $N_{\rm BSS}^{\rm tot}$ is the total number of BSSs observed, and $L^{\rm sampled}(r)/L_{tot}^{\rm sampled}$ is the fraction of light sampled in the same annulus, with respect to the total measured luminosity. This ratio is expected to be equal to unity for any population with a radial distribution following that of the cluster luminosity, as RGB or horizontal branch (HB) stars (Renzini & Fusi Pecci, 1988). Figure 1.7 clearly shows that this is indeed the case for the HB population in M3 (grey segments), while BSSs are characterized by a completely different (a bimodal) radial distribution, that reaches a maximum in the center of the cluster,

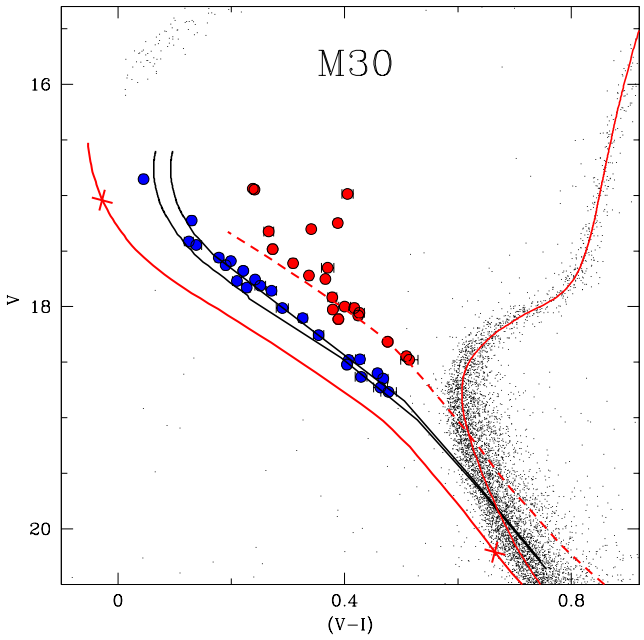

Figure 1.6: Magnified portion of the CMD of M30. The solid black lines correspond to the collisional isochrones of 1 and 2 Gyr, respectively, which accurately reproduce the blue BSS sequence. The solid red lines correspond to the single-star isochrones of 13 Gyr (well fitting the main cluster evolutionary sequences) and 0.5 Gyr (representing the reference cluster zero-age main sequence, ZAMS). The two crosses mark the respective positions of a $0.8M_{\odot}$ star and a $1.6M_{\odot}$ star along the ZAMS. The dashed red line corresponds to the ZAMS shifted by 0.75 mag, marking the lower boundary of the locus occupied by mass-transfer binary systems. This line well reproduces the red BSS sequence. From Ferraro et al. (2009).

shows a clear-cut dip in the intermediate region (at 100 arcsec $< r <$ 200 arcsec), and rises again in the outer region.

Sigurdsson, Davies & Bolte (1994) suggested that the bimodal BSS distribution observed in M3 could be explained by assuming that all BSSs formed in the core by direct collisions (thus originating the central peak of the distribution) and some of them were kicked out from the centre by the recoil of the interactions. Those BSSs ejected to a few core radii rapidly drifted back to the center of the cluster due to mass segregation (thus contributing to the central BSS concentration and generating the paucity of BSSs at intermediate distances of a few core radii). BSSs affected by more energetic recoils would have been kicked out to larger distances and, since they require much more time to drift back toward the core, they may account for the overabundance of BSSs observed in the cluster outskirts. However, Monte-Carlo dynamical simulations (Mapelli et al., 2004, 2006) demonstrated that BSSs kicked out from the core either are lost from the cluster, or sink back to the centre in 1-2 Gyr only. Hence the observed BSS bimodal distributions cannot be explained with a purely collisional population, and to accurately reproduce the external upturn of the

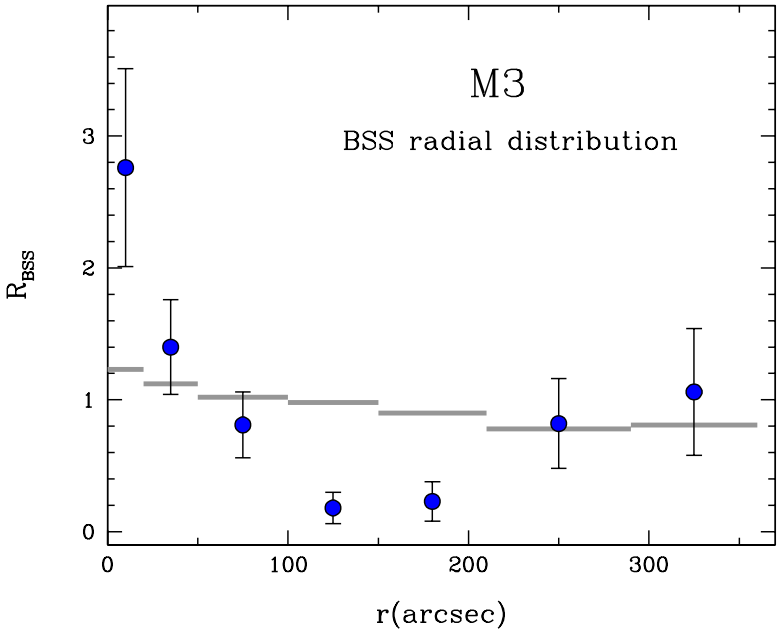

Figure 1.7: Bimodal radial distribution of BSSs in M3. The blue dots mark the value of the BSS double normalized ratio as defined in eq. (1.1), computed at various distances from the cluster centre, the gray segments mark the double normalized ratio of HB stars. From Ferraro et al. (1997).

distribution it is necessary to assume a sizable fraction ($\sim 20-40\%$) of MT-BSSs, generated in the peripheral regions where primordial binaries can evolve in isolation and experience mass transfer processes without suffering significant interactions with other cluster stars.

While the bimodality detected in M3 was considered for years to be *peculiar*, more recent results demonstrated that this is not the case. In fact, the same observational strategy adopted by Ferraro et al. (1997) in M3 has been applied to a number of other clusters, and bimodal distributions have been detected in the majority of cases (~ 25) studied so far (see below). Only a few exceptions are known: M30, M75, M79, and M80, which do not present any external upturn (Lanzoni et al., 2007b; Contreras Ramos et al., 2012; Ferraro et al., 2012), and four clusters (ω Centauri, NGC 2419, NGC 6101 and Palomar 14) showing a completely flat BSS radial distribution, totally consistent with that of the reference population (Ferraro et al., 2006b; Dalessandro et al., 2008; Beccari et al., 2011; Dalessandro et al., 2015, respectively). The last four cases deserve a specific comment. The flat behaviour discovered in these clusters suggests that the BSS radial distribution is not yet significantly altered by stellar interactions and by the dynamical evolution of the cluster. *Indeed, this is the cleanest evidence of the fact that these systems are not fully relaxed yet, even in the central regions.* Very nicely, this in the cases of ω Centauri and NGC 6101 this is confirmed

also by the radial distribution of MS stars and binary stars, which show a level of mass segregation lower than what expected from equipartition (Anderson, 2002; Dalessandro et al., 2015).

The "stellar system dynamical clock"

The entire database of available BSS radial distributions has been analysed by Ferraro et al. (2012). It consists of 21 GCs with very different structural properties (hence possibly at different stages of their dynamical evolution), but with nearly the same chronological age (12-13 Gry; Marín-Franch et al., 2009), with the only exception of Palomar 14 which formed ~ 10.5 Gyr ago (Dotter, Sarajedini & Yang, 2008). While significant cluster-to-cluster variations were already known, Ferraro et al. (2012) discovered that once the radial distance from the centre is expressed in units of the core radius (thus to allow a meaningful comparison among the clusters), GCs can be efficiently grouped on the basis of the shape of their BSS radial distribution, and at least three families can be defined:

- *Family I* – the radial distribution of the BSS double normalized ratio ($R_{\rm BSS}$) is fully consistent with that of the reference population ($R_{\rm pop}$) over the entire cluster extension (see Figure 1.8);
- *Family II* – the distribution of $R_{\rm BSS}$ is incompatible with that of $R_{\rm pop}$, showing a significant bimodality, with a central peak and an external upturn. At intermediate radii a minimum is evident and its position ($r_{\rm min}$) can be clearly defined for each sub-group (see Figure 1.9);
- *Family III* – the radial distribution of $R_{\rm BSS}$ is still incompatible with that of the reference population, showing a well defined central peak with no external upturn (see Figure 1.10).

The physical interpretation of these different shapes come singles out the long-term effect of dynamical friction acting on the cluster binary population (and its progeny) since the early stages of cluster evolution. In fact, what we call MT-BSS today is the by-product of the evolution of a $\sim 1.2 M_{\odot}$ binary that has been orbiting the cluster and suffering the effects of dynamical friction for a significant fraction of the cluster lifetime. The efficiency of dynamical friction decreases for increasing radial distance from the centre, as a function of the local velocity dispersion and mass density. Hence, dynamical friction first segregates (heavy) objects orbiting close to the centre and produces a central peak in their radial distribution. As the time goes on, the effect extends to larger and larger distances, thus yielding to a region devoid of these stars (i.e., a dip in their radial distribution) that progressively propagates outward. Simple analytical estimate of the radial position of this dip turned out to be in excellent agreement with the position of the minimum in the *observed* BSS radial distributions ($r_{\rm min}$), despite a number of crude approximation (see, e.g., Mapelli

et al., 2006). Moreover, a progressive outward drift of $r_{\rm min}$ as a function of time is confirmed by the results of direct N-body simulations that follow the evolution of $\sim 1.2 M_{\odot}$ objects within a reference cluster over a significant fraction of its lifetime.

In light of these considerations, the three families defined in Figs. 1.8–1.10 correspond to GCs of increasing dynamical ages. Hence, the shape of the BSS radial distribution turns out to be a powerful dynamical-age indicator. A flat BSS radial distribution (consistent with that of the reference population; see *Family I* in Fig. 1.8) indicates that dynamical friction has not played a major role yet even in the innermost regions, and the cluster is still dynamically young. This interpretation is confirmed by the absence of statistically significant dips in the BSS distributions observed in dwarf spheroidal galaxies (Mapelli et al., 2009; Monelli et al., 2012): these are, in fact, collisionless systems where dynamical friction is expected to be highly inefficient. In more evolved clusters (*Family II*), dynamical friction starts to be effective and to segregate BSSs that are orbiting at distances still relatively close to the centre: as a consequence, a peak in the centre and a minimum at small radii appear in the distribution, while the most remote BSSs are not yet affected by the action of dynamical friction (this generates the rising branch of the observed bimodal BSS distributions; see upper panel in Fig. 1.9). Since the action of dynamical friction progressively extends to larger and larger distances from the centre, the dip of the distribution progressively moves outward (as seen in the different groups of *Family II* clusters; Fig. 1.9, panels from top to bottom). In highly evolved systems dynamical friction already affected even the most remote BSSs, which started to gradually drift toward the centre: as a consequence, the external rising branch of the radial distribution disappears (as observed for *Family III* clusters in Fig. 1.10). All GCs with a single-peak BSS distribution can therefore be classified as "dynamically old".

Interestingly, this latter class includes M30 (see Section 1.3.1), a system that already suffered core collapse which is considered as a typical symptom of extreme dynamical evolution (e.g., Meylan & Heggie, 1997). The proposed classification is also able to shed light on a number of controversial cases debated into the literature. In fact, M4 turns out to have an intermediate dynamical age, at odds with previous studies suggesting that it might be in a PCC state (Heggie & Giersz, 2008). On the other hand, NGC 6752 turns out to be in a quite advanced state of dynamical evolution, in agreement with its observed double King profile indicating that the cluster core is detaching from the rest of the cluster structure (Ferraro et al., 2003a). Finally this approach might provide the key to discriminate between a central density cusp due to core collapse (as for M30) and that due to the presence of an exceptional concentration of dark massive objects (neutron stars and/or the still elusive intermediate-mass black holes; see the case of NGC 6388, Lanzoni et al., 2007a, 2013, and references therein).

The quantization in distinct age-families is of course an over-simplification, while

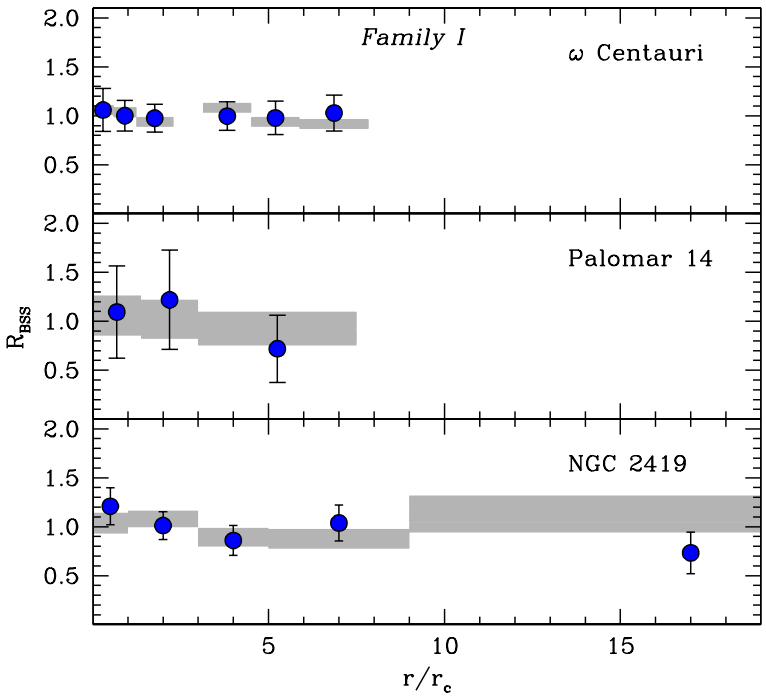

Figure 1.8: BSS radial distribution observed in ω Centauri, Palomar 14 and NGC 2419, with the blue circles marking the values of $R_{\rm BSS}$, defined in eq. (1.1). The distribution of the double normalized ratio measured for RGB or HB stars is also shown for comparison (grey strips). The BSS radial distribution is flat and totally consistent with that of the reference population, thus indicating a low degree of dynamical evolution for these three GCs (*Family I*). From Ferraro et al. (2012).

the position of $r_{\rm min}$ is found to vary with continuity as a sort of clock time-hand. This allowed Ferraro et al. (2012) to define the first empirical clock able to measure the dynamical age of a stellar system from pure observational quantities (the *"dynamical clock"*): as the engine of a chronometer advances the clock hand to measure the time flow, in a similar way the progressive sedimentation of BSSs towards the cluster centre moves $r_{\rm min}$ outward, thus marking its dynamical age. This is indeed confirmed by the tight correlations found between the clock-hand ($r_{\rm min}$) and the central and half-mass relaxation times ($t_{\rm rc}$ and $t_{\rm rh}$, respectively), which are commonly used to measure the cluster dynamical evolution time-scales. The trend with $t_{\rm rc}$ found by Ferraro et al. (2012) is shown in Figure 1.11 and the best-fit relations is:

$$\log(t_{\rm rc}/t_{\rm H}) = -1.11 \times \log(r_{\rm min}) - 0.78 \qquad (1.2)$$

where $t_{\rm H}$ is the Hubble time. Note that, while $t_{\rm rc}$ and $t_{\rm rh}$ provide an indication of the relaxation timescales at specific radial distances from the cluster centre ($r_{\rm c}$ and $r_{\rm h}$, respectively), the dynamical clock here defined provides a measure of the global dynamical evolution of the systems, because the BSS radial distribution simultaneously

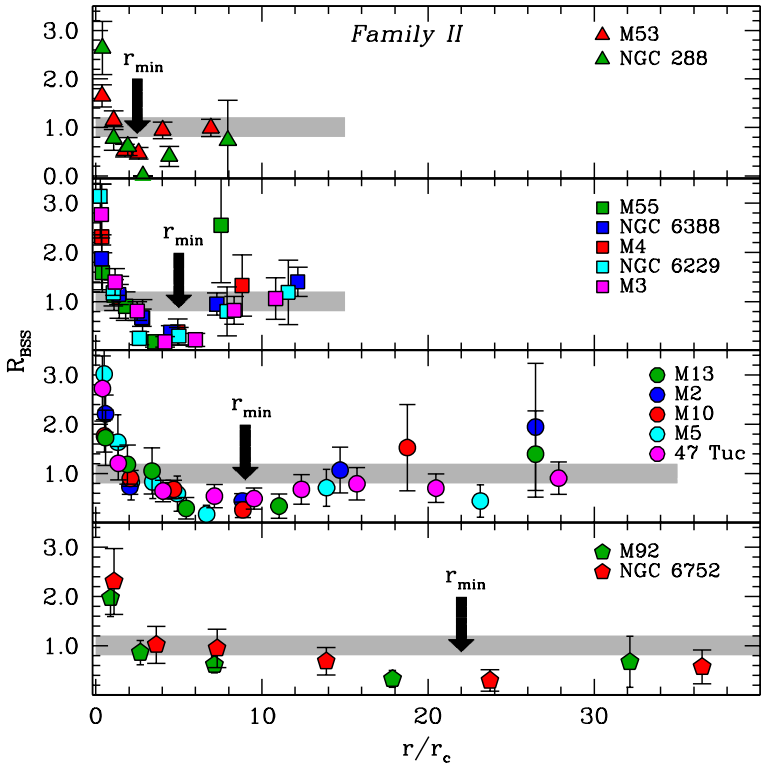

Figure 1.9: BSS radial distribution observed in clusters of intermediate dynamical age (*Family II*). The distribution is clearly bimodal and the radial position of the minimum (marked with the arrow and labelled as $r_{\rm min}$) clearly moves outward from top to bottom, suggesting that the bottom clusters are more dynamically evolved than the upper ones. For the sake of clarity, the grey bands schematically mark the distribution of the reference populations. From Ferraro et al. (2012).

probes all distances from the cluster centre.

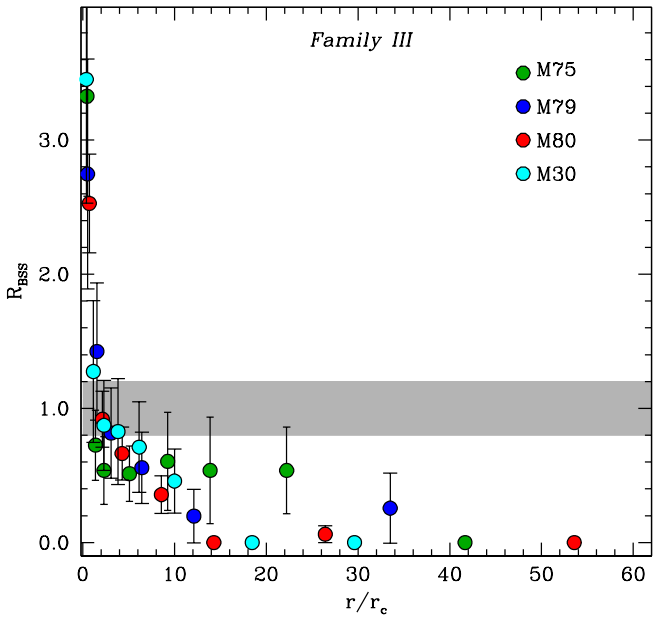

Figure 1.10: BSS radial distribution for dynamically old clusters (*Family III*): only a central peak is visible, while the external upturn is no more present because, within the proposed scenario, the dynamical friction has been efficient out to the cluster outskirts. From Ferraro et al. (2012).

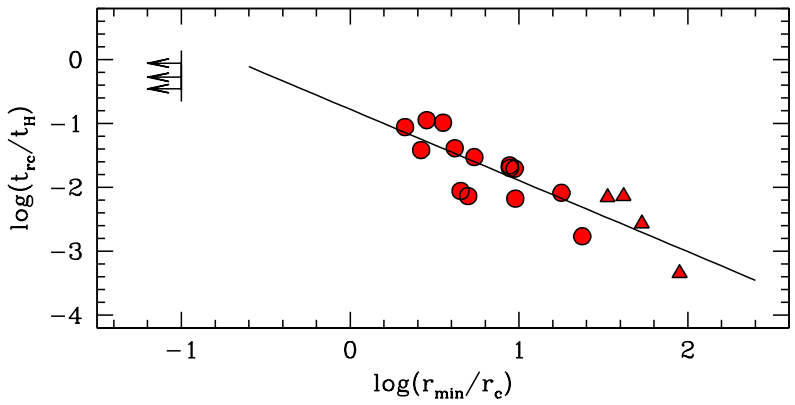

Figure 1.11: Core relaxation time (normalized to the Hubble time t_H) as a function of the time hand of the proposed *dynamical clock* ($r_{\rm min}$, in units of the core radius). Dynamically young systems (*Family I*) show no minimum and are plotted as lower-limit arrows at $r_{\rm min}/r_c = 0.1$. For dynamically old clusters (*Family III*, triangles), the distance of the farthest radial bin where no BSSs are observed has been adopted as $r_{\rm min}$. As expected for a meaningful clock, a tight anticorrelation is found: clusters with relaxation times of the order of the age of the Universe show no signs of BSS segregation (hence their BSS radial distribution is flat and $r_{\rm min}$ is not definable; see Fig. 1.8), whereas for decreasing relaxation times the radial position of the minimum increases progressively. The solid line correspond to the best-fit relations, given in eq. (1.2). From Ferraro et al. (2012).

Chapter 2

Dynamical Friction time scale in multi-component evolved GCs

2.1 Introduction

GCs are multi-mass systems, in the sense that they contain stars with different masses. MS stars have masses in the range $[0.1, m_{\rm TO}]$, where $m_{\rm TO}$ is the TO mass, representing the mass of the most massive stars still experiencing the hydrogen-burning phase; for today GCs, $m_{\rm TO} \simeq 0.8 - 0.9 M_{\odot}$. Moreover, they contain the *dark product* of the stellar evolution, with all the stars that had an initial mass larger than $m_{\rm TO}$: white dwarfs (WDs), neutron stars (NSs) and stellar mass black holes (BHs), with masses in the range $\approx [0.2, 1.0] M_{\odot}$, $\approx [1.3, 2.5] M_{\odot}$ and $\approx [2.5, 20] M_{\odot}$, respectively. So, GCs contain stars covering a quite large mass interval ($[0.1 - 20] M_{\odot}$).

Concerning the DF process, it has been extensively investigated by Chandrasekhar (1943) in the case of a test particle moving in an infinite and homogeneous background field. Then, by taking into account that multi-mass systems behave, dynamically, quite differently with respect to systems composed by particles with the same mass, both in terms of processes involved and of time-scales on which they occur, many authors have extended the Chandrasekhar's framework to other more realistic physical cases, with different assumptions or different and more sophisticated methods (Chandrasekhar & von Neumann, 1942, 1943; White, 1949; Thorne, 1968; Lee, 1969; Binney, 1977; Tremaine & Weinberg, 1984; Ostriker, 1999; Ciotti & Binney, 2004; Nipoti et al., 2008). From the astrophysical point of view, it is clear that DF plays an important role on different scales, from galaxy clusters and their cD galaxies (e.g., Ostriker & Tremaine, 1975; White, 1976; Binney, 1977; Dressler, 1979; Kashlinsky, 1987; Nipoti et al., 2004; Kim, El-Zant & Kamionkowski, 2005; El-Zant, 2008), to galaxies and their GC systems (e.g., Tremaine, Ostriker & Spitzer, 1975; Bontekoe

& van Albada, 1987; Bertin, Liseikina & Pegoraro, 2003, 2004; Capuzzo-Dolcetta & Vicari, 2005; Arena et al., 2006; Mastrobuono-Battisti & Capuzzo-Dolcetta, 2012; Arca-Sedda & Capuzzo-Dolcetta, 2014), to binary BHs at the center of early-type galaxies (e.g., Fukushige, Ebisuzaki & Makino, 1992; Vecchio, Colpi & Polnarev, 1994; Milosavljević & Merritt, 2001).

It is clear that in the above mentioned cases the following assumptions are fully justified:

(i) the mass of the test particle is much larger than the mass of the field ones ($m_t \gg m$). This is a realistic situation, for example, when studying the sinking of GCs in galaxies ($m_{\rm GC} \simeq 10^5 M_\odot \gg m_* \simeq 1 M_\odot$, where $m_{\rm GC}$ and m_* are, respectively, the typical mass of GCs and that of a star in a galaxy).

(ii) the field particles all have the same mass. This assumption becomes realistic if the previous condition is verified: when the test particle is much more massive than the field ones, the background can be safely approximated by stars with mass equal to their average value.

Instead the case of BSSs in GCs is a significant exception to points *(i)* and *(ii)*, being the mass of the test particle only slightly (2-3 times) larger than that of the field stars, so that taking into account a mass spectrum for the background can make significant differences. Moreover, real GCs are composed of stars in a relatively large range of masses ($0.1 - 20\ M_\odot$; see above), then also assumption *(ii)* is not strictly valid. Finally, it should be noticed that in general (e.g., Bertin, 2000), the ratio between the DF and the two-body relaxation times is given by: $t_{\rm DF}/t_{\rm 2b} \propto 2m/(m_t + m)$. Hence, while in the case of massive objects DF effects manifest on time-scales shorter than the two-body relaxation time of the system ($t_{\rm 2b}$), for comparable masses these effects occur on quite long times, with the tendency to mix with two-body relaxation time effects. All these considerations make the problem of modeling the DF action on BSSs in a GC more complex.

For the reasons above, it is not surprising that the case in which the field particles have a mass spectrum has not been extensively investigated in the literature. A notable exception is the work by Ciotti (2010), who showed that the DF time-scale in a system with a mass spectrum can be shorter (i.e., DF stronger) up to a factor of 2 or 3, with respect to the case of a single-mass system with the same average density and the same total mass. Hence, the considerations presented in Ciotti (2010) for a homogeneous and infinite density background with a mass spectrum, coupled with the well known dynamical evolution of a multi-mass GC (e.g., Spitzer 1987), prompted us to investigate in more detail the problem. In fact, the dynamical evolution of the parent GC leads to a radially dependent stratification of masses for the background stars (due to mass segregation), so that, in practice, each radius is characterized by a different mass function, leading to a radially dependent DF

strength. Moreover, it should be noted that, if a sort of equipartition is established in the background particles, then some additional non trivial effect due to their velocity distributions may take place (Ciotti, 2010). For example, in the case of a bottom-heavy mass spectrum, on one side the low-mass population can have a higher density than that of high-mass stars (thus providing a proportionally larger contribution to the total DF), but, from the other side, the velocity of the light particles is also higher, so that their contribution to DF is reduced, in a compensating effect. Since DF depends on the "local" conditions of the system, in terms of both density and velocity distribution, it is not trivial to predict the final effect on the test particle due to the interplay between the various mass-components in the cluster. Furthermore, the dynamical evolution of a GC produces significant changes on these distributions in time (e.g., during and after the core-collapse stage), which, in turn, depend on the component stellar mass, too. Hence the problem of modeling the DF on (the slightly heavier than average) BSSs in a dynamically evolving (multi-mass) GCs is a quite complex task. Therefore, what really happens to the BSS population in a GC can be analyzed only by considering the combined effects, at each radius, of both a radially and a time dependent mass spectrum obtained (for example) by N-body simulations, in a self-consistent way.

Within this context, we investigate here the multifaceted nature of DF on test particles slightly heavier than average field particles in a dynamically evolving system with a mass spectrum, combining the approach described in Ciotti (2010) with a set of numerical N-body simulations. In particular the main aim is answering the following question: *could the DF time-scale develop a non-monotonic radial behavior at some time during the cluster evolution?* In fact, if $t_{\rm DF}$ develops a minimum at a given radius $r_{\rm min}$, the BSSs orbiting at that distance from the center would suffer from an enhanced drag force with respect to the other BSSs orbiting at different radii, and a minimum in the BSS radial distribution would therefore appear at $r_{\rm min}$ (i.e., at a place and time different from what expected in the "dynamical clock" framework, therefore affecting the possibility to use the distribution of BSSs as a simple clock). The answer to this question could provide an additional explanation to the observed variety of BSS radial distributions.

In Section 2.2 we introduce the analytic approach to the problem of DF. In Section 2.3, we outline the mono-mass and multi-mass N-body simulations used to describe the background field component. The results are discussed in Section 2.4.

2.2 Analytical background

2.2.1 Mono-mass case

In order to introduce the case of a mass spectrum, we begin by recalling the relevant aspects of DF in the standard case of a background made by identical scattering masses m; this case is a useful benchmark which allows to better identify the mass-spectrum effects on DF. The deceleration of a test particle of mass m_t, moving with velocity $\mathbf{v}_t$ and modulus v_t in a homogeneous background of particles of equal mass m, constant number density n, and isotropic velocity distribution $f(\mathbf{v})$, under the effect of DF can be written as

$$\frac{d\mathbf{v}_t}{dt} = -4\pi G^2 \ln\Lambda \; n \; m(m+m_t) \; \Xi(v_t) \frac{\mathbf{v}_t}{{v_t}^3}, \tag{2.1}$$

where G is the gravitational constant, $\Xi(v_t)$ is the fraction of particles slower than v_t and $\ln\Lambda$ is the velocity weighted Coulomb logarithm (Chandrasekhar, 1943, 1960; Binney & Tremaine, 2008; Bertin, 2000). By definition, $\Xi(0) = 0$ and $\Xi(\infty) = 1$: we recall that the sharp truncation of the function Ξ for velocities larger than v_t is an approximation (not affecting our discussion) due to the assumption of velocity isotropy of the background and to the use of the lowest order term in the impulsive approximation adopted to compute the two-body interactions. It is well known that several problems affect the direct application of eq. (2.1) to spherical systems, as a local description of DF (Bontekoe & van Albada, 1987; Bertin, Liseikina & Pegoraro, 2003, 2004; Arena et al., 2006). Nonetheless several studies have been based on the applications of eq. (2.1) to spherical systems.

Here we follow the same approach, for the case of interest (i.e., that of the evolution of the BSS population in a GC), and take into account the radial dependence of the number density by replacing n with $n(r)$. In addition, in all our discussion we assume the test particle to be on circular orbit in the GC potential well, so that also v_t depends on r:

$$v_t(r) = \sqrt{G\frac{M(r)}{r}}, \tag{2.2}$$

where $M(r)$ is the total mass of the system enclosed within a sphere of radius r. From these assumptions, it follows that also the function Ξ depends only on the radial distance from the center through $v_t(r)$ and the local velocity distribution of the field particles. As usual, from eq. (2.1) we can define the characteristic DF times-scale as

$$t_{\rm DF} \equiv \frac{v_t}{|d\mathbf{v}_t/dt|}, \tag{2.3}$$

so that in our case

$$t_{\rm DF}(r) = \frac{v_t^3(r)}{4\pi G^2 \rho(r)(m+m_t)\Xi(r)\ln\Lambda} \tag{2.4}$$

where $\rho(r) = n(r)m$ is the mass density of the background. This expression explicitly shows that the radial dependence of the DF time-scale is shaped by three functions: the velocity of the test particle, $v_t(r)$, the mass density of the field stars, $\rho(r)$, and the relative number of stars moving slower than v_t at any radius, $\Xi(r)$. For simplicity, we neglect the possible dependence of Λ on radius: at the present level of approximation this seems a reasonable assumption, due to the logarithmic nature of the associated term. Note that the function $\Xi(r)$ is sometimes evaluated analytically by assuming a local Maxwellian velocity distribution for the background particles, determined by the value of the local velocity dispersion (e.g., Binney & Tremaine 2008). Here however we avoid this additional assumption, as we compute the function $\Xi(r)$ directly by counting the number of particles moving slower than v_t in the N-body simulation outputs (see Section 2.3).

2.2.2 Multi-mass case

As described in the Introduction, this study is focused on the case of a system made by the superposition of different mass components, such as a GC with stars distributed according to a prescribed mass spectrum. Ciotti (2010) showed that in such circumstances the DF experienced by a test particle can be significantly different from that experienced in a single-mass background. Therefore, the natural question arises of what happens in a GC, where the mass spectrum is associated to the initial mass function (IMF), and the dynamical evolution of the GC leads to a redistribution (through the tendency to equipartition, e.g. Spitzer 1987) of the density and velocity profiles of the different mass components. It is easy to realize that all these trends, weighted by the ratio between the mass of a BSS and the mass of the field stars in each subcomponent of the cluster, could lead to a quite complicate radial trend of the total DF.

In the presence of field particles with a mass spectrum, the total DF deceleration can be split in the individual contributions due to each single population. The i^{th} population causes a deceleration of the test particle which is again expressed by eq. (2.1);

$$\frac{d\mathbf{v}_t}{dt}^{i}(r) = -4\pi G^2 \ln\Lambda_i \ \rho_i(r)(m_i + m_t) \ \Xi_i(v_t)\frac{\mathbf{v}_t}{{v_t}^3}, \tag{2.5}$$

where now $\rho_i(r) = n_i(r)m_i$ is the local density of the background component with stellar mass m_i. Due to the additive nature of scattering effects in the Chandrasekhar treatment of DF, the total deceleration is obtained from the sum of all the contributions. In particular, from eqs. (2.3) and (2.5) it follows that:

$$\frac{1}{t_{\rm DF}(r)} = \sum_{i=1}^{N_{\rm pop}} \frac{1}{t^i_{DF}(r)}, \tag{2.6}$$

where

$$t^i_{DF}(r) = \frac{v_t^3(r)}{4\pi G^2 \rho_i(r)(m_i + m_t)\Xi_i(r) \ln \Lambda_i}. \quad (2.7)$$

In eq. (2.6) we assumed that the mass spectrum of the background stars is represented by the sum of a finite number of components ($N_{\rm pop}$). However eq. (2.6) can be easily written as an integral in the case of a continuous mass spectrum (Ciotti, 2010). As a general comment, note that eq. (2.6) indicates that the local value of the DF time is roughly determined by the smallest among the various $t^i_{DF}(r)$.

So far, the description in this Section just reflects the "standard" approach to our problem: namely, one could construct an equilibrium model for a GC (for example by solving numerically the Poisson equation for one- and multi-component King (1966) or Wilson (1975) models), take the radial profile of $n_i(r)$ and the local velocity distribution and compute eq. (2.7). Here, we follow a more realistic approach, namely we make use of (collisional) N-body simulations of a set of mono- and multi-mass GC models, capable to provide us with the self-consistent radial behaviors of all the various quantities needed to evaluate eq. (2.7). This approach, at variance with the solution of the Poisson problem, allows us to take into account also the time evolution of the $t_{\rm DF}$ radial profile.

2.3 N-body simulations

Here we describe the set-up of the N-body simulations performed in order to determine the time evolution of the GC models hosting the BSS population. Since GCs are collisional systems, very accurate and specifically designed numerical methods are required to properly describe their time evolution. In practice, we use direct N-body simulations to obtain a self-consistent description of the phase-space density distribution of the different components of the GC, and then we apply the equations presented in Section 2.2 to estimate the radial trend of $t_{\rm DF}$. We also perform some simulation where the background stars are all characterized by the same mass, so that the effects of a mass spectrum can be better appreciated through comparison. For our simulations we used the direct N-body code `NBODY6` (Aarseth, 2003). In all cases, the simulations are not meant to describe the evolution of a GC from its formation to the present days. They just provide a simplified “picture” of a current GC, which could be in a pre- or in a post-core collapse phase.

2.3.1 Mono-mass simulations

The mono-mass system is composed of $N = 10^4$ particles with mass m. The initial conditions (particle positions and velocities) have been generated from a King (1966) model with central dimensionless potential $W_0 = 4$. We followed the dynamical

evolution of the cluster up to a final time $t_f = 1000$ in N-body time units (i.e. in units in which the total mass of the cluster is $M = 1$, $G = 1$ and the total energy is $E = -1/4$, also known as 'Hénon' Units; see Aarseth, 2003, Sect. 7.4 and Heggie & Mathieu, 1986). A characteristic time scale for two-body relaxation is given by $t_{\rm rh}(0)$, the half-mass relaxation time of the initial conditions (e.g., Spitzer, 1987):

$$t_{\rm rh}(0) = 0.138N\sqrt{\frac{r_h(0)^3}{GM}}\frac{1}{\ln(0.4N)} = 2.2\,\frac{N}{\ln(0.4N)}\left(\frac{r_h(0)}{1\rm pc}\right)^{3/2}\left(\frac{1\rm M_\odot}{M}\right)^{1/2}[\rm Myr], \tag{2.8}$$

where $r_h(0)$ is the half mass radius (i.e., the radius containing half the total mass of the system) at the initial time $t = 0$. In N-body units $t_{\rm rh}(0) \simeq 210$ so that in practice we follow the GC evolution up to $t_f \simeq 4.8 t_{\rm rh}(0)$. To improve the statistics, 20 different sets of initial conditions have been generated by changing only the random seed from which the positions and velocities of the particles are extracted starting from the distribution function. All the realizations have then been combined at each time-step, shifting the center of mass of each system to a common origin. This procedure generated "*supersnapshots*" containing $N_{\rm super} = 2 \times 10^5$ particles. The simulations have been run on a dedicated workstation, and each simulation in the mono-mass case took approximately 3 hours (thanks to the use of a GPU card).

2.3.2 Multi-mass simulations

As described in Section 2.2, in order to determine the time evolution of the radial trend of $t_{\rm DF}$ for the population of BSSs in a multi-mass GC, we need the distribution function of each stellar component of the cluster, i.e., the associated density profile and its velocity distribution. Of course, some educated guess could be used to describe the radial profile of the velocity distribution (e.g., to solve the associated Jeans equations and use the resulting velocity dispersion in the local Maxwellian approximation), but here we prefer to use direct N-body simulations that allow to compute in a self-consistent way the evolution of the structural and dynamical properties of the different components.

The modelization of a mass-spectrum with a necessarily limited number of particles imposes some constrain in the choice of the number of mass bins. Of course, the larger is the number of bins, the finer is the spectrum. However, to avoid too little numbers of particles in each bin as a consequence of an excessive partition among the field particles, as well as to understand more clearly the contribution of the various mass ranges (at the various radii) to the resulting DF, we represent the mass spectrum as the superposition of three different populations with a total number of stars N_1, N_2, and N_3. The masses of the individual stars in each population are m_1, m_2, and m_3 respectively, with m_1 being the smallest value, $m_2 = 2m_1$ and $m_3 = 3m_1$. Therefore, $N = N_1 + N_2 + N_3$ and $m_1 = M/(N_1 + 2N_2 + 3N_3)$, where M is the

total mass of the cluster. The three populations are aimed at grossly representing the main populations of field stars in a present-day GC, namely low-MS stars (with mass $m_1 \simeq 0.3M_\odot$), intermediate-MS objects ($m_2 \simeq 0.6M_\odot$), and TO and giant stars ($m_3 \simeq 0.9M_\odot$). As in the mono-mass simulations, the total initial number of stars is $N = 10^4$, with the three components counting $N_1 = 8500$, $N_2 = 1200$ and $N_3 = 300$ particles, respectively. This choice is a reasonable compromise between the description of a realistic case, and the need of a large statistical sampling for the less numerous population (m_3) in order to avoid noise-dominated results.

The initial positions and velocities of all particles in each of the three groups are randomly extracted from the same King (1966) distribution function, i.e., no initial mass segregation is assumed. This choice is made both to avoid an additional degree of freedom (an unconstrained amount of mass segregation) and because it is justified by the flat BSS distribution observed in ω Cen, Palomar 14, NGC 2419 and NGC6101 (see Ferraro et al., 2012; Dalessandro et al., 2015, and Chapter 1). The system is also fully isolated, with no primordial populations of binaries or multiple systems.

In order to improve the statistics, as in the mono-mass case, we generated 20 sets of initial conditions by varying only the random seed and we combined all the runs together at every extracted snapshot, thus generating supersnapshots made of $N_{\rm super} \simeq 2 \times 10^5$ stars (this number varies slightly during the evolution due to the loss of unbound particles). All the simulations have been stopped at the time $t_f \simeq 10 t_{\rm rh}(0)$, with $t_{\rm rh}(0) = 190$ in N-body units. In these multi-mass cases, the half-mass relaxation time is again computed by using eq. (2.8). We extracted a snapshot every $5 \times 10^{-3} t_{\rm rh}(0)$, thus we have guaranteed a good accuracy in tracking the cluster evolution. Three different values of the King dimensionless potential ($W_0 = 4, 6, 8$) have been considered for the multi-mass simulations, so in total we ran 60 simulations in the multi-mass case.

2.4 Results

2.4.1 Mono-mass case

In the mono-mass case, the DF time-scale of a test particle of mass $m_t = 4m$ (m being the mass of the background stars) has been evaluated by using eq. (2.4). In order to extract from the simulations the radial profiles of $v_t(r)$, $n(r)$ and $\Xi(r)$ entering eq. (2.4), we considered equally populated radial bins (i.e., 100 concentric spherical shells, each enclosing 2000 particles of a given supersnapshot). This choice has the useful property of maintaining constant the error bars of the number density over the whole radial range, thus reducing the effects of random fluctuations. This choice also implies a finer sampling of the innermost regions as the time passes,

because the density progressively increases in the core of the GC. The number density profile of the field component, $n(r)$, is then given by the number of particles in each radial bin divided by the volume of the shell. The circular velocity of the test particle, $v_t(r)$, is trivially computed by using eq. (2.2). Finally, the local estimate of $\Xi(r)$ in each radial bin is obtained by normalizing the number of background particles in the given radial bin that are slower than $v_t(r)$, to the total number of background particle in the same bin.

The resulting radial trend of $t_{\rm DF}$ at four representative times is shown in fig. 2.1, where the radial distance is expressed in units of the half-mass radius at that time $r_h(t)$, and the time is normalized to the *instantaneous* half-mass relaxation time, $t_{\rm rh}(t)$. Fig. 2.1 clearly shows that $t_{\rm DF}$ maintains a monotonic radial trend at increasing time, in agreement with simple expectations. We see also that, as the dynamical evolution of the system proceeds, $t_{\rm DF}$ decreases (i.e., DF becomes more efficient) in the central and external regions, while the effect is opposite at intermediate radii. This behavior is mainly due to the time evolution of the mass density (see fig. 2.3), which progressively increases with time in the innermost and outermost regions, (the former being due to the core-contraction, the latter due to the related cluster halo expansion), while it tends to decrease on the radial interval $-0.3 \lesssim log(r/r_h) \lesssim 0.3$ (consistently with an evolution towards a higher cluster concentration, resulting in a decrease of r_h). Indeed the density profile is the primary driver of the shape of $t_{\rm DF}(r)$ at all times, while the other terms entering eq. (2.4) provide a negligible contribution. This is due to a more significant evolution of $\rho(r) = m\, n(r)$ with respect to those of $\Xi(r)$ and $v_t^3(r)$, as is clearly apparent in fig. 2.2. Therefore, the mono-mass simulations show that a radial non-monotonicity of $t_{\rm DF}$ cannot explain the observed BSS-nRDs and confirm the scenario adopted by Ferraro et al. (2012) where the cause is, instead, a monotonic increase of the radius at which the cluster age coincides with $t_{\rm DF}(r)$.

2.4.2 Multi-mass case

In the multi-mass case, the DF time-scale has been computed by evaluating each term in eq. (2.6) associated to each one of the three stellar components considered in the simulations described in Sect. 2.3.2, and by setting the BSS mass at $m_t = 4m_1$. To avoid large fluctuations due to the low number statistics of the most massive component (which counts only 3% of the total number of particles), the radial binning has been chosen by imposing that at least $\simeq 200$ stars of mass m_3 are included in each shell and that the total number of bins is always $N_{\rm bin} \geq 19$. Thus, at odds with the mono-mass case, the total number of particles in each shell is not constant. The number density profile of each mass component, $n_i(r)$, has been computed as in the mono-mass case (see Sect. 2.4.1), while the circular velocity of the test particle, is again trivially computed from eq. (2.2). The velocity factors

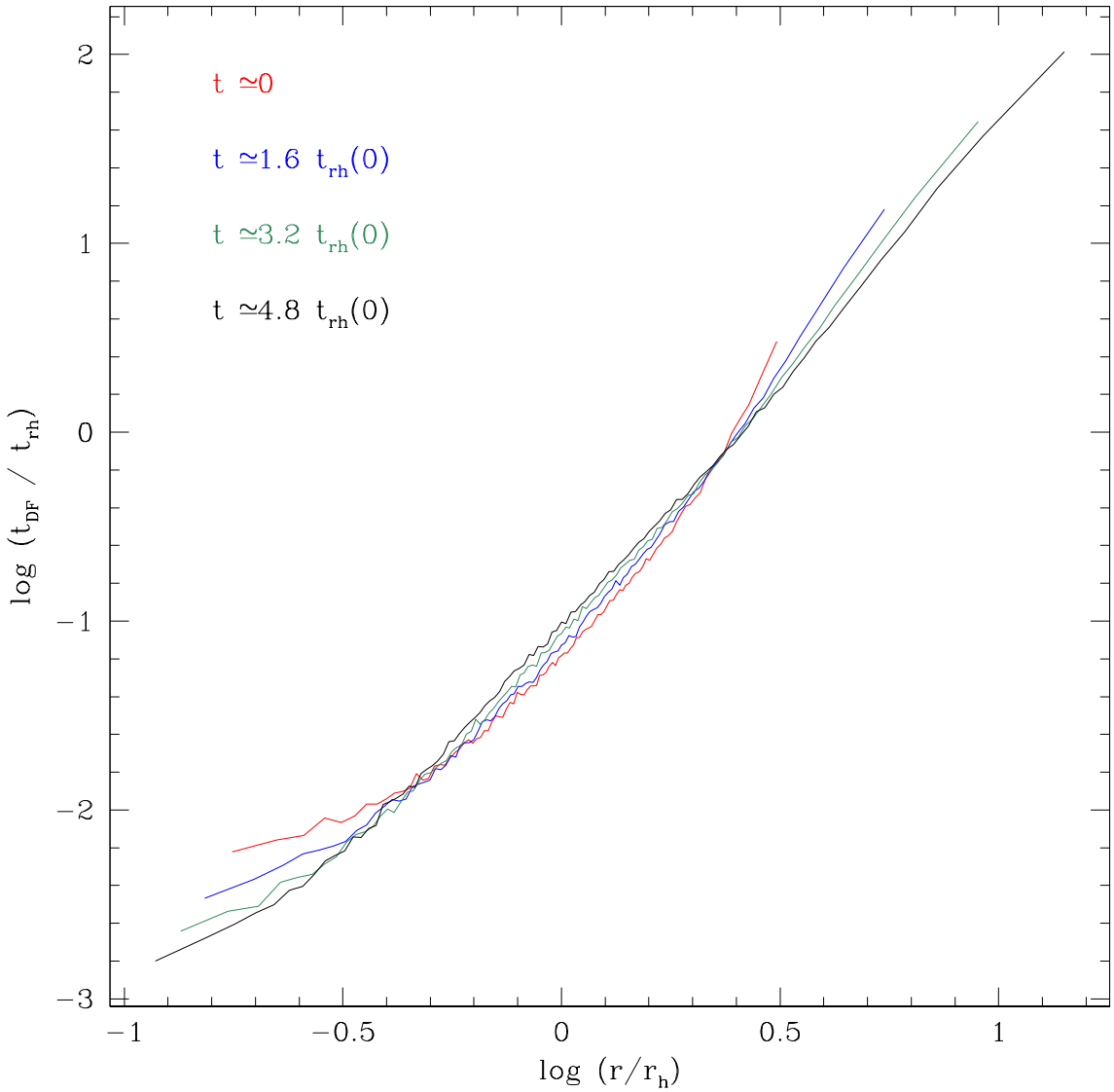

Figure 2.1: Time evolution of the radial profile of the DF time-scale, $t_{\rm DF}$, for the mono-mass system with central dimensionless potential $W_0 = 4$. The four curves correspond to four different times of the simulation (see labels), from $t = 0$ to the final time $t_f = 4.8\ t_{\rm rh}(0)$. As explained in the text, the DF time-scale is normalized to the instantaneous half-mass relaxation time, while the radius is in units of the instantaneous half-mass radius r_h. The increase of the probed radial range at large radii with time is due to the decrease of r_h, while in the central regions the different extension is due to the fixed number of stars assumed to define the radial bins (see the text).

$\Xi_i(r)$ in each radial bin have been computed by normalizing the number of stars in the i^{th} mass group that move slower than $v_t(r)$, to the total number of particles of the same mass group in that radial bin.

The results obtained for the three considered values of the dimensionless potential ($W_0 = 4, 6, 8$) and four different times are plotted in fig. 2.4. In particular, we show $t_{\rm DF}(r)$ at the initial time of the simulation ($t = 0$) and for three snapshots around

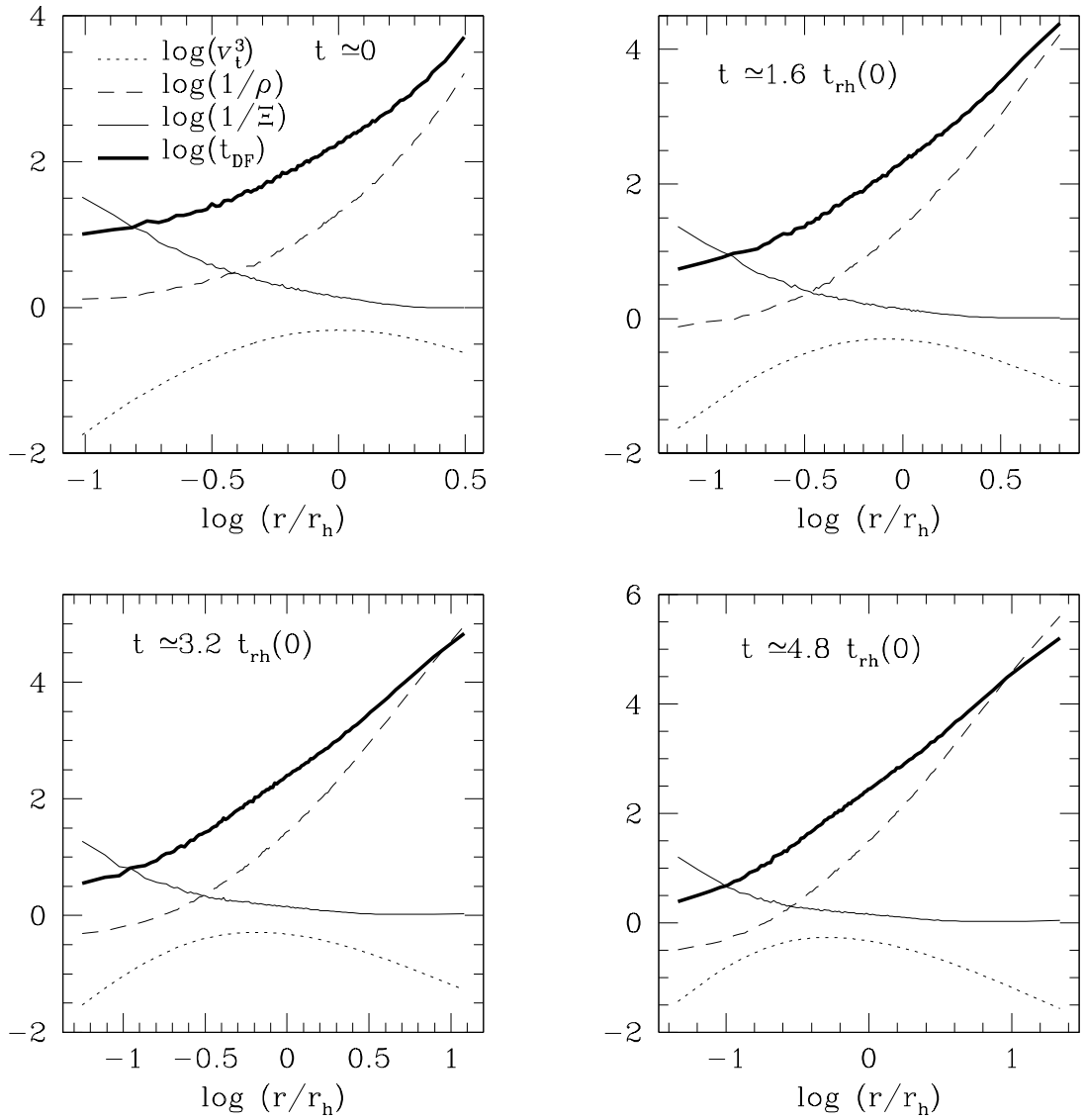

Figure 2.2: Mono-mass case. Radial trend of the DF time-scale (thick solid line, eq. 2.4) at the four representative times in Figures 2.1 and 2.3. In the plots we also show the three radially dependent terms contributing to the final value of $t_{\rm DF}$ (v_t^3: dotted line, $1/\rho$: dashed line, $1/\Xi$: thin solid line). All quantities are given here in code units, and from eq. (2.4) it follows that $log(t_{\rm DF})$ is just given (modulo an additive constant) by the sum of the three quantities.

the "core-collapse time" $t_{\rm cc}$, defined as the time at which the Lagrangian radius r_{10} (i.e., the radius containing 10% of the total mass) reaches its minimum value. For reference, we notice that $t_{\rm cc} \simeq 3.6\ t_{\rm rh}(0), 2.5\ t_{\rm rh}(0), 0.6\ t_{\rm rh}(0)$ for $W_0 = 4, 6, 8$, respectively. The radial behavior of the DF time-scale is plotted both for each mass-component separately (color lines), and combining the effects of the three background mass components according to eq. (2.6) (thick black lines).

Since the initial conditions for all mass-groups were built from the same King model properly scaled only for the adopted number of stars, at $t = 0$ the radial

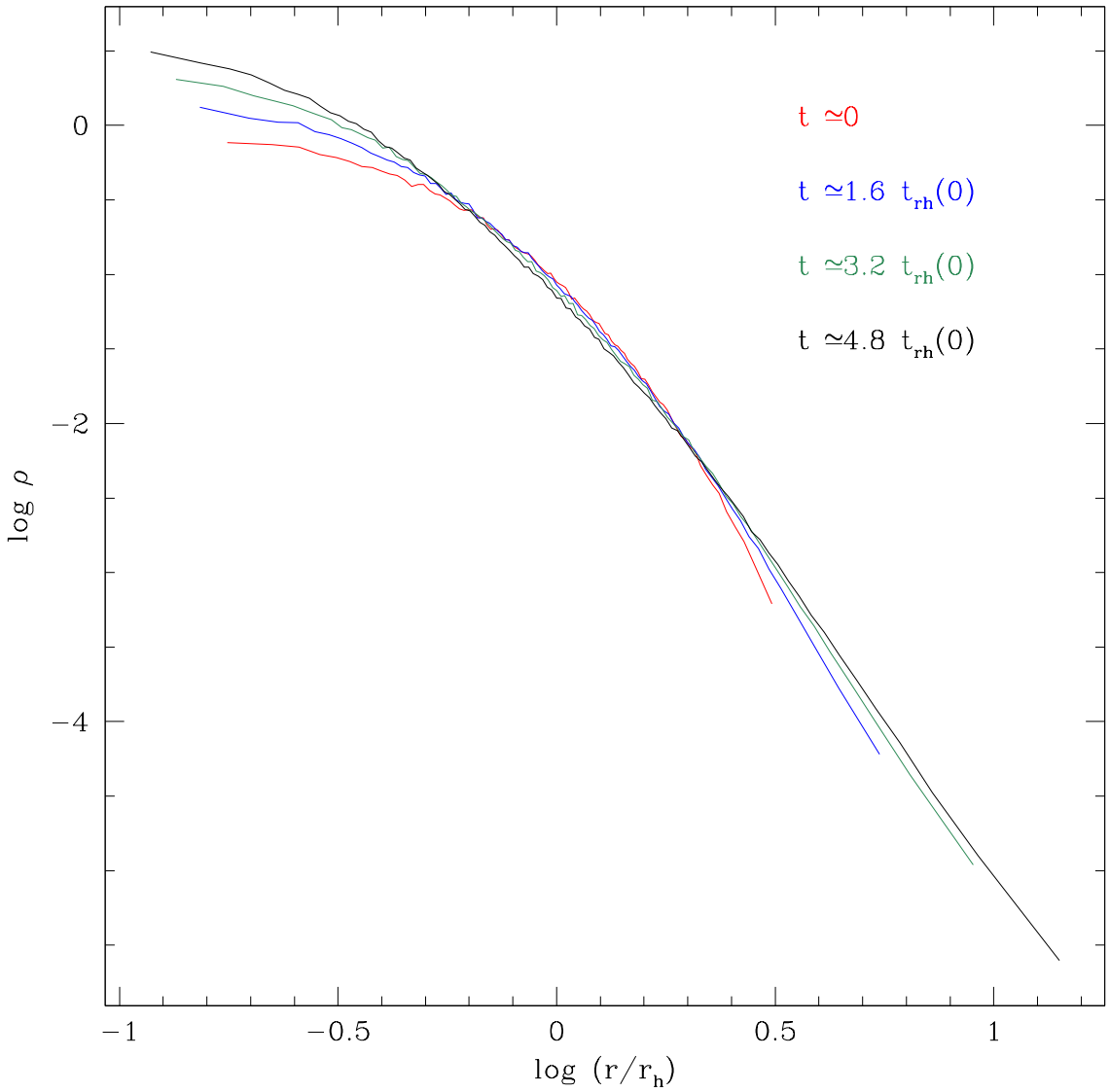

Figure 2.3: Time evolution of the background mass density profile $\rho(r)$ of the cluster from the initial time $t = 0$ to the final time $t_f = 4.8\ t_{\rm rh}(0)$, in the mono-mass case derived from the initial conditions with $W_0 = 4$.

profile of $t_{\rm DF}$ has the same qualitative behavior for any group and its value at any radial distance decreases for decreasing particle mass, because lighter stars are by far the most numerous and thus dominate the local mass density.

At all evolutionary times, as for the mono-mass simulations, also in this case the mass density is the main driver in shaping $t_{\rm DF}(r)$: the local value of $t_{\rm DF}(r)$ is essentially determined by that of the dominant contributor to $\rho(r)$. In fact, due to energy equipartition, the most massive particles progressively migrate toward the center, while the lightest component expands outward. As a consequence the total mass density is mainly contributed by the heaviest mass-group at small radii, while

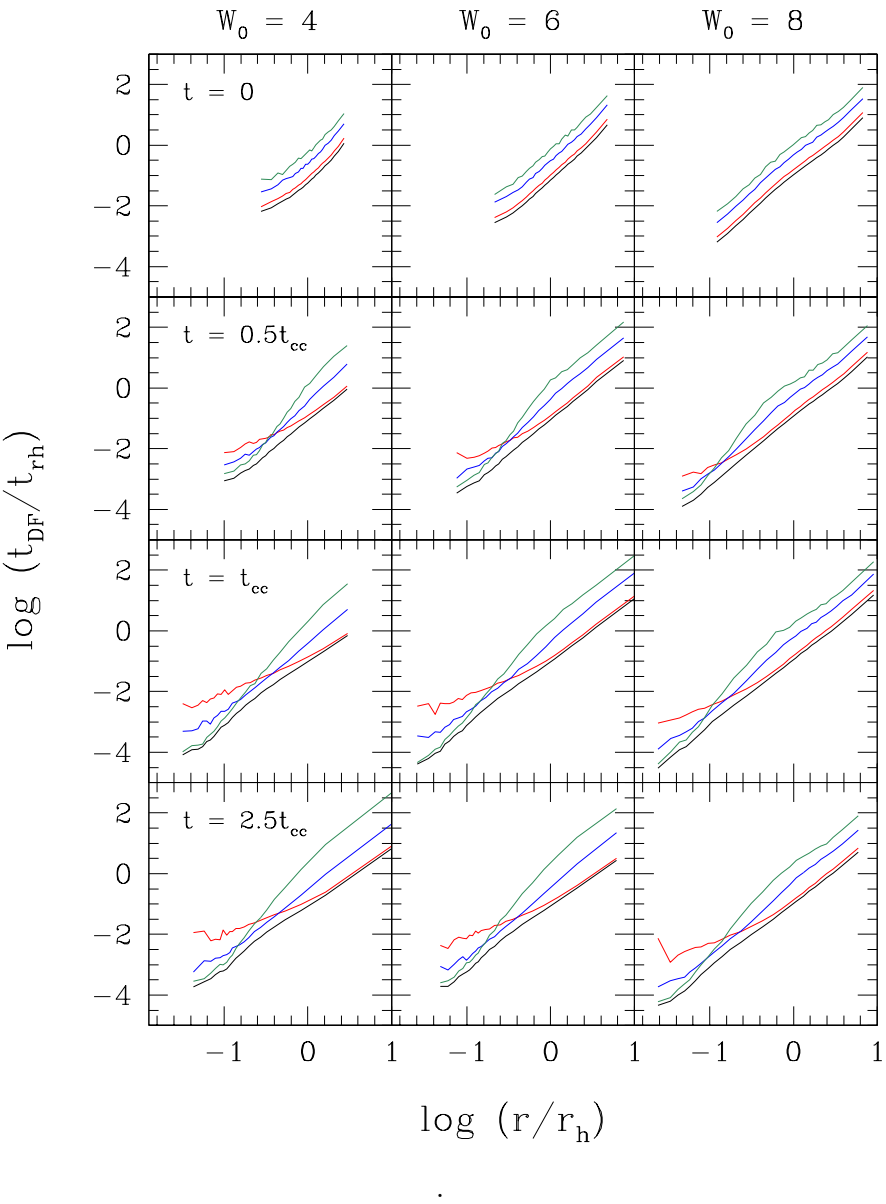

Figure 2.4: Radial profile of $t_{\rm DF}$ in the multi-mass simulations, plotted for each mass-component separately (red: m_1, blue: m_2, green: m_3) and from the combined effects of the three background mass components according to eq. (2.6) (black lines). The different panels are snapshots taken at $t = 0, 0.5, 1$, and 2.5 $t_{\rm cc}$, where $t_{\rm cc}$ is the fiducial core-collapse time of the system (see Section 2.4.2). Panels from left to right show, models with: $W_0 = 4$, 6, 8. The radial distance from the center and $t_{\rm DF}$ are normalized, respectively, to the instantaneous half-mass radius and the instantaneous half-mass relaxation time computed for the system as a whole.

it is dominated by the m_1 particles in the outskirts, and the radial profile of $t_{\rm DF}$ is thus driven by $1/\rho_3(r)$ and $1/\rho_1(r)$ in the two respective radial regions. In addition, from $t = 0$ to $t = t_{\rm cc}$, DF becomes increasingly more efficient in the center (i.e., the value of $t_{\rm DF}$ at fixed small radii becomes smaller) because also the central mass density increases, due to the segregation first of m_3 particles and then also of m_2

stars[1]. The increase of $t_{\rm DF}(r)$ at $t = 2.5\ t_{\rm cc}$, is due to a late re-expansion of the system (corresponding to a decrease of the mass density).

Fig. 2.4 also shows that the radial profile of $t_{\rm DF}$ is qualitatively the same for all values of W_0 (i.e., independently of the cluster concentration) and it always monotonically increases with radius, as in the mono-mass case. *Our simple analysis then shows that the presence of a mass spectrum does not induce non-monotonic behaviors in the DF time-scale.*

2.4.3 Equivalent Classical System

The previous analysis showed that a mass spectrum in a GC does not lead to a non-monotonic behavior of $t_{\rm DF}(r)$, so that the results are in qualitative agreement with the mono-mass case. But what about the absolute value of $t_{\rm DF}$? In fact, Ciotti (2010) showed that a significant overestimate of the DF time-scale can arise if approximating a multi-mass system with a single component only. In our case this check can be done by introducing the definition of the *Equivalent Classical System* (ECS):

- the *number* density in the ECS is equal to the *total* number density of the multi-mass case:
$$n_{\rm ECS}(r) = \sum_{i=1}^{N_{\rm pop}} n_i(r); \tag{2.9}$$
- the mass of the field particles in the ECS ($m_{\rm ECS}$) is equal to the *average* field mass of the multi-component case:
$$m_{\rm ECS} = \frac{1}{N} \sum_{i=1}^{N_{\rm pop}} m_i\, N_i \tag{2.10}$$
where N is the total number of stars in the multi-mass system;
- the velocity dispersion of the ECS is equal to the *equipartition* velocity of the multi-component case.

The last property is non relevant in our case, since we compute the function $\Xi(r)$ directly from the simulation outputs, as the fraction of all the stars slower than the test particle. In order to compare the DF time-scale obtained in the ECS approximation with the exact determination for the multi-mass case discussed in the previous section, we used eq. (2.4) by assuming $n(r) = n_{\rm ECS}(r)$, $m_t = 4\ m_1$ and

[1]The progressive increase of the central density, combined with an expansion of the outer layers are also responsible for the enlarged radial sampling (both toward the center and in the outskirts) for increasing evolutionary times, as a consequence of by the adopted binning procedure.

$m = m_{\rm ECS} \simeq 1.2\ m_1$. To compute $M(r)$ entering the definition of v_t, we counted the number of particles within the radius r and multiplied it by $m_{\rm ECS}$. The comparison between the DF time-scale in the multi-mass and in the ECS cases for $W_0 = 8$ is shown in fig. 2.5 (solid lines). As expected, no differences are found at $t = 0$, when mass-segregation has not played any role yet. This is due to the fact that the mass density is nearly the same in the two cases, because the three components have equal radial distributions and $m_{\rm ECS}$ well corresponds to the true mean mass at all radii. When mass-segregation takes place, a systematic underestimate of DF in the ECS case becomes apparent in the central regions, where $t_{\rm DF}$ can be almost a factor of 3 larger than in the true multi-mass system. This discrepancy is due to the systematic underestimate of the ECS local mass density with respect to the multi-mass one. In fact, as a consequence of mass segregation, the number density at small radii is mainly contributed by the heaviest stars, and since m_3 is significantly larger than $m_{\rm ECS}$, the ECS mass density in these regions is considerably smaller than the multi-mass one. A smaller density implies a lower efficiency of DF, thus bringing to larger values of $t_{\rm DF}$ in the ECS with respect to the multi-mass case. Beyond the half-mass radius, the ratio between the values of $t_{\rm DF}$ in the two cases becomes nearly flat around 1. This is because beyond the half mass radius no appreciable mass-segregation has taken place during the simulated time, and so the local average mass is nearly equal to $m_{\rm ECS}$ in that region, as in the initial conditions.

As a final test we modified the definition of ECS in requiring that the *mass density* in this approximation is equal to the true mass density of the multi-component system at any radius:

$$\rho_{\rm ECS}(r) = \rho(r) = \sum_{i=1}^{N_{\rm pop}} \rho_i(r). \tag{2.11}$$

As expected the difference between the two representations is considerably reduced and the underestimate of $t_{\rm DF}$ is about half that previously found (see the dashed lines in fig. 2.5). Therefore, we conclude that special attention should be paid to arguments based on specific requests about the value of $t_{\rm DF}$, as estimate based on the average properties of the GC can be off by a factor of 2 or 3, factors that are quite important for phenomena happening on time scales of the order of the Hubble time.

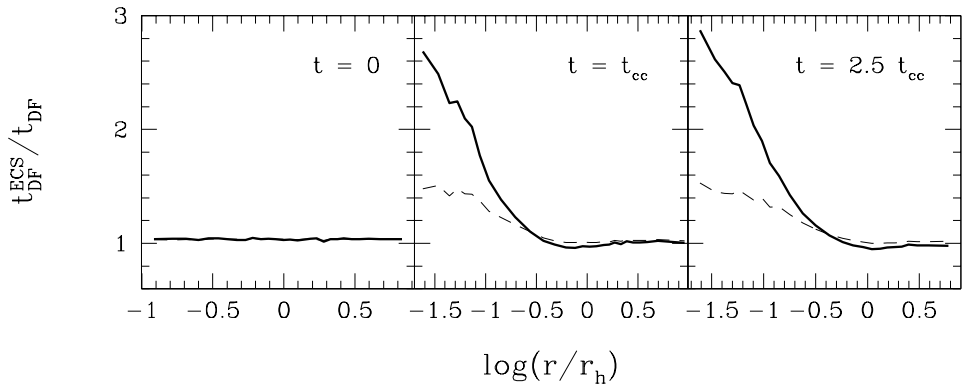

Figure 2.5: Ratio between the DF time-scale computed in the ECS approximation and for the multi-mass system, as a function of radius (in units of the total half-mass radius), for three evolutionary times (see labels) and for the model with initial conditions $W_0 = 8$. The thick solid lines show the results obtained under the assumption that the *number* density of the ECS system equals that of the multi-mass case: $n_{\rm ECS}(r) = n(r)$. The dashed lines refer to the approximation in which the *mass* density of the ECS system is equal to that of the multi-mass case: $\rho_{\rm ECS}(r) = \rho(r)$. The results are essentially the same $W_0 = 4$ and $W_0 = 6$. Notice how the number average estimate can be off by a factor up to 3 in the central regions, while a much better estimate is obtained by using the mass density average.

Chapter 3

Semi-analytical models and preliminary N-body simulations

3.1 Introduction

In chapter 2, we studied the evolution of the DF time scale in a dynamically evolving multi-mass GC, and we excluded the possibility that the bimodal shape of the BSS-nRD in Family-II GCs is due to a non-monotonic radial behaviour of this quantity. Now, the idea is to model all the ingredients contributing to BSS segregation, step by step; the aim is to isolate all the important effects, one by one, avoiding sudden complications to the model that could lead to an incomprensible superposition of all the various effects that take part in this process (tidal field, primordial binaries, binary evolution, large number of particles, impact of a BH subsystem, ect.). Hence, to properly address the problem, as a first step we need semi-analytical models coupled with preliminary N-body simulations. For this reason we started with a semi-analytical approach with some basic assumptions.

In Sect. 3.2 we present the assumptions of our the semi-analytical model, while the results of this approach are presented in Sect. 3.2.1. Preliminary N-body are presented in Sect. 3.3, followed by their results in Sections 3.3.1 and 3.3.2. Section 3.4 concerns our first simulation with a larger number of particles, the results of which are presented in Sect. 3.5.

3.2 The semi-analytical model

We consider an isolated cluster. The mass spectrum is modeled as sect. 2.3.2 of the previous chapter, considering only three species meant to represent low-MS stars, reference population stars (REF) and BSSs. The first component is the lightest one and primarily contirbutes to both the overall gravitational potential and DF.

The REF population represents intermediate-mass objects, corresponding to TO, RGB and or HB stars in real GCs. BSSs are the most massive component and their number counts are normalized to those of the REF stars, as it is routinely done in obsevational studies.

The system is subject to a static gravitational field ($\mathbf{g}$), due to MS stars only, which play the role of the *field stars*. These objects have the same mass m_f and are assumed to have a spherically symmetric spatial distribution and an isotropic velocity dispersion distribution. Their distribution function $f(r, v)$ is defined such that $f(r, v)d\mathbf{r}d\mathbf{v}$ is the number of these stars in the phase-space volume element $d\mathbf{r}d\mathbf{v}$ (with $r = |\mathbf{r}|$ and $v = |\mathbf{v}|$). Under these assumptions, $\mathbf{g}$ is constant with time. With this field, the DF deceleration on a *test* star with mass m_t moving in a background of field stars with masses m_f is determined by the Chandrasekhar (1943) formula

$$\mathbf{a}_{\rm DF} = -4\pi \ln \Lambda G^2 m_f (m_f + m_t)\psi(r, v)v^{-3}\mathbf{v},$$

where

$$\psi(r, v) = 4\pi \int_0^v f(r, u)u^2 du,$$

is the number density at radius r of field stars moving slower than the test star. We neglected the self-gravity acting on all of the mass components and any interaction between test stars. We assumed that the distribution function of test stars is described by a Plummer (1911) model. With this assumption, the gravitational field is

$$\mathbf{g}(\mathbf{r}) = -\frac{GM}{(r^2 + {r_0}^2)^{3/2}}\mathbf{r},$$

where M is the total mass of the field stars and r_0 is the characterstic length scale of the Plummer model. The DF deceleration acting on BSSs and REFs is completely determined once the values for m_f, m_t and r_0 are chosen. We recall from chapter 2, sect. 2.3.2, that we assigned to BSSs a mass of $3m_f$ and to the REF stars a mass of $2m_f$.

After this assumptions, we generated a set of initial conditions (positions and velocities) the two evolving components (BSSs and REFs) assuming the same total number of stars of each species as in Sect. 2.3.2: $N_{\rm BSS} = 300$ and $N_{\rm REF} = 1200$. They follow the same Plummer distribution function as the field stars; this choice is in agreement with the observations, considering that, for dynamically unevolved clusters (Family-I GCs), all the populations are observed to follow the same radial distribution.

Starting from these initial conditions, we time-integrated the orbit of each test star, under the total acceleration $\mathbf{a} = \mathbf{g} + \mathbf{a}_{\rm DF}$, using a second order leapfrog algorithm (e.g., Hockney & Eastwood, 1988) with a constant time step. At given times, a snapshot of the system was extracted and the projected number distribution of

the two heavier stellar species was derived in a series of concentric annuli around the cluster center, to build the radial distributions of the two populations.

3.2.1 Results of the semi-analytical model

We computed the double normalized ratio of BSSs with respect to the fraction of REF stars i.e.: $R_{\rm BSS}(r) \equiv (n_{\rm BSS}(r)/N_{BSS})/(n_{\rm REF}(r)/N_{\rm REF})$. Since the REF population is distributed as the cluster luminosity, this is consistent with the defintion provided in Chapter 1 and first introduced by Ferraro et al. (1993), where the fraction of BSSs is normalized to the fraction of sampled light. In Fig. 3.1 we plot $R_{\rm BSS}$ for four evolutionary times. The radius is normalized to the Plummer length scale r_0, while times are expressed in units of the half-mass relaxation time t_{rh}, i.e., the relaxation time computed at the half-mass radius (Binney & Tremaine, 2008) of the field stars. The initial flat distribution (upper panel in Fig. 3.1) is a consequence of our initial conditions, for which all the populations share the same distribution function, by construction. In less than one t_{rh}, however, the BSS radial distribution becomes rapidly bimodal (second panel from the top in Fig. 3.1); moreover, its minimum progressively moves outward with time (see the drift of the arrow from the second to the bottom panel of Fig. 3.1). At the end of the simulation, however, the shape of the BSS radial distribution becomes almost flat again, with the central peak disappearing.

Part of these results are in accordance, at least qualitatively, with the scenario depicted by Ferraro et al. (2012): they show that DF by itself can give rise to a bimodal BSS distribution. However, the central peak which forms very rapidly at the early stages of the evolution, does not last over time, in contrast with the observations. The reason of this dumping, is that DF acts on both REFs and BSSs indefinitely, causing almost all the test stars to fall in the innermost radial bin, giving a double-normalized ratio which is nearly 1 (namely, the innermost five bins in the bottom panel of Figure 3.1 contain $\sim 95\%$ of the total test stars).

To quantify the level of bimodality of the distribution, we defined the parameter b as the best-fit slope for $R_{\rm BSS}$ in the region of the rising branch, from the radius of the minimum r_{min} up to $r_{min} + 4\Delta r$ (with Δr being the minimum threshold to the width of each radial bin). Empirically, with a visual inspection of the snapshots, it turns out that bimodality in the double normalized-ratio can be well appreciated when $b \gtrsim 0.01$.

For those snapshots satisfying the "bimodality" condition ($b \gtrsim 0.01$), we plotted the time evolution of the minimum, which is shown in Fig. 3.2. Althought the fluctuations are quite large, the outward migration of the minimum is evident from the figure, in accordance with what a visual inspection of Fig. 3.1 suggested, supporting, at least qualitatively, the dynamical-clock scenario.

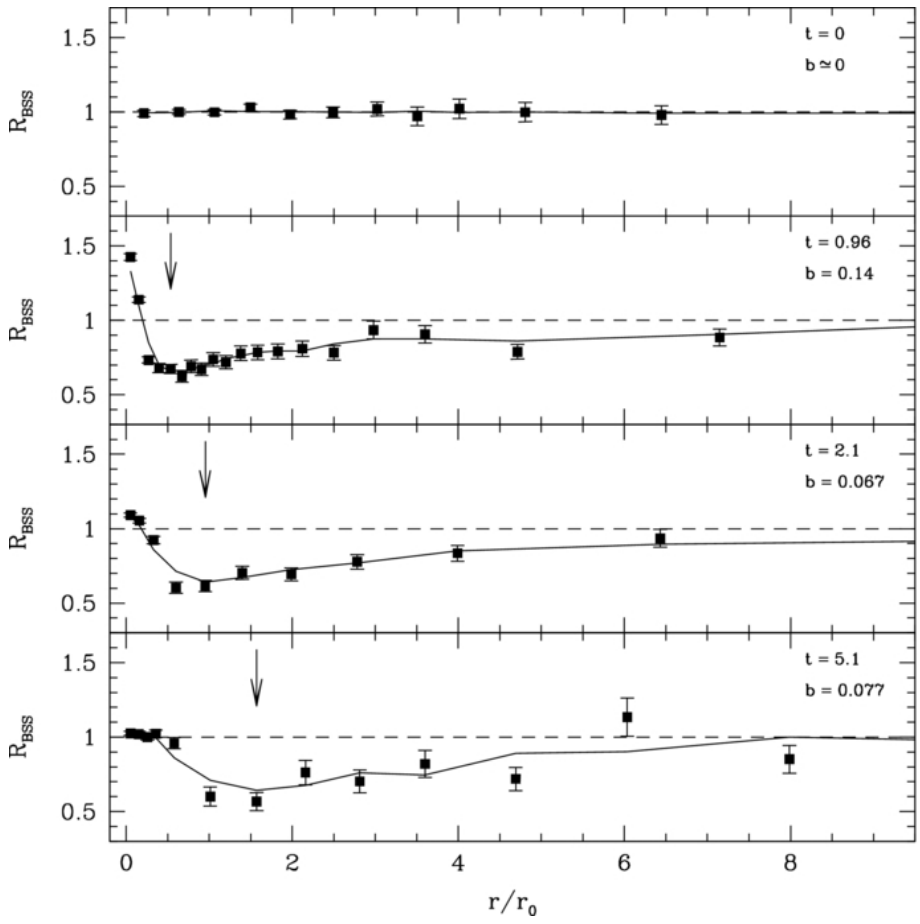

Figure 3.1: Double-normalized ratio ($R_{\rm BSS}$) between the projected number of BSSs and that of REFs, in various radial bins around the cluster center and at four different evolutionary times (see labels), from the semianalytical model. Time is normalized to the half-mass relaxation time t_{rh}. The solid curve in each panel is the running average of the $R_{\rm BSS}$ radial behavior. Also labeled is the slope (b) of the rising branch beyond the dip (see text). The number of radial bins is variable due to the employed adaptive binning method. From Miocchi et al. (2015).

3.3 Preliminary N-body simulations

As a step forward to adopt a more realistic approach, we investigated the problem by means of collisional N-body simulations. Hence, we studied the behaviour of $R_{\rm BSS}$ and the evolution of r_{min} in the same set of simulations already introduced in chapter 2. We will directly present the results of this part of the work, since the set-up of the simulations is already known by the reader. The only difference is in the association between GC stars and the simulated particles: the $N_1 = 8500$ particles of mass m_1 represent MS stars with average mass of $\sim 0.4 M_\odot$, the $N_2 = 1200$ particles with mass $m_2 = 2m_1$ are assumed to be the REF population (hence, MS turnoff, RGB, or HB stars), while the remaining $N_3 = 300$ particles with mass $m_3 = 3m_1$ are now intended to be BSSs.

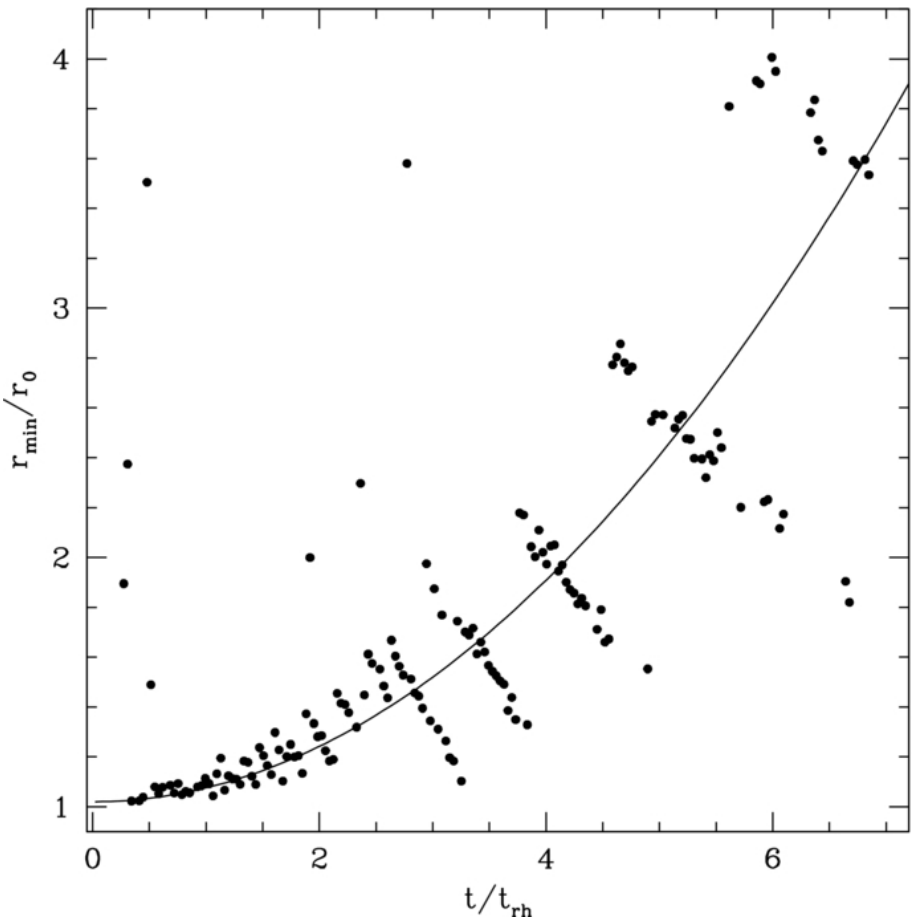

Figure 3.2: Time evolution of the position of the absolute minimum, r_{min} (dots), normalized to the Plummer characteristic scale radius, for all the snapshots in which $R_{\rm BSS}(r)$ has an appreciable bimodality ($b \geq 0.01$; see the text). The solid line is a fitting $\sim t^2$ law.From Miocchi et al. (2015)

3.3.1 Results

We first start showing the overall evolution of the system. In Figures 3.3–3.5, the evolution of three representative Lagrangian radii is shown for the three mass components and for each of the initial W_0 values. We note that the heavier components (BSSs and REFs) in the internal regions contract (see R_{10} in the figures), following the core contraction; this process injects kinetic energy to the halo (because of energy exchanges during close encounters between halo stars and core stars) which reacts with a monotonic expansion (see the behaviour of R_{99} in the figures). This is also the cause for the lack of contraction of the 10% Lagrangian radius of the MS stars. Overall, the dynamical time-scales are shorter for the heavier components. All these results well agree with what expected from the well known collisional relaxation processes in systems with a mass spectrum (e.g., Heggie & Hut, 2003; Gürkan, Freitag & Rasio, 2004; Khalisi, Amaro-Seoane & Spurzem, 2007). With dotted line, we also show the time evolution of the core radius of the reference population, de-

fined as the radius at which the surface density profile (rising from the King model that better fits the central regions) reaches the half of its central value. This choice is made to be as close as possible to the core radius adopted in observational works (e.g., Ferraro et al., 2012), and it allows to meaningfully compare our results with the observations. Incidentally, we report that, at least within the CC time, the REF core radius is well described by the 10% Lagrangian radius of the same population. The time at which r_c (as well R_{10}) changes the slope from negative to positve is the time that we get as representative of the CC time (which occurs at $t \simeq 3.7, 2.5$ and $0.7\ t_{rh0}$ for $W_0 = 4, 6$ and 8 simulations, respectively).

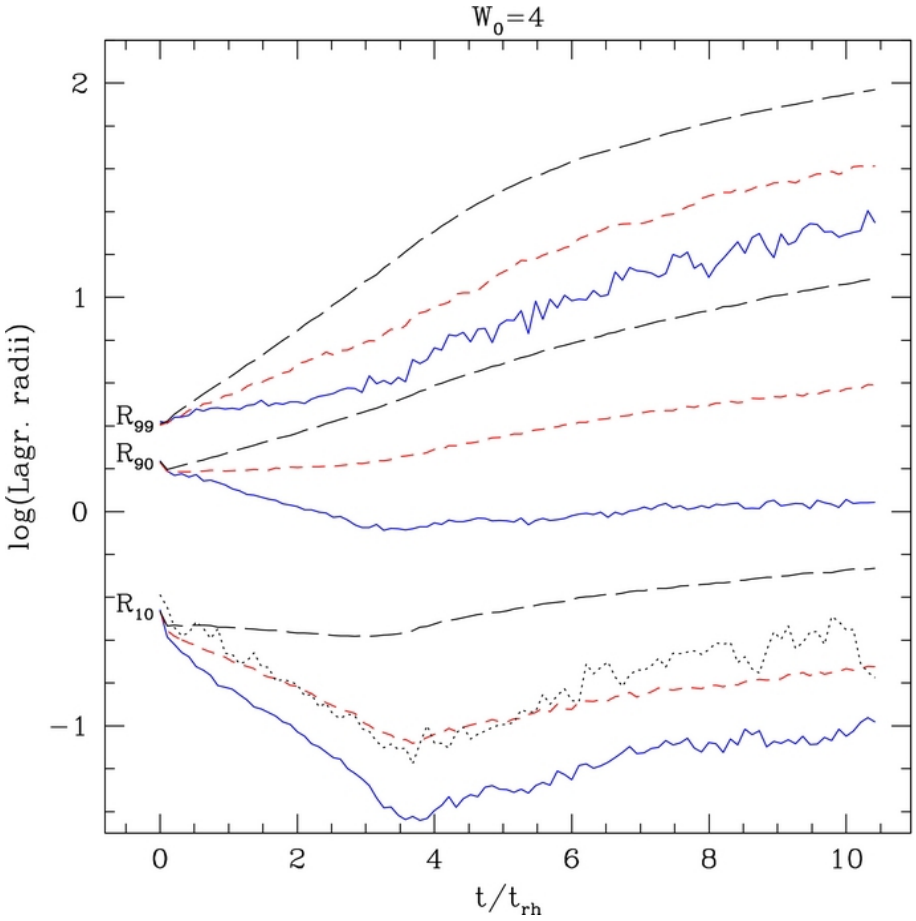

Figure 3.3: Time evolution of the Lagrangian radii of the three mass components in simulations with $W_0 = 4$. From top to bottom: R_{99}, R_{90}, R_{10}, wich are the radii containing the 99, 90 and 10% of particles, respectively. Blue line: BSSs; red-dashed line: REFs; black-dashed line: MSs; black-dotted line: core radius $r_c(t)$ of REF stars. From Miocchi et al. (2015).

3.3.2 Bimodality in $R_{\rm BSS}$

Now we focus on the behaviour of the BSS double-normalized ratio in our simulations. In Figure 3.6, $R_{\rm BSS}$ is shown at four different evolutionary times for the

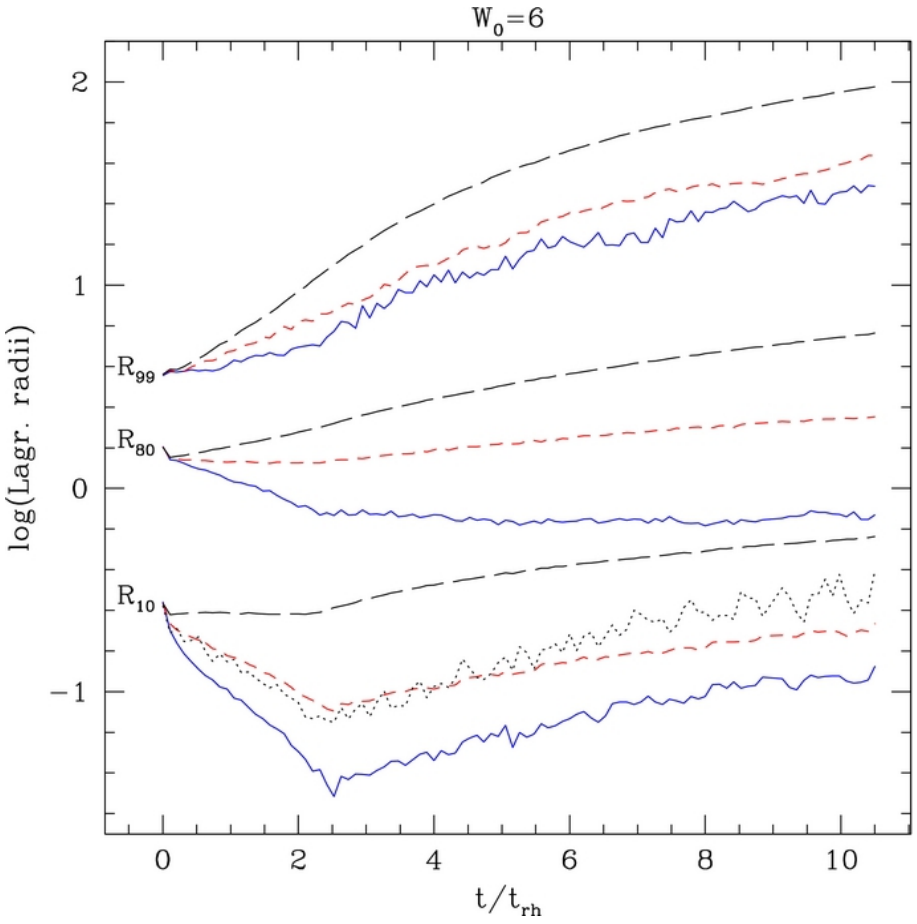

Figure 3.4: The same as Fig. 3.3 for the simulations with $W_0 = 6$. From Miocchi et al. (2015).

simulations with $W_0 = 6$. Obviously, the initial radial profile of $R_{\rm BSS}$ is flat around 1, by construction (upper pannel of the figure); then, a bimodal shape develops, with the central peak growing as the evolution proceeds and the BSSs segregate toward the cluster centre; at odds with the semi-analytical model, this feature is stable and long lasting. Meanwhile, a dip forms in the intermediate regions, with its width increasing with time. Moreover, the radius of the minimum (r_{min}) drifts outward with the dynamical evolution of the system, reaching very external regions at the late stages of the simulation and leading to a monotonic distribution at the end of the run (see the bottom panel of Fig. 3.6), in agreement with what observed in Family III-GCs (Ferraro et al., 2012).

Similar general comments also apply to the case of the simulations starting with $W_0 = 8$, for which the behaviour of the double-normalized ratio is shown in Figure 3.7. In this case, the bimodality is even more apparent, as well as the increasing depth of the minimum.

All these features are in good qualitative agreement with the observations (e.g., Ferraro et al., 2003b, 2012). However, the progressive decrease of BSSs in the

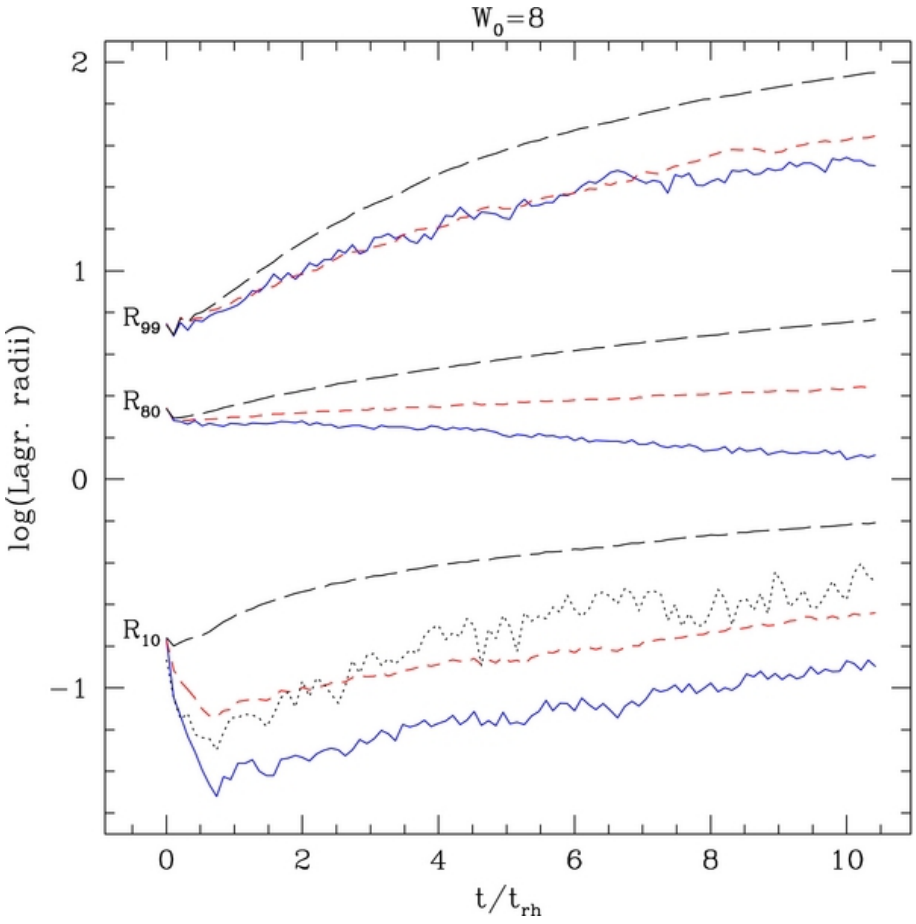

Figure 3.5: The same as Fig. 3.3 for the simulations with $W_0 = 8$. From Miocchi et al. (2015).

external regions makes the detection of the minimum (i.e., of the bimodality) quite difficult in some snapshots.

In the simulations with $W_0 = 4$ no significant bimodality develops at any time: $R_{\rm BSS}$ is always a monotonic decreasing function of the radius showing just a central peak. This behaviour (as well as the fact that bimodality is better apreciated in the $W_0 = 8$ than in the $W_0 = 6$ case) can be well understood by considering that the DF time-scale profile mainly depends on the density profile (see chapter 2 and Alessandrini et al., 2014). Thus, since low-concentrated systems have more extended cores (where the density profile is essentially flat) also the region in which the DF time-scale is constant is larger than in high concentration clusters (which, instead, have small cores). This causes DF to act more rapidly and less gradually (in terms of both time-scales and size of the interested region) in clusters with low-concentration: as a consequence, DF tracers (as the $R_{\rm BSS}$ bimodality and the outward migration of r_{min}) are more difficult to be detected in low-concentration systems. However, $R_{\rm BSS}$ is observed to be bimodal also in low-W_0 GCs, making the lacking of bimodality in the $W_0 = 4$ simulations worth to be investigated.

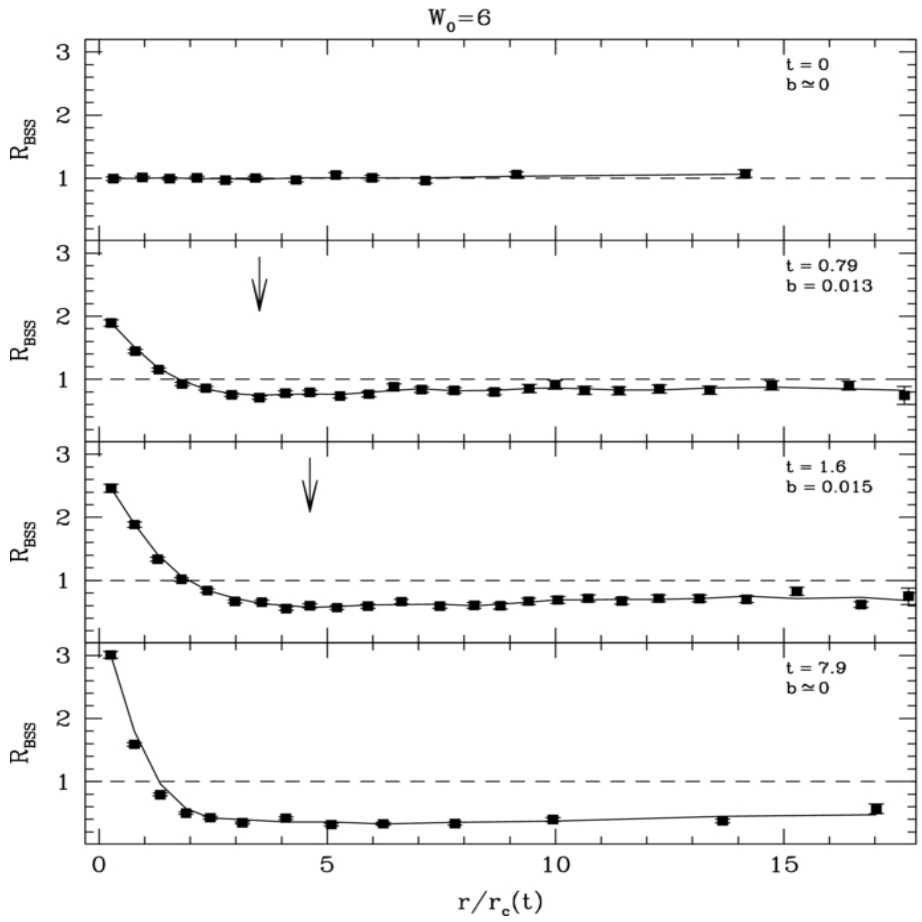

Figure 3.6: Profile of the double-normalized ratio (dots) for the $W_0 = 8$ simulations, at four different evolutionary times (see labels). Dashed line: initial value of $R_{\rm BSS}$ ($\simeq 1$, which means no mass segregation); solid curve: running average of $R_{\rm BSS}$. The arrow marks the radius of the absolute minimum, r_{min}. The level of bimodality (b) is also reported (see labels). From Miocchi et al. (2015).

3.4 The first $N = 10^5$ simulation

As a further test, we built a simulation by increasing the number of particles from $N = 10^4$ to $N = 10^5$. This choice allows us to better describe the collisionality of the system, which depends on the number of particles. In this case, due to the high computational costs, we ran only one simulation, with $W_0 = 8$. This choice arises from the verification that DF effects are more gradual and visible for high concentration cases (see the discussion in Sect. 3.3.2).

Also for this simulation, the mass spectrum is modeled with three different mass bins that contain low-MS stars, REFs and BSSs, with numbers $N_{\rm MS} = 96700$, $N_{\rm REF} = 3000$ and $N_{\rm BSS} = 300$.

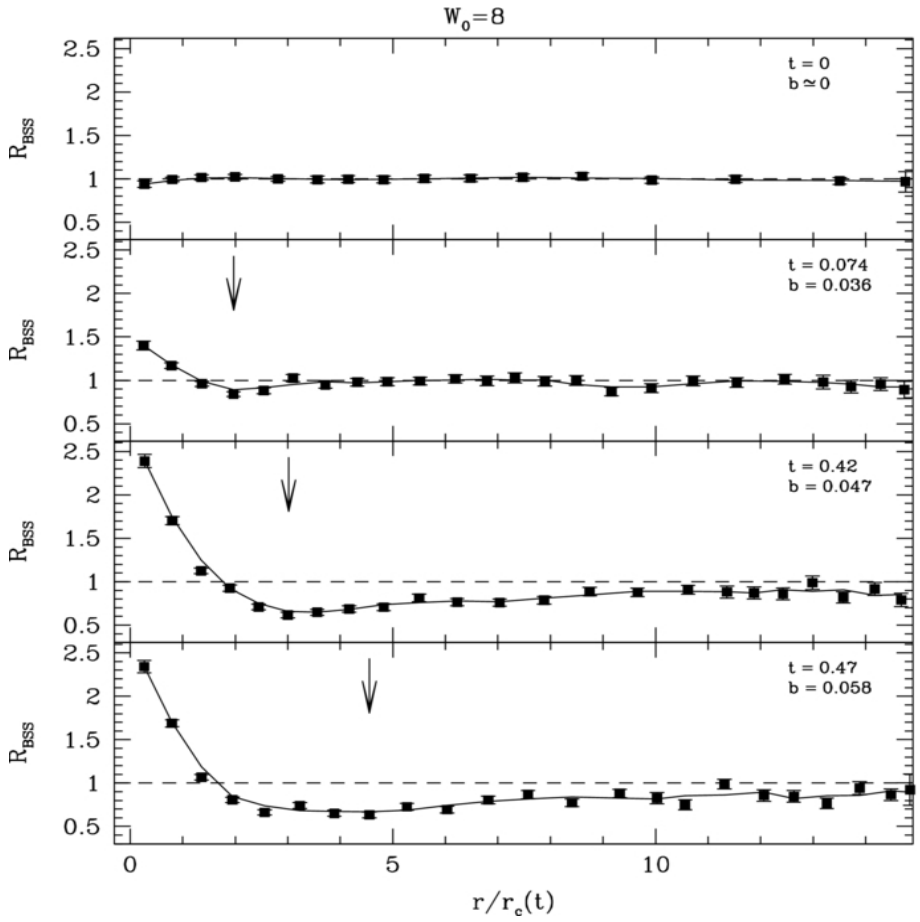

Figure 3.7: Same as Fig. 3.6 for the simulations with $W_0 = 8$. From Miocchi et al. (2015).

3.5 Results of the 10^5 model

As in Figures 3.3–3.5, in Figure 3.8 we show the time evolution of three Lagrangian radii for the three mass components, in the case with $N = 10^5$ stars. All the consideration made in Section 3.3.1 for the overall evolution of $N = 10^4$ simulations, still apply to the case $N = 10^5$. A notable feature is that in this simulation the CC time increases by a factor of 2.3, occurring at $t \simeq 1.6 t_{rh}$ (the CC time is $t \simeq 0.7\ t_{rh}$ in the 10^4 particle case with the same W_0). This comparison clearly shows that the 10^4 particle simulations do not provide reliable characteristic timescales of the various dynamical processes. However, they are useful for qualitative conclusions.

The evolution of the BSS double-normalized ratio is shown in Figure 3.9: with respect to the $N = 10^4$ simulations, the outward migration of r_{min}, as well as the formation and growing of the central peak are more evident in this more realistic case, prompting us to further improve the realism of the simulations in order to properly model the BSS segregation process in GCs, and meaningfully compare numerical results with observational data.

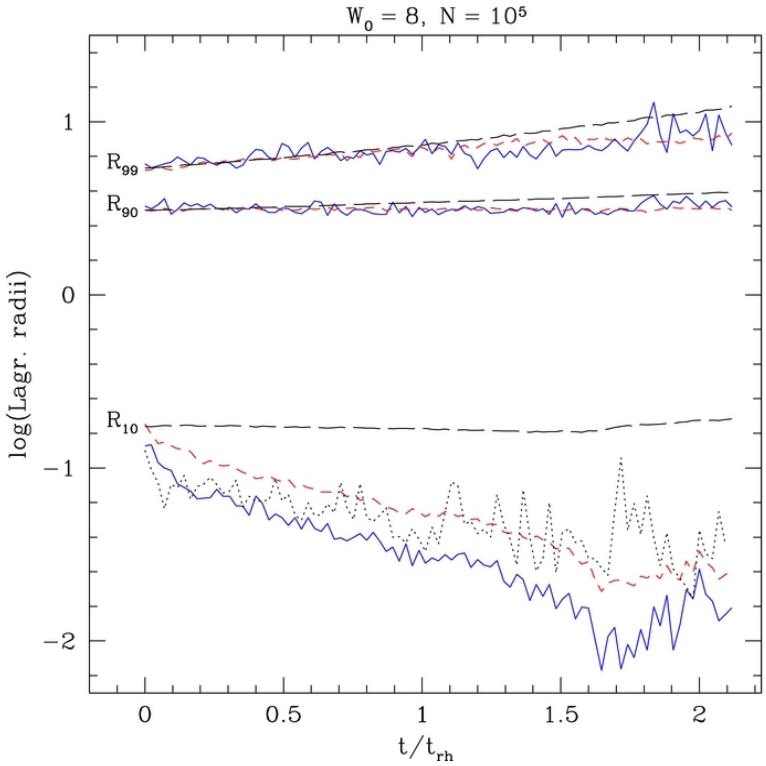

Figure 3.8: Same as Fig. 3.3 for the case with $N = 10^5$ particles (and $W_0 = 8$). From Miocchi et al. (2015).

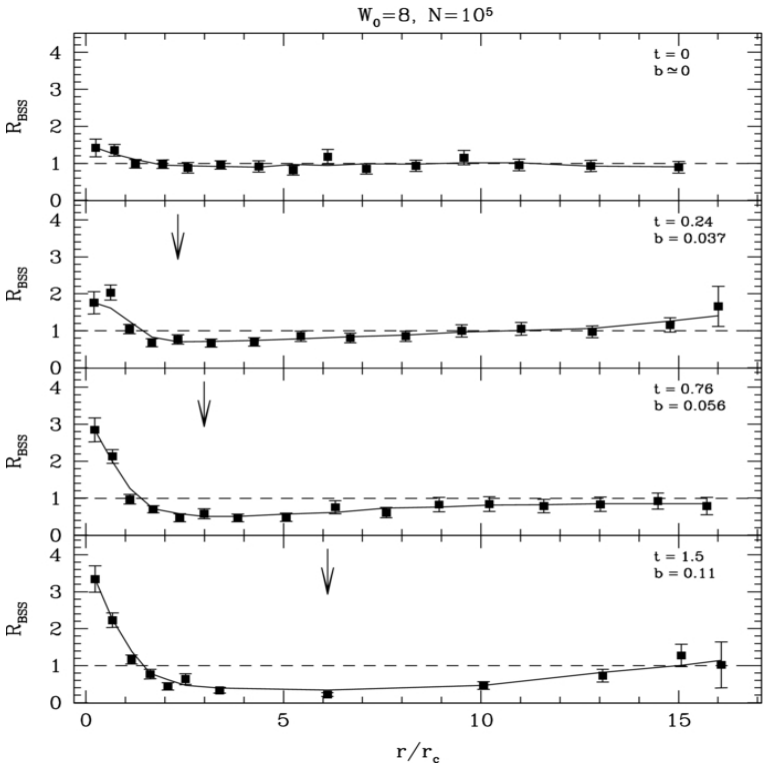

Figure 3.9: Same as Fig. 3.6 for the case with 10^5 particles. From Miocchi et al. (2015).

Chapter 4

More realistic simulations: the impact of dark remnants

4.1 Introduction

In chapter 3 we made a first attempt to model the evolution of the BSS radial distribution under the action of DF. In Miocchi et al. (2015), we performed simulations with 10^4 particles, obtaining qualitative good agreement with the observations. However, the results are affected by some noisy behaviour and, in particular, we faced the problem of accurately determining the value of r_{min}, which suffers from low number statistics, partially due to the lacking of realism of the initial assumptions. We can resume some of the weak points affecting the simulations used in chapter 3 as follows:

- Small number of particles ($N = 10^4$);
- Unrealistic mass spectrum (only three discrete mass bins);
- Predominant dynamical role of BSSs (they are the most massive objects in the system, driving the CC and the overall evolution of the cluster).

However, GCs are million-body systems containing stars with different masses distributed with a mass function, which represents a continuous distribution of mass instead of a discrete one. Moreover, from the stellar evolution theory, we know that all stars more massive than the current MS turnoff mass in a GC already exhausted their thermonuclear burning processes and became either black holes (BHs), or neutron stars (NSs), or white dwarfs (WDs), depending on the initial mass of their progenitors. Observationally, the presence of WDs and NSs is largely confirmed (see, e.g., Cackett et al., 2006; Kirsten et al., 2014; Maccarone et al., 2016), and

very recent results showed that also some stellar-mass BHs is still orbiting the potential well of a few GCs (e.g., Strader et al., 2012; Chomiuk et al., 2013; Miller-Jones et al., 2015; Peuten et al., 2016). However, at least a fraction of these objects is predicted to be ejected from the system either at birth (due to supernova explosion kicks) or later on, through dynamical interactions. Indeed, the exact number of these objects, especially of NSs and BHs (that we will refer to as dark remnants, DRs), in present-day GCs is poorly constrained and, during the last 30 years, many authors have addressed the problem of how many NSs (e.g. Hut, Murphy & Verbunt, 1991; Drukier, 1996; Davies & Hansen, 1998; Pfahl, Rappaport & Podsiadlowski, 2002; Podsiadlowski, Pfahl & Rappaport, 2005) and BHs (e.g., Sigurdsson & Hernquist, 1993; O'Leary et al., 2006; Moody & Sigurdsson, 2009; Repetto, Davies & Sigurdsson, 2012; Morscher et al., 2013; Sippel & Hurley, 2013) are retained during the evolution of the cluster, in what is called the DR retention problem. In spite of the uncertainties on their number, DRs are known to play a fundamental role in the dynamical evolution of GCs; their influence is due to their high-masses, which cause their rapid segregation toward the cluster centre and the formation of a heavy subsystem that dynamically interacts with the other "normal" stars, acting as a source of dynamical-heating from the core to the halo stars (e.g., Breen & Heggie, 2013a,b; Morscher et al., 2015). Hence, a model that aims at properly describing the dynamical evolution of GCs requires the presence of a population of DRs among its ingredients.

For all these reasons, as a further step toward more realistic models, we decided to run a set of simulations that, with respect to those in Miocchi et al. (2015), include (*i*) a significantly larger number ($N \simeq 10^5$) of particles, (*ii*) a much finer mass-spectrum obtained from the evolution of a Kroupa (2001) Initial Mass Function (IMF), and (*iii*) a population of DRs. Since the initial conditions are subject to the above mentioned retention problem, we performed simulations with different fractions of NSs and BHs. Moreover, instead of following the evolution of the shape of the BSS distribution, and try to locate the position of the minimum, here we define a new parameter able to quantify the level of sedimentation of BSSs toward the cluster center with no need of binning the data.

In Section 4.2 we present our set of N-body models, describing the initial conditions of the simulations; in Sections 4.3.1–4.3.2 we discuss the time evolution of the Lagrangian radii and the cumulative radial distributions of BSSs and reference stars. In Sections 4.3.3 we define a new mass segregation indicator and discuss its time dependence.

4.2 N-body models

The simulations exploit the Graphic Processing Unit (GPU) version of the direct N-body code `NBODY6` (Nitadori & Aarseth, 2012) on the `BIGRED2` supercomputer at Indiana University, Bloomington. We performed ten different runs in order to explore both the effect of various percentages of DRs, and the effect of different cluster concentrations, on GC dynamical evolution.

The initial conditions have been built as follows. Starting from 99700 stars belonging to a Kroupa (2001) IMF, in the mass interval $m = [0.1, 100]M_{\odot}$ and assuming a metallicity $Z = 0.001$, we evolved the system for 12 Gyr, by means of the stellar evolution recipes implemented in the SSE version of the software `McLuster` (Hurley, Pols & Tout, 2000; Hurley, Tout & Pols, 2002; Küpper et al., 2011). This procedure generated a population of WDs and DRs descending from the evolution of stars with initial masses $m > 0.8M_{\odot}$. In particular, NSs have masses peaked at $1.4M_{\odot}$, with a tail up to $2.5M_{\odot}$, while BH masses range between $2.5M_{\odot}$ and $\sim 25M_{\odot}$. To all the runs we also added 300 BSSs, modeled as single particles with a mass of $1.2M_{\odot}$. The number of BSSs in our runs, although being overabundant with respect to what observed in real GCs, guarantees enough statistics to limit stochastic noise in the results. We assume the particles follow a King (1966) model distribution with no primordial mass segregation. In order to explore the effect of different concentrations, we have chosen two different values of the King central dimensionless potential: $W_0 = 5$ and $W_0 = 8$.

With the aim of exploring how cluster dynamics depends on the presence and content of heavy objects, and to isolate the effect of BHs from that of NSs, for each of the adopted W_0 values we ran five simulations by varying, in the initial conditions, the percentage of DRs retained within the system: (i) in simulations S_0^{W0} (with $W_0 = 5, 8$) no DRs have been retained (hence, BSSs are the most massive objects in the cluster); (ii) in runs S_{10}^{W0} and S_{30}^{W0} we assumed that 10% and 30%, respectively, of NSs have been retained, while all BHs have been ejected; (iii) in simulations $S_{10\bullet}^{W0}$ and $S_{30\bullet}^{W0}$ we assumed that 10% and 30%, respectively, of NSs and BHs have been retained. The number of NSs, BHs, and BSSs in the initial conditions of each run are summarized in Table 4.1.

4.3 Results

4.3.1 Evolution of the Lagrangian Radii

We start the presentation of our results with a brief description of the evolution of the structural properties of our simulated clusters, and the effects of the presence of DRs. Figures 4.2 and 4.3 show the evolution of the 5%, 10% and 50% number

Run	W_0	$f_{\rm DR}$ %	$N_{\rm NS0}$	$N_{\rm BH0}$	$N_{\rm BSS0}$	$N_{\rm TOT}$	$t_{\rm rh0}$
S^5_0	5	0	0	0	300	10^5	1330.5
S^5_{10}	5	10	72	0	300	99161	1325.4
S^5_{30}	5	30	206	0	300	99295	1326.9
$S^5_{10\bullet}$	5	10	72	19	300	99180	1325.6
$S^5_{30\bullet}$	5	30	206	67	300	99362	1328.8
S^8_0	8	0	0	0	300	10^5	1471.7
S^8_{10}	8	10	71	0	300	99183	1465.3
S^8_{30}	8	30	200	0	300	99313	1466.9
$S^8_{10\bullet}$	8	10	71	17	300	99202	1470.6
$S^8_{30\bullet}$	8	30	200	65	300	99379	1467.8

Table 4.1: Initial conditions of the N-body simulations. For each run, the table lists the adopted name (column 1), the intial value of the King dimensionless potential W_0 (column 2), the initial retention fraction of DRs (column 3), the total number of NSs, BHs, BSSs and particles of any mass at $t = 0$ (columns 4–7), the initial half-mass relaxation time expressed in N-body units (column 8). From Alessandrini et al. (2016).

Lagrangian radii of particles belonging to different populations in the simulations with no DRs and in those also including BHs, for $W_0 = 5$ and $W_0 = 8$, respectively. In particular, we compare the evolution of the Lagrangian radii of BSSs (i.e., all the particles with mass $m = 1.2\ M_\odot$; blue lines), of what we call *reference* population (REF), corresponding to all the particles with masses between 0.75 and 0.84 $M_\odot$ (red lines), and of the overall system, including all particles irrespective of their masses (grey lines). Moreover, for the runs with BHs, we also show in black the evolution of the DR population ($m > 1.4\ M_\odot$). The figures clearly show that the cluster dynamical evolution is highly affected by the presence and amount of DRs, and also depends on the initial concentration of the system. Quite interestingly, this is true not only in the innermost cluster regions (as sampled by the 5% and 10% Lagrangian radii), but the effects also extend much outward, with large differences even at radial distances including 50% of the populations.

The analysis of the results obtained for $W_0 = 5$ (Fig. 4.2) shows that if no DRs are present (left-hand column) BSSs drive the cluster toward CC. This is indeed expected (see also Miocchi et al., 2015), since in that case, BSSs are the most massive objects within the system. The time evolution of the Lagrangian radii in the cases where only NSs are retained (namely, simulations S^5_{10} and S^5_{30}) is very similar to that with no DRs (thus, we provide no explicit figures for these runs), since the large majority of NSs has masses comparable to that of BSSs. Hence, the main effect of including a DR population made of NSs only is that the collapse is driven by these objects and BSSs segregate just at a slightly slower rate than in the case with no DRs at all. In the $S^5_{10\bullet}$ and even more in the $S^5_{30\bullet}$ simulations, instead, DRs undergo

a rapid decoupling from the other populations, forming a subsystem that quickly sinks toward the centre (see the black curves in the central and the right columns of Fig. 4.2). Clearly this behaviour is due to the subsystem of BHs, which have masses significantly larger than BSSs and NSs. Analogous results have been found and discussed also by Sigurdsson & Hernquist (1993) and Kulkarni, Hut & McMillan (1993), and again very recently by Banerjee, Baumgardt & Kroupa (2010) and Breen & Heggie (2013b). Interestingly, the effect of BHs on the time evolution of the BSS and REF Lagrangian radii is negligible if a retention fraction of only 10% is assumed. In fact, their value in the $S^5_{10\bullet}$ run is almost the same, at any fixed value of time $t/t_{\rm rh0}$, as in the S^5_0 (and the S^5_{10}) case. In the $S^5_{10\bullet}$ simulation, after the initial phase of rapid DR decoupling, the inner Lagrangian radii of these heavy objects stay approximately constant up to $\sim 2.5\ t_{\rm rh0}$, then decrease steadily in time, closely followed by the Lagrangian radii of BSSs, which therefore start to participate in driving the overall cluster evolution, similarly to what happens in the S^5_0 run. Instead, for $f_{\rm DR} = 30\%$ the effect played by BHs is much stronger. After the initial decoupling from the rest of the system, DRs evolve at almost constant Lagrangian radii for approximately 6 initial relaxation times, while the other stellar components migrate much more gently inward: the Lagrangian radii of all populations are systematically larger, at the same evolutionary time, with respect to what observed in the $S^5_{10\bullet}$ case, and the difference between the Lagrangian radii of the BSS and the REF populations is smaller. The Lagrangian radii of BSSs start to approach those of DRs at $\sim 6\ t_{\rm rh0}$, while the same happens much earlier in the $S^5_{10\bullet}$ run. The overall system reacts with a continuos expansion of r_{50} (grey line in the bottom right panel). The presence and the amount of BHs in the system has a strong impact on the rate at which the dynamical evolution of BSSs and REFs proceeds: in particular, the evolution of the level of mass segregation of the BSS population is increasingly inhibited and delayed as the adopted DR retention fraction increases. In fact, while the time of CC of the visible component is $\sim 4.4\ t_{\rm rh0}$ if no DRs or only NSs are present, in the simulations including also BHs, it increases to ~ 5.2 for a 10% DR retention fraction, and further to ~ 7.5 for $f_{\rm DR} = 30\%$. These behaviours can be explained as an effect of dynamical heating due to the population of BHs, which inhibits mass segregation. It is interesting to note that the inibhition of the mass segregation, due to the heating from a BH subsystem, resembles what Baumgardt, Makino & Ebisuzaki (2004), Trenti et al. (2007) and Gill et al. (2008) have found in the presence of an intermediate-mass black hole (IMBH). A recent study by Peuten et al. (2016) has also shown that the lack of segregation observed in NGC 6101 might be due to a population of BHs, a result consistent with our findings.

Similar general comments as above also apply to the case of a much more concentrated system ($W_0 = 8$, in place of $W_0 = 5$), where the impact of DRs including a population of BHs is even more apparent (see Fig. 4.3). Overall the time evolution

is much faster than in the $W_0 = 5$ case, indicating that increasing the cluster concentration accelerates the dynamical evolution of the system. If DRs are absent, the inner Lagrangian radii (r_5 and r_{10}) of both BSSs and REF stars rapidly decrease in time until the CC (the rapid fluctuation in r_5 and r_{10} are simply a consequence of the ejection of BSS binaries), while r_{50} of the REF population remains almost constant during the entire evolution. If NSs and BHs are included (central and right-hand columns) all populations segregate much more slowly and the difference between the BSS and the REF Lagrangian radii is smaller at any fixed evolutionary times. In the $S^8_{30\bullet}$ run, DRs rapidly decouple from the rest of the system, then their inner Lagrangian radii expand significantly and start to re-contract only after $\sim 4\ t_{\rm rh0}$, closely followed by BSSs.

Hence, according to what expected, massive objects (especially stellar-mass BHs) are found to play a fundamental role in the cluster dynamics, driving the CC of visible stars and determining its timescale.

4.3.2 Cumulative radial distributions

The time evolution of the Lagrangian radii discussed in the previous section provides precious information about the processes of segregation and expansion of various stellar populations. Although our simulations are still idealized and not meant to be directly compared to observational data, it is important to identify and follow the evolution of mass segregation indicators that can be more easily adopted in observational studies of the segregation of BSS and REF populations. Many previous studies have shown that different GCs are characterized by different cumulative radial distributions, corresponding to different levels of BSS segregation in the central regions (e.g., Ferraro et al., 2004). Here we therefore study how the cumulative radial distributions of BSSs and REFs depend on the simulated cluster properties. In order to highlight the inner distance scale, where the effect of DF is the most evident, we choose to express the radial distance from the cluster centre in logarithmic units. Since in all simulations we assume no initial mass segregation (see Sect. 4.2), at $t = 0$ all populations are perfectly mixed and the BSS and the REF distributions are superimposed. However, as time increases, BSSs migrate toward the cluster centre more rapidly than the REF population (see Figs. 4.2 and 4.3) and the two corresponding cumulative radial distributions start to separate from each other.

For illustrative purposes, Figure 4.4 shows the cumulative radial distributions of BSSs and REFs (blue and red lines, respectively) for the $S^8_{30\bullet}$ run, at four different evolutionary times (normalized to the initial half-mass relaxation time of the run; see labels in the figure). For the sake of comparison, the radial distance is expressed in units of the half-mass radius of the REF population at the considered time. A notable feature in the figure is that the separation between the blue and the red

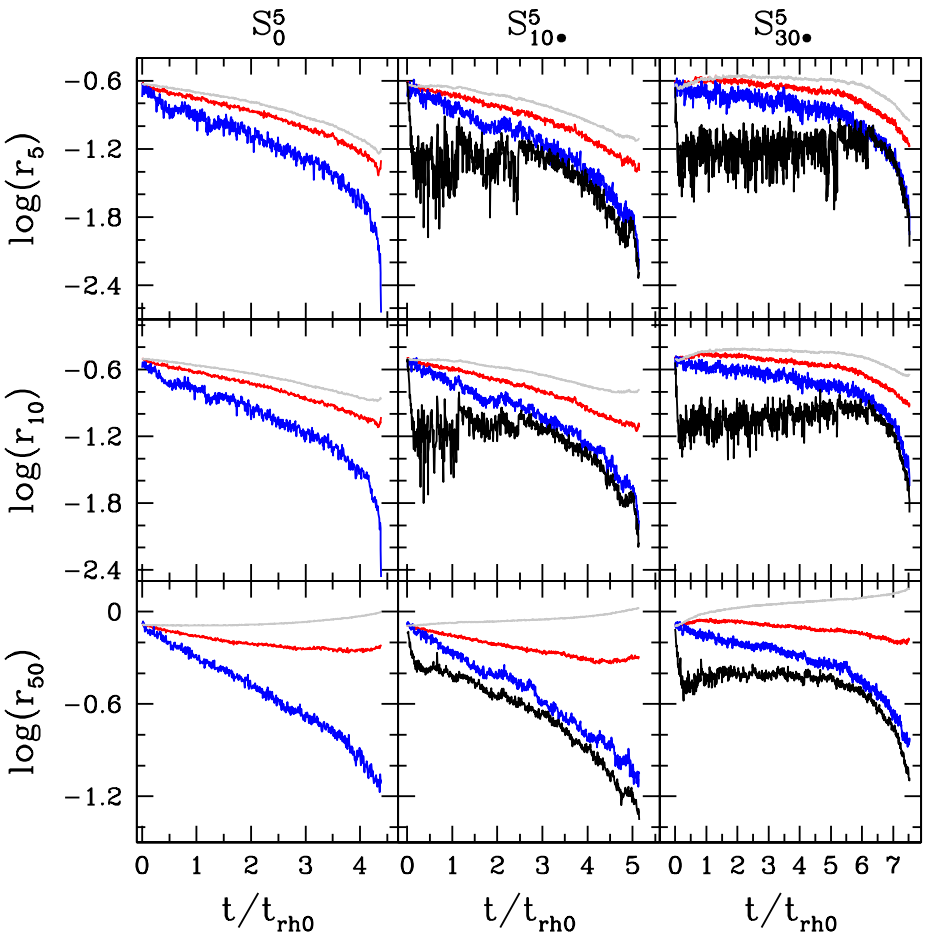

Figure 4.2: Evolution of the Lagrangian radii containing 5%, 10% and 50% (top, central and bottom panels, respectively) of the relative number of DRs (black), BSSs (blue), REF stars (red), and particles of any mass (grey), for the three runs with $W_0 = 5$ that include BHs. Time is normalized to the initial half-mass relaxation time $t_{\rm rh0}$ of each run (see Table4.1). From Alessandrini et al. (2016).

lines increases with time, with the BSS population always being more centrally segregated (i.e., with a steeper cumulative distribution) than the REF stars. This is due to DF that preferentially affects the heavier component (BSSs, with respect to REFs), making these objects more rapidly migrate toward the cluster centre.

Figure 4.5 compares the cumulative radial distributions obtained for the four models including BHs ($S^5_{10\bullet}$, $S^5_{30\bullet}$, $S^8_{10\bullet}$ and $S^8_{30\bullet}$) at a fixed evolutionary time, $t = 2.9\ t_{\rm rh0}$ (when the $S^8_{10\bullet}$ simulation stops). In line with what discussed in the previous sections, we find that BSSs are more centrally segregated for the lowest DR retention fraction (at fixed value of W_0) and for the largest cluster concentration (at fixed DR retention fraction). In particular, the accelerating effect on mass segregation due to a larger cluster concentration is clearly dominant in the case of a small population of DRs (10% retention fraction), while it is almost cancelled or even overcome if

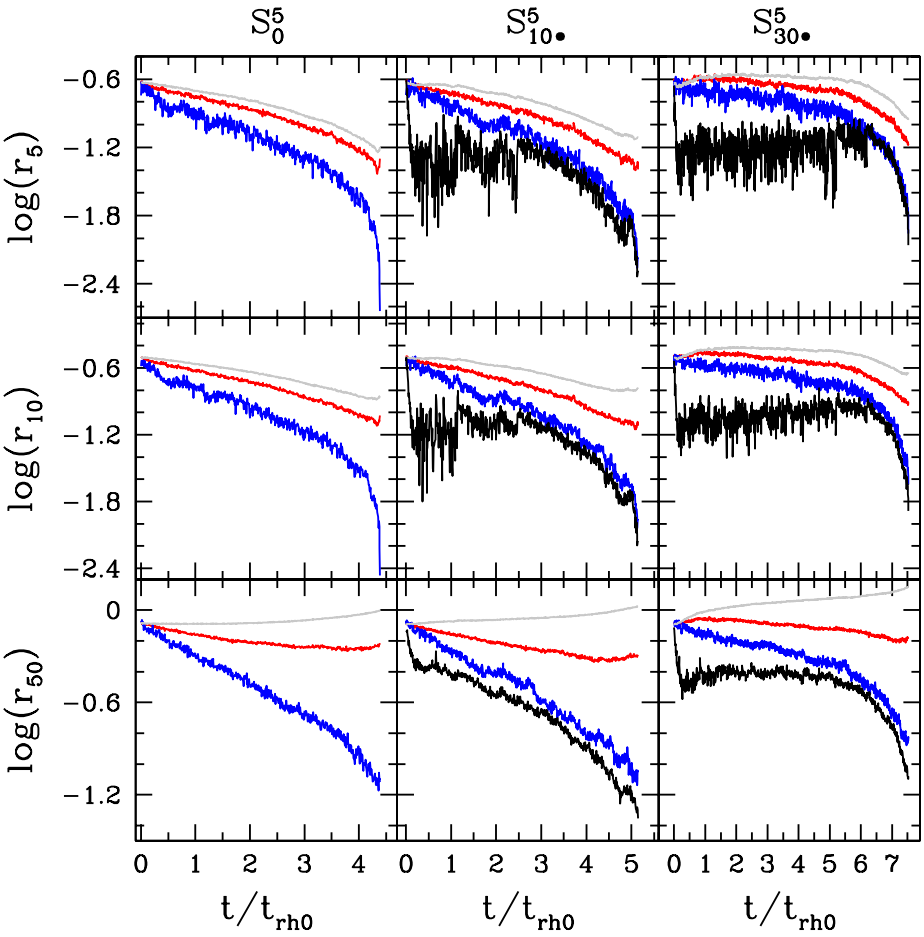

Figure 4.3: Same as Figure 4.2 for the runs with $W_0 = 8$ that include BHs. From Alessandrini et al. (2016).

DRs become sufficiently numerous. In fact, for a fixed 30% retention fraction the cumulative radial distributions in the $W_0 = 5$ and $W_0 = 8$ cases are quite alike, with the latter becoming different from zero at only slightly lower radii than in the $W_0 = 5$ case (compare panels labeled with $S^5_{30\bullet}$ and $S^8_{30\bullet}$ in Fig. 4.5). Such an effect is even more apparent from the comparison of the $S^5_{10\bullet}$ and $S^8_{30\bullet}$ radial distributions: in spite of a smaller concentration (and thanks to a lower fraction of DRs) both stellar populations are more concentrated and the two cumulative distributions are more separated in the former case ($S^5_{10\bullet}$).

4.3.3 A new indicator of BSS segregation: A^+

The results discussed above suggest that the separation between the cumulative radial distributions can be used to measure the level of BSS central segregation with respect to a lighter cluster population taken as reference. We quantitatively define this new indicator as the area between the BSS and the REF cumulative

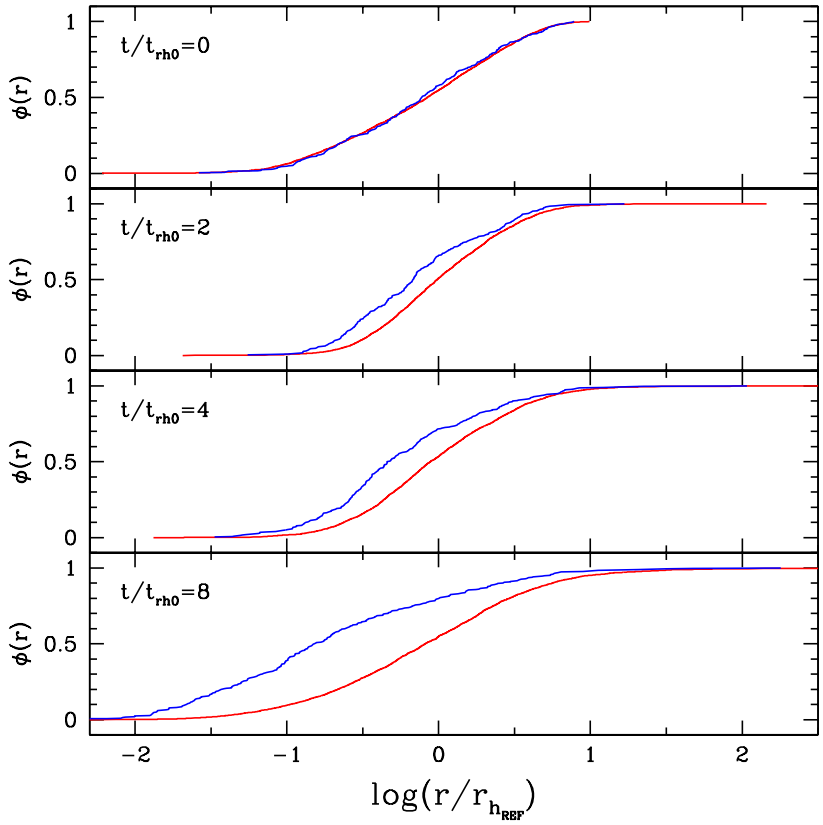

Figure 4.4: From top to bottom, time evolution of the cumulative radial distributions of BSSs (blue lines) and REF stars (red lines), for the $S^8_{30\bullet}$ simulation. The radial scale is logarithmic, with the radius normalized to the half-mass radius of the REF population measured at any considered evolutionary time (see labels). At $t = 0$ the two populations are perfectly mixed and their cumulative radial distributions superimposed. For increasing time, the two distributions become more and more separated due to the effect of mass segregation that preferentially segregates the heavier objects (BSSs) toward the clustre centre. The same qualitative trend is observed in all simulations. From Alessandrini et al. (2016).

radial distributions in the $\phi(r) - \log(r/rh_{\rm REF})$ plane, and we name it A^+ with the following definition:

$$A^+(x) \equiv \int_{x_{min}}^{x} \phi_{\rm BSS}(\xi) - \phi_{\rm REF}(\xi) d\xi. \tag{4.1}$$

In order to allow meaningful comparisons with the observational data, the radial distance is normalized to the half-mass radius of the REF stars. For perfectly mixed populations (as it is the case at $t = 0$ in our models), such a parameter must be equal to zero. Then, A^+ is expected to become positive because the effect of DF is stronger on BSSs (heavier) than on the (lighter) REF stars, and the cumulative radial distributions of the two populations therefore start to separate from each other. According to the scenario presented by Ferraro et al. (2012), as time passes, the value of A^+ is expected to increase progressively, since BSSs orbiting at increasingly

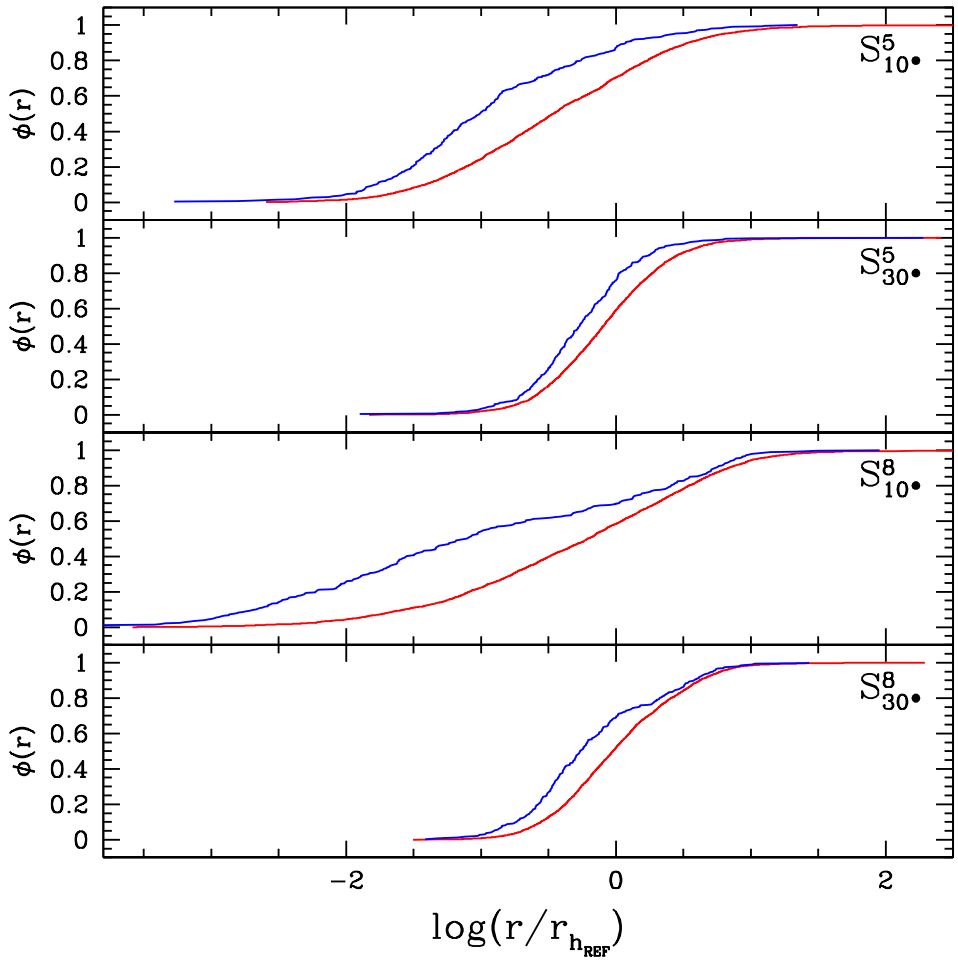

Figure 4.5: Comparison among the cumulative radial distribution of BSSs (blue lines) and REF stars (red lines) at the same evolutionary time ($t = 2.9\ t_{rh0}$) in the four runs including BHs (see labels). The highest central concentration of BSSs (testified by both the lowest inner radius and the largest separation between the two distributions) is found for the $S^8_{10\bullet}$ run (which shows the fastest evolution: cfr with Figs. 4.2). The smallest central segregation of BSSs is observed in the $S^5_{30\bullet}$ cluster (which, in fact, shows the slowest dynamical evolution). From Alessandrini et al. (2016).

larger distances from the cluster centre sink to the bottom of the potential well and the increase of A+ with time corresponds to the formation and the growth of the central peak of the normalized BSS distribution.

Fig. 4.6 shows that A^+ always increases with time and confirms that this parameter is indeed a sensitive indicator of the BSS sedimentation process. The figure confirms that NSs alone have a negligible impact on the rate of central BSS segregation: in fact, for a given value of W_0, there is no significant difference between the models with different percentages of such objects (see, for instance, the red and the cyan dashed lines: S^5_{10} and S^5_{30} runs, respectively), nor between these models and those with the same W_0 but no DRs (compare the lines above with the grey one,

S^5_0, in the figure). Instead, BHs clearly appear to play a crucial role, significanlty slowing down the evolution of the system (see colored solid lines in the figure). In particular, we note that for a given concentration (W_0) and time ($t/t_{\rm rh0}$), the values of A^+ are larger for models with a smaller BH retention. On the other hand, for a given time and a given retention fraction, A^+ is larger for models with a larger initial concentration. At any given value of $t/t_{\rm rh0}$, the largest values of A^+ are found for models with the largest concentration and the smallest BH retention fraction ($S^8_{10\bullet}$), while the smaller values of A^+ are found with lower concentration models with larger BH retention fraction ($S^5_{30\bullet}$). In addition, the parameter is larger in the $S^5_{10\bullet}$ case than in the $S^8_{30\bullet}$ run (at fixed time), demonstrating that the (slowing) effect of a larger percentage of BHs is stronger than the (accelerating) effect of a larger cluster concentration. In our $W_0 = 8$ simulations all BHs are ejected from the system at the end of the run, while three and one BHs are still present at the end of the $S^5_{10\bullet}$ and $S^5_{30\bullet}$ simulations, respectively (see also Heggie, 2014; Hurley et al., 2016 for examples of models in which instead all or a large fraction of BHs are lost during the cluster evolution). The gradual loss of the initial population of BHs allows the BSS to segregate and A^+ to grow and reach values above 0.4-0.5 with a rate that is slower for increasing fractions of BHs. The simulations presented here serve the purpose of illustrating the general effect of a population of black holes on the process of segregation of BSS and the extent to which this effect depends on the fraction of BHs retained. The time evolution of A^+ might differ for clusters with different fractions of BHs. In particular, should the initial fraction of BHs be larger and/or the cluster structural properties allow to retain a larger fraction BHs than those adopted here (see e.g., Morscher et al., 2015; Chatterjee, Rodriguez & Rasio, 2016; Peuten et al., 2016), the rate of BSS segregation (and therefore the growth of A^+) could be slowed down and delayed more than what shown in the few illustrative cases we have explored.

All these properties are consistent with the conclusions of our discussion about the segregation process in terms of evolution of the Lagrangian radii (see Sect. 4.3.1) and show that the new parameter A^+ is a reliable indicator of the cluster dynamical evolution as traced by the BSS population.

Fig. 4.6 also shows that the time dependence of A^+ is characterized by two main regimes: an initial, slower phase, followed by a steeper trend toward the end of the simulations, at times approaching the CC time. This effect is more evident if BHs are included: the evolutionary times when the curves change regime are $t \approx 4.2$, 5.5, 2 and 6.2 $t_{\rm rh0}$ in the $S^5_{10\bullet}$, $S^5_{30\bullet}$, $S^8_{10\bullet}$ and $S^8_{30\bullet}$ runs, respectively. These epochs also correspond to the moment when the time dependence of the inner BSS Lagrangian radii also change slope, while those of the REF population evolve in a slower, smoother way (see Figs. 4.2 and 4.3). The fact that A^+ shows a regime of faster time dependence when the cluster is approaching the CC phase further

demonstrates that it is an indicator of the level of BSS segregation and dynamical evolution of the system.

Figure 4.7 shows the evolution of A^+ as a function of time normalized to the CC time of the BSS and REF populations ($t_{\rm CC}$). Interestingly, all the models fall on a relatively narrow band in this plane, irrespective of the amount and the mass of DRs they contain. This suggests that A^+ might be used as an approximate indicator of how far a cluster is from CC of the visible component.

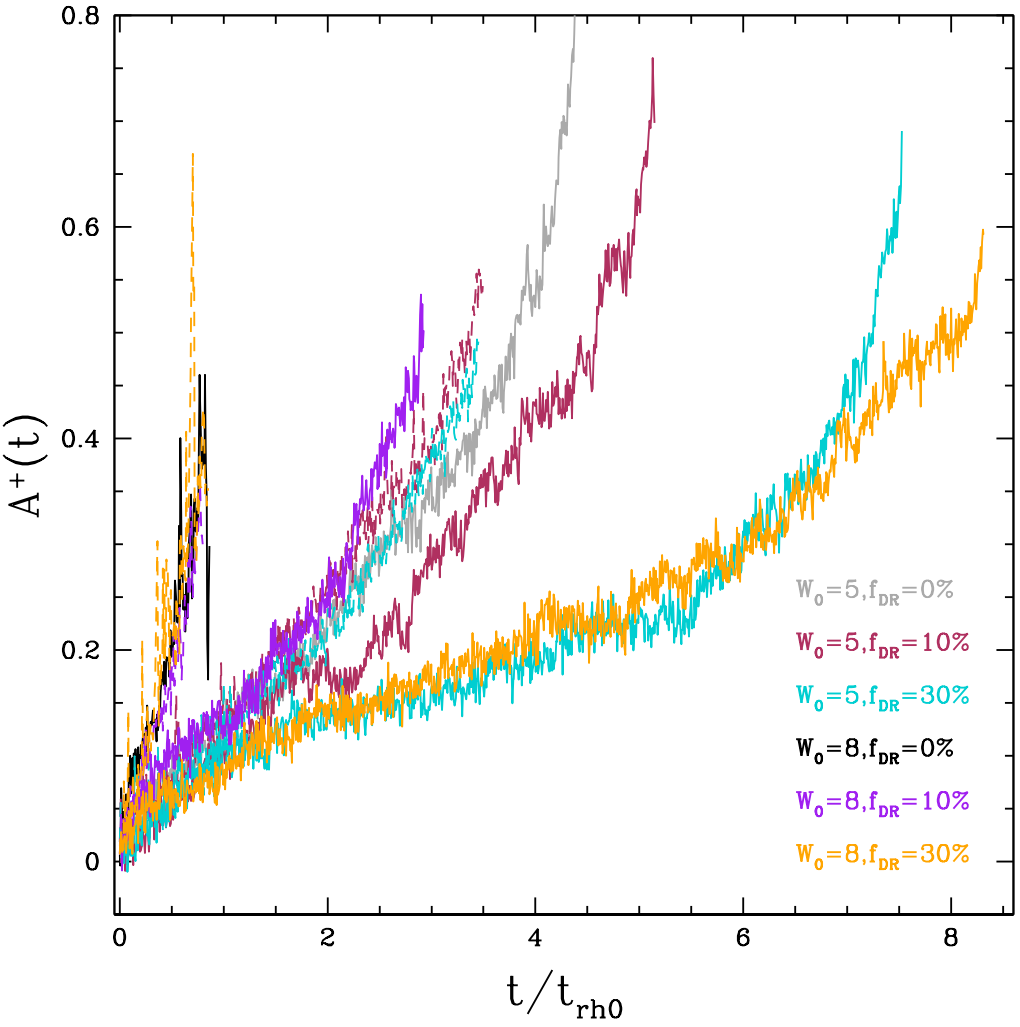

Figure 4.6: Evolution of A^+ as a function of the time normalized to $t_{\rm rh0}$ in the all our models: simulations with no DRs are plotted in grey and black for the $W_0 = 5$ and $W_0 = 8$ cases, respectively; the dashed lines refer to models with only NSs, while the solid lines correspond to the simulations including both NSs and BHs (see the labels for the color code). A^+ increases with time as expected for a reliable mass segregation and dynamical evolution indicator (see Sect. 4.3.3). From Alessandrini et al. (2016).

Finally, in order to illustrate how the strength of the mass segregation depends on the populations chosen, in Fig. 4.8 we compare the time evolution of the A^+

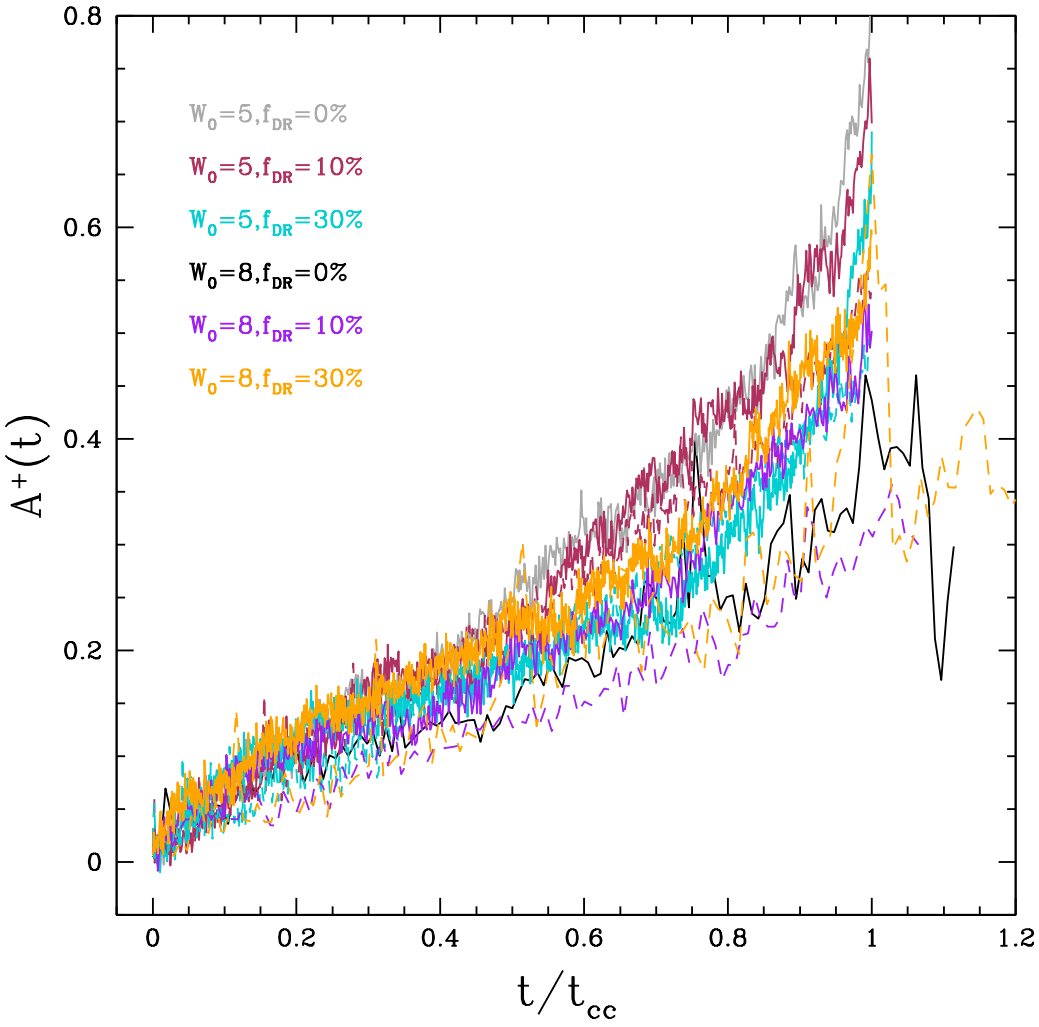

Figure 4.7: Same as Fig. 4.6, but with the time normalized to the CC time of BSSs and REF stars in every model ($t_{\rm CC}$). From Alessandrini et al. (2016).

parameter calculated for BSSs and REF stars (black curves, the same as those plotted in colors in Fig. 4.6) and the time evolution of the A^+ parameter calculated using REF and $m = 0.4 M_\odot$ particles (grey curves). In the former case the mass ratio between the two populations is 1.5, while it is larger (equal to 2) in the latter. While in both cases A^+ increases with time, the effect is much stronger in the former. This is because, in spite of a smaller mass ratio between the former populations (BSSs and REFs), the relative effect of mass segregation on these components is stronger than that on REF and $0.4 M_\odot$ stars. This behaviour suggests that BSSs are more powerful observational tracers of dynamical evolution than, for instance, main sequence stars.

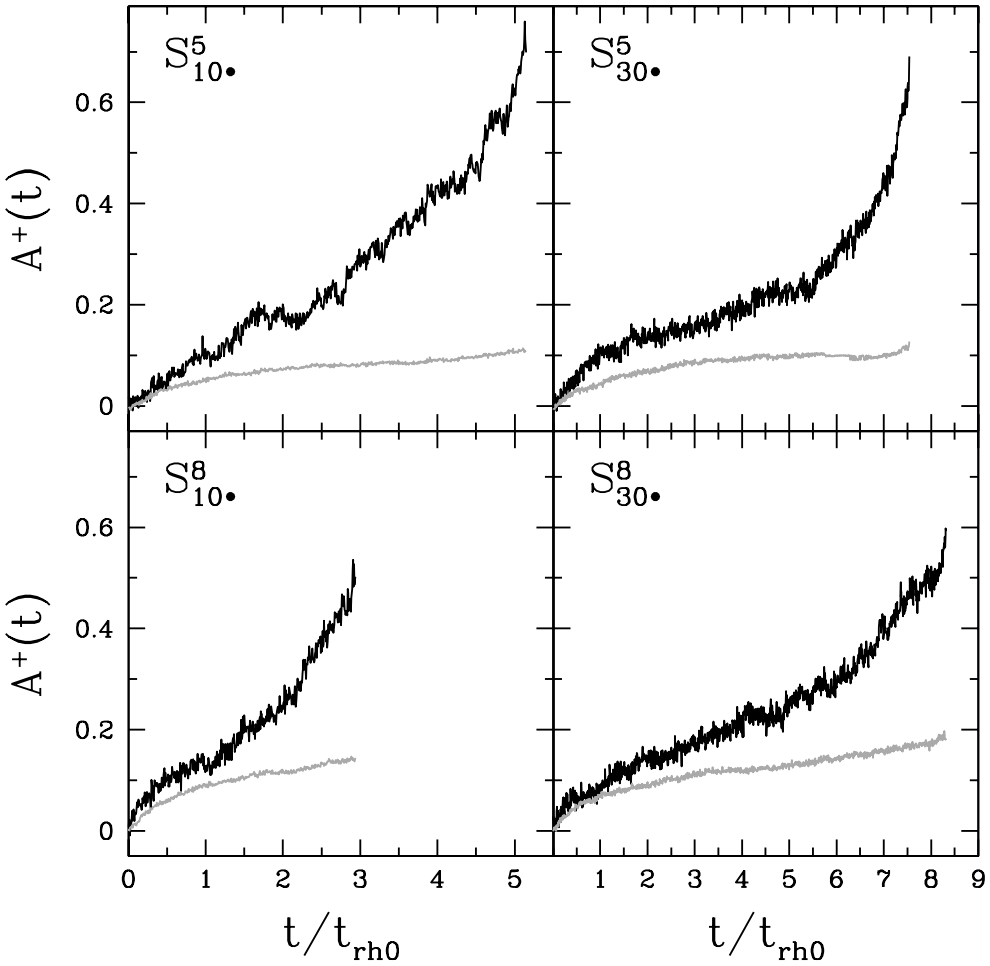

Figure 4.8: Same as Fig. 4.6, but with the time normalized to the CC time of BSSs and REF stars in every model (t_{CC}). From Alessandrini et al. (2016).

Chapter 5

The A^+ parameter: observational results

5.1 Introduction

As described in Chapter 4, in Alessandrini et al. (2016) we used N-body simulations with 10^5 particle and different fractions of heavy dark remnants to investigate the effect of dynamical friction on BSSs in GCs, and we proposed a new parameter (A^+, Chapter 4, Eq. 4.1) to measure the level of BSS segregation. We also demonstrated that A^+ is a powerful indicator of the dynamical evolution of the host cluster and can therefore be used as an alternative hand of the dynamical clock (alternative to r_{min}, i.e., the minimum of the BSS-nRD).. Given this theoretical results obtained from N-body simulations, it is now crucial to study this parameter also from the observational point of view. To this aim, we empirically determined the value of A^+ in a sample of 25 Galactic GCs and we checked for correlations with other dynamical evolution indicators.

In Sect. 5.2 the data-set is presented. Sect. 5.3 describes the method used for the determination of A^+ from the observations. Finally, the results are showed in Sections 5.4.1 and 5.4.2.

5.2 Sample selection and description of the data-set

The sample selected for the empirical estimate of A^+ consists of the same 21 GCs previously used to define the dynamical clock (Ferraro et al., 2012), plus four additional clusters discussed in subsequent papers (Dalessandro et al., 2013b; Beccari et al., 2013; Sanna et al., 2014; Dalessandro et al., 2015).

The central regions of each cluster have been typically observed in the ultraviolet band with the Wide Field Planetary Camera 2 (WFPC2) on board the Hubble Space Telescope (HST), and, where possible, with complementary optical observations secured with the HST Advanced Camera for Surveys (ACS). The outskirts

of the clusters have been sampled by means of optical, ground-based observations performed with wide-field imagers, as the WFI@ESO and MegaCam@CFHT. Since BSSs are most reliably distinguishable from other cluster populations in the UV color-magnitude diagram (see Ferraro et al. 2015), we generally used this plane to define the BSS selection box. The latter is then transformed into the optical planes by using sub-samples of BSSs observed in both the UV and the optical bands. As reference populations we generally considered RGB, sub-giant branch (SGB), and/or HB stars, depending on the cluster properties and the available photometric data. In order to allow unbiased comparisons, their selection was performed using the same photometric catalogues adopted for the BSSs. However, depending on the surface temperature of each stellar population, we used the UV color-magnitude diagrams to select (hot) HB stars, and the optical planes for the (cool) RGB/SGB reference samples, so to avoid any completeness bias. In the case of more than one reference population, we have verified that the corresponding radial distributions are in mutual agreement. This guarantees that any adopted reference population can be equivalently used for the determination of A^+.

5.3 Observational determination of A^+

By definition (see Chapter 4 Sect. 4.3.3), A^+ depends on the considered cluster-centric distance. Hence a meaningful cluster-to-cluster comparison requires that the parameter is measured over equivalent radial portions in every system and that the adopted region is large enough to be sensitive to the phenomenon that A^+ is describing (the effect of dynamical friction on BSSs). By using the set of N-body simulations discussed in Alessandrini et al. (2016), we verified that the value of the parameter computed at one half-mass radius (r_h) is always representative of the cluster global value (i.e., the value attained if the entire radial extension is considered), corresponding to $\sim 70-80\%$ of it in all our runs. We also note that in the analysis of Ferraro et al. (2012), the level of BSS sedimentation is parametrized by the value of $R_{\rm BSS}$: a central peak in the BSS-nRD corresponds to $R_{\rm BSS} > 1$, indicating that the observed number of BSSs is in excess with respect to what expected from the sampled luminosity. Interestingly, values of $R_{\rm BSS} > 1$ are observed at $r < r_h$ in all clusters belonging to Family II and Family III. This confirms that the region included within one half-mass radius is the most sensitive to the BSS sedimentation process. Thus, for a meaningful cluster-to-cluster comparison, in each system we determined the value of A^+ within one half-mass radius from the center[1]

[1]The available HST data are sufficient to cover such a region in almost all the selected clusters. Exceptions are M3, M4 and M55, for which also complementary wide-field catalogues are needed, and the clusters NGC 5466 and Palomar 14, which, in virtue of their low density, have been entirely sampled with ground-based observations (with LBC@LBT and MegaCam@CFHT, respectively; see Beccari et al., 2013, 2011). In the case of 47 Tucanae only the WFPC2 data discussed in Ferraro

(hereafter A^+_{rh}). As expected, in the cases where two reference populations (HB and RGB/SGB) are available, the two resulting values of A^+_{rh} are very similar. We therefore adopted their mean value as the best estimate, and the standard deviation as their error. Since these latter range between 0.01 and 0.03, we attributed an error of 0.02 to all the cases where only one reference population is available. The values thus obtained are listed in Table 5.1, together with a few key parameters of the program clusters.

5.4 Results and Discussion

5.4.1 Correlation between A^+ and $r_{\rm min}$

In Figure 5.2 (left-hand panels) the cumulative radial distributions of BSSs and REF stars for four GCs in our sample is shown. The labelled values of A^+_{rh} (see also Table 5.1) correspond to the size of the shaded areas: formally zero for ω Cen, which has a non-segregated BSS population (Family I cluster in the dynamical clock formalism), and up to 0.52 for M30, which is one of the dynamically oldest system (Family III) in the sample, with BSSs much more centrally concentrated than the REF population. As listed in Table 5.1, the parameter is smaller than 0.05 also for the other three GCs with non-segregated BSS populations known so far, namely Palomar 14, NGC 2419 and NGC 6101. In all the other cases, it assumes larger values, depending on the separation between the BSS and the reference star cumulative distributions. Qualitatively, this is exactly the behavior expected from a reliable indicator of BSS segregation. In the right-hand panels of the figure we plot the radial distributions of the BSS double normalized ratio $R_{\rm BSS}$ for the same four clusters, with the black arrows indicating the position of the minimum, epressed in units of the cluster core radius (r_c). The figure clearly shows that the increase of A^+_{rh} seen from top to bottom in the left panels is accompanied by a systematic increase of $r_{\rm min}/r_c$ in the corresponding right-hand panels, thus indicating that these two parameters are mutually linked, as expected if they describe the same phenomenon.

For a closer comparison with results of Ferraro et al. (2012), we investigate the relation between A^+_{rh} and the parameter $\log(r_{\rm min}/r_c)$ for the entire sample of 25 GCs. We point out that, although both these quantities describe the progressive central segregation of BSSs, their definitions are completely independent and, in principle, they could be completely uncorrelated. Figure 5.3 shows, instead, that the two parameters are linked through a quite tight and direct correlation. Indeed, the Spearman rank correlation coefficient between A^+_{rh} and $r_{\rm min}/r_c$ is $\rho = 0.77$, corresponding to a probability $P > 99.99\%$ that the two parameters are correlated. The significance remains very high ($P > 99.7\%$) even if one (arbitrarily) excludes

et al. (2004) have been used.

Name	r_c	r_h	$\log(t_{\rm rc})$	$r_{\rm min}$	A^+_{rh}	ϵ
ω Centauri	153.0	443.7	9.86	0.0	-0.010	0.010
Palomar 14	41.0	69.7	9.68	0.0	-0.010	0.010
NGC 6101	61.3	128.2	9.38	0.0	0.030	0.018
NGC 2419	20.0	54.0	10.08	0.0	0.035	0.007
NGC 5466	72.0	213.8	9.42	180.0	0.100	0.020
M55	99.0	215.8	9.00	405.0	0.100	0.020
M4	70.0	308.0	8.00	350.0	0.120	0.014
NGC 288	88.0	167.2	9.19	250.0	0.130	0.014
M53	26.0	98.8	9.08	55.0	0.150	0.014
M5	27.0	124.2	8.43	255.0	0.150	0.020
M10	41.0	139.8	8.26	425.0	0.160	0.000
M13	49.5	148.5	9.03	185.0	0.165	0.007
M2	17.0	57.8	8.48	150.0	0.170	0.028
NGC 6388	7.2	45.4	8.08	32.5	0.190	0.020
NGC 362	13.0	73.8	8.08	515.0	0.200	0.020
M79	9.7	47.5	7.98	325.0	0.250	0.020
M92	14.0	84.0	8.05	250.0	0.255	0.007
M3	30.0	186.0	8.75	125.0	0.260	0.020
NGC 5824	4.4	29.0	8.28	20.0	0.280	0.028
47 Tucanae	21.0	201.6	7.96	200.0	0.290	0.020
NGC 6229	9.5	30.4	8.72	25.0	0.290	0.000
M80	7.0	40.6	7.57	375.0	0.290	0.014
NGC 6752	13.7	194.5	7.37	325.0	0.325	0.021
M75	5.4	29.2	8.00	225.0	0.380	0.020
M30	4.3	109.2	6.79	385.0	0.520	0.000

Table 5.1: Structural/dynamical parameters and values of A^+_{rh} for the program clusters: core radius and half-mass radii in arcseconds (columns 2 and 3), logarithm of the central relaxation time in Gyr (column 4), value of $r_{\rm min}$ in arcseconds (column 5), value of A^+_{rh} and its error (columns 6 and 7). The values of the structural/dynamical parameters come from Ferraro et al. (2012), Dalessandro et al. (2013a,b), Beccari et al. (2013), Sanna et al. (2014), and Dalessandro et al. (2015). For NGC 6101 the value of $\log(t_{\rm rc})$ has been recomputed by following equation (10) in Djorgovski (1993) for homogeneity with the other clusters. From Lanzoni et al. (2016).

from the sample the most extreme points (namely, M30 and the four Family I GCs), or if limiting the analysis to the 13 clusters with the smallest errors on A^+_{rh} ($\epsilon < 0.02$). This confirms that A^+_{rh} and $r_{\rm min}/r_c$ are actually different ways of measuring the same physical mechanism: as discussed in Ferraro et al. (2012), the underlying process is dynamical friction, which, as clusters get dynamically older, progressively removes BSSs at increasingly larger distances from the center (thus generating a minimum at increasingly larger values of $r_{\rm min}/r_c$) and accumulates them toward the cluster center

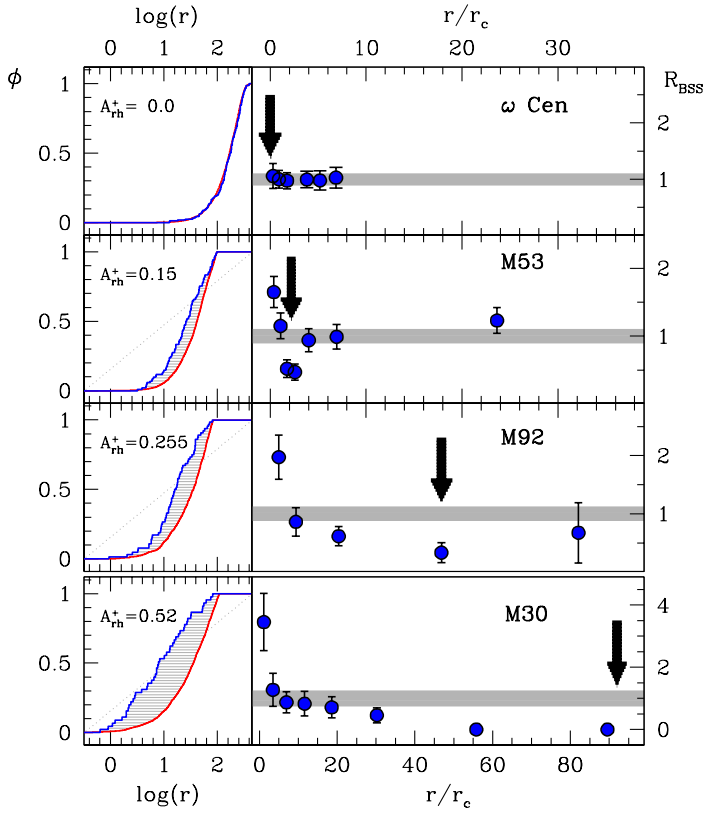

Figure 5.2: *Left panels:* Cumulative radial distributions of BSSs (blue line) and REF stars (red line) observed within one half-mass radius (r_h) in four GCs of the considered sample (from top, to bottom: ω Centauri, M53, M92 and M30). The distance from the center (r) is in arcsecond units. The size of the area between the two curves (shaded in grey) corresponds to the labelled value of A^+_{rh} (see also Table 5.1). *Right panels:* BSS normalized radial distribution ($R_{\rm BSS}$, blue circles) for the same clusters shown in the left panels. The black arrows mark the position of the BSS-nRD minimum ($r_{\rm min}/r_c$). The grey strips schematically show the distribution measured for the REF population. From Lanzoni et al. (2016).

(thus increasing A^+_{rh}). As discussed in Alessandrini et al. (2016), the process of BSS segregation can be delayed by the presence of dark remnants and in particular by a population of stellar mass black holes. This adds another important element to the information contained in the BSS segregation level and the parameter introduced to measure it.

5.4.2 Correlation between A^+ and the central relaxation time t_{rc}

The results obtained suggest that A^+_{rh} could be used as an alternative indicator of the level of dynamical evolution experienced by star clusters since their formation, and we should expect that is related to other parameters measuring the dynamical

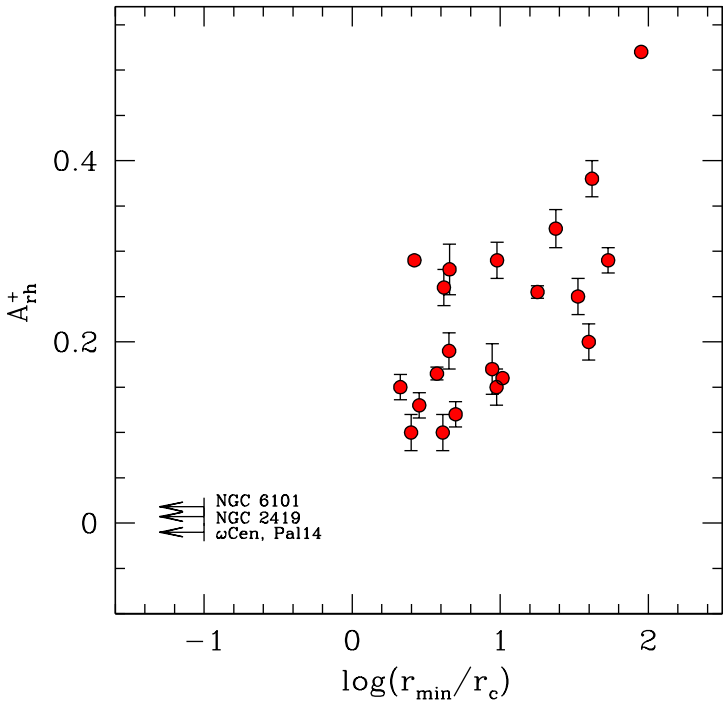

Figure 5.3: Parameter A^+_{rh} as a function of the observed position of the BSS-nRD minimum ($r_{\rm min}/r_c$) expressed in logarithmic units. For Family I clusters, with an everywhere flat BSS-nRD, a value $r_{\rm min}/r_c = 0.1$ has been arbitrarily assumed as an upper limit (see arrows). From Lanzoni et al. (2016).

evolution time-scale. Indeed, Ferraro et al. (2012) found a nice correlation between the cluster-centric distance of the minimum of the BSS-nRD ($r_{\rm min}/r_c$) and the central relaxation time of the cluster (t_{rc}). Figure 5.4 shows that the latter is tightly related also to A^+_{rh}, in the sense that the proposed new parameter systematically decreases for increasing values of the relaxation time. The Spearman rank correlation coefficient between A^+_{rh} and t_{rc}/t_H (with $t_H = 13.7$ Gyr being the Hubble time) is $\rho = -0.81$, corresponding to $P > 99.99\%$, and it decreases only to $\rho = -0.63$ ($P = 99.7\%$) if Family I clusters and M30 are (arbitrarily) excluded from the sample. Also the Pearson correlation coefficient is very high ($r = -0.85$), indicating a strong linear correlation between A^+_{rh} and $\log(t_{rc}/t_H)$. As apparent from the figure, the relation between these two variables shows some scatter. This may indicate that further refinements should be used to measure A^+_{rh}, or, more likely, that the values of t_{rc} empirically estimated by following Djorgovski (1993) are rough approximations of the true relaxation times of Galactic GCs (as discussed, e.g., by Chatterjee et al., 2013b from dedicated Monte Carlo simulations). Beside the scatter, however, our analysis fully confirms that A^+_{rh} is a powerful indicator of cluster dynamical evolution and, once properly calibrated, it promises to be usable as an alternative, and

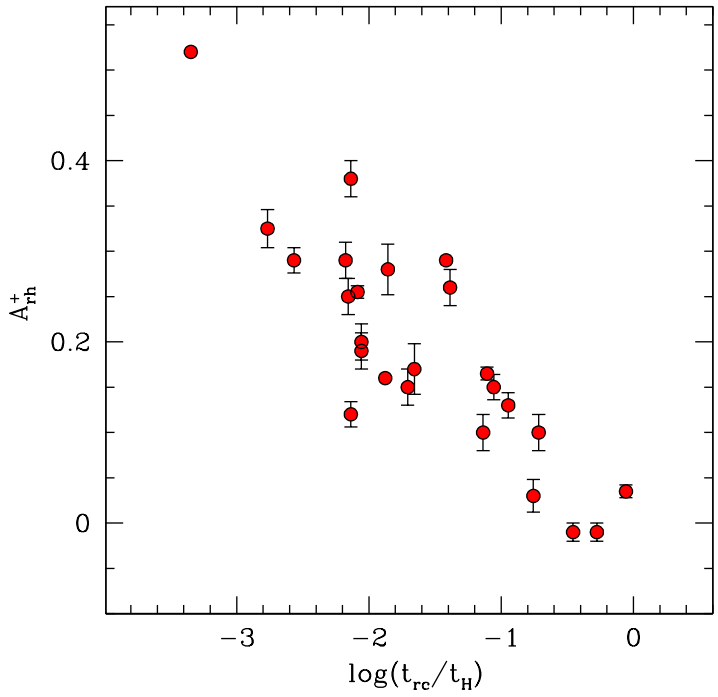

Figure 5.4: Relation between the new parameter A^+_{rh} and the logarithm of the cluster central relaxation time ($t_{\rm rc}$) normalized to the Hubble time ($t_H = 13.7$ Gyr). From Lanzoni et al. (2016).

hopefully more precise, measure of the central relaxation time of GCs.

In the framework of the dynamical clock originally defined by Ferraro et al. (2012) in terms of the position of the minimum in the BSS-nRD ($r_{\rm min}/r_c$), the new parameter A^+ corresponds to a new clock-hand, while the engine of the clock remains the same (the dynamical friction process). From the observational point of view, the advantage of this new clock-hand is that it is easier to measure and somehow less "fragile" than the position of the BSS-nRD minimum. In fact, for determining $r_{\rm min}$ it is necessary to sample the entire cluster radial extension (typically by means of a combination of HST and wide-field, ground-based observations), while only the central regions ($r < r_h$), possibly probed just by HST, are sufficient to measure A^+_{rh}. Moreover, it does not require any (somehow arbitrary) assumption on the radial binning (which is instead needed to build the BSS-nRD). Finally, from its own definition, $r_{\rm min}$ is located in a region of "low signal", where DF is removing heavy stars and the number of BSSs reaches its minimum (the so called "zone of avoidance"; Mapelli et al., 2004, 2006); instead A^+_{rh} is measured in a "high signal" region, where dynamical friction is accumulating heavy stars and the number of BSSs reaches its maximum. Thus, the proposed change of clock hand makes the reading of the dynamical clock easier and less prone to low statistics uncertainties.

Chapter 6

Conclusions

In the work described in this Thesis, we investigated the problem of modeling blue straggler star (BSS) dynamics in globular clusters (GCs) to obtain a deeper physical understanding of why and how these objects can be used as probes the dynamical evolution of the host system. Being these stars more massive than the average stars in GCs, they are indeed subject to dynamical friction (DF), which causes their sinking and segregation toward the cluster centre. In particular, the shape of the BSS normalized radial distribution (BSS-nRD) has been observed to be of three different types in GCs: a flat distribution (i.e., with BSSs distributed as the average stars), a bimodal one, with a central peak and minimun in the intermediate regions followed by an outer rising branch, and unimodal distribution, which just shows a central peak and a monotonically decreasing trend outward. This result has been interpreted by Ferraro et al. (2012) as the proof of different dynamical stages reached by the investigated clusters, with the progressive migration of the minimum toward larger distances from the centre being used as a clock hand able to measure the dynamical age of GCs, thus defining the so called "dynamical clock" scenario.

This Thesis had the goal of searching for these observed features in different sets of N-body simulations, trying to identify and discern all the physical processes that contribute in shaping the BSS-nRD during the dynamical evolution of GCs. To this aim, we constructed models of GCs with progressively increasing levels of realism (and complexity), step by step adding to the simulations several ingredients that can significantly affect the dynamical evolution of the system.

First of all, we provided an analytical method to calculate the DF timescale in a system of particles distributed with a mass spectrum (as a GC is) expanding on the original work by Ciotti (2010). 2010). While this latter study was focussed on the specific case of a homogenous background, we evolved the system by means of direct and collisional N-body simulations. To our knowledge, this is the first numerical study of DF in the presence of a self-consistently evolving field of particles with

unequal masses and for a test star with a mass comparable to that of the field. We explored both the mono-mass case (where all particles have unit mass and the test star decelerated by DF is four times more massive), and the multi-mass case (with three field components of masses m_1, $m_2 = 2\,m_1$, $m_3 = 3m_1$ and total numbers N_1, N_2, N_3, and with the test particle having $m_t = 4m_1$). Each simulation was run with a total of $N = 10^4$ particles initially distributed as a spherical and isotropic King model with dimensionless potential $W_0 = 4$ in the mono-mass case, and $W_0 = 4, 6, 8$ in the multi-mass one.

We found that the radial behavior of $t_{\rm DF}$ is always monotonic ($t_{\rm DF}$ increasing with r), both in the mono-mass case and in the presence of a mass spectrum, independently of the evolutionary time and the initial concentration of the system. In all cases, the largely dominant factor in determining the shape of $t_{\rm DF}(r)$ is the total mass density profile. Moreover, we also found that approximating a multi-mass system as single-mass cluster (made of stars with masses equal to the average particle mass) can lead to a systematic overestimate of $t_{\rm DF}$ within the half-mass radius, up to a factor of 3 in the innermost regions. This implies that care must be used when adopting the average properties of background populations to obtain quantitative estimates of $t_{\rm DF}$ if the system is composed of stars of different masses.

The $N-$body simulations and the overall approach presented in this work are certainly a rough simplification of the much more complex problem of DF in real GCs. First of all, the total number of simulated particles is much smaller than the number of stars in a cluster. However, while this affects the overall cluster evolution time-scale, it is not expected to impact the conclusions about the radial monotonicity of $t_{\rm DF}$. The same considerations apply to the assumptions adopted for the mass spectrum (only three discrete bins): a larger number of finer mass groups is not expected to induce a non-monotonic behavior on $t_{\rm DF}(r)$, since the density profile $\rho(r)$ would still be a monotonic decreasing function of radius, but it can modify the overall cluster evolution. Hence, the monotonic behaviour found in all cases for $t_{\rm DF}(r)$ appears to be a quite solid result, further supporting the scenario proposed by Ferraro et al. (2012), where $t_{\rm DF}(r)$ is implicitly assumed to be monotonic at all times and the bimodal behaviour of the observed BSS-nRD is due to the fact that DF progressively affects larger clustercentric distances as a function of time.

We then studied the problem of the BSS radial distribution in GCs with the same simulations used in the previous work but from another point of view. In particular, we used the heaviest component (with mass m_3) to represent the BSS population in a cluster made of N_1 field stars with mass m_1 and N_2 reference stars (RGB or HB objects) with mass m_2. We followed the evolution of BSSs and REF stars in the evolving background, to explore the role of DF in shaping the BSS-nRD in these simulated systems. Our goal has been to verify whether some dynamical process can drive the BSS radial distribution from being flat to be unimodal, passing through

the bimodal shape, as predicted in the dynamical clock scenario.

Our simple N-body models clearly showed the formation of a central peak in the BSS-nRD in all the cases considered. Also the bimodal shape of the BSS-nRD is present for long periods in almost all the simulated systems. The lowest concentrated cluster, however, shows only the formation of the central peak without any bimodality, at odds with the observations. We finally verified that increasing the number of particles by one order of magnitude (from 10^4 to 10^5) leads to a more accurate description of the dynamics occurring in real GCs, as well as to a more gradual evolution of the BSS radial distibution.

Prompted by this last result, we decided to increase the number of particles in our simulations. Moreover, in order to improve the realism of our model, we admitted the presence of a population of dark remnants (DRs), consisting of neutron stars (NSs) and stellar-mass black holes (BHs) which are both heavier than BSSs and can therefore significantly affect the overall cluster evolution and the process of mass segregation. Thus, we performed a set of direct N-body simulations of GCs with $N \sim 10^5$ particles, with different initial concentrations ($W_0 = 5$ and $W_0 = 8$), including a population of BSSs (modelled as single particles of $1.2M_\odot$) and different fractions of NSs and BHs (we also modelled the case of systems with no heavy DRs at all, for the sake of comparison).

We have shown that the segregation of BSSs and of the most massive main sequence stars is significantly slowed down by the presence of BHs. This is due to the dynamical heating effect of these heavy objects that rapidly decouple from the other components, form a centrally concentrated sub-system and inhibit the radial segregation of the less massive components. The effect of BHs has been revealed to be stronger than that of concentration: in fact, while in the absence of BHs, the central segregation of BSSs and REF stars is much faster for $W_0 = 8$, than for $W_0 = 5$, the opposite occurs (i.e., the evolution becomes slower in the highest concentration cluster) if the $W_0 = 8$ system host a larger fraction of BHs.

Furthermore, in this work we have introduced a new parameter (A^+) as a new tool to measure the sedimentation level of BSSs and probe the host cluster dynamical evolution. The parameter is defined as the area between the cumulative radial distribution of BSSs and that of REF stars. We found that A^+ shows a clear increasing trend with time that well reflects the evolution of the Lagrangian radii observed in the simulations, with analogous dependences on the cluster concentration and the DR retention fraction. As the system evolves and loses part of the initial population of BHs, the level of BSS segregation grows at an increasing rate and diverges from that of the REF stars. As a consequence, the time dependence of A^+ shows a change in the slope. This demonstrates that A^+ is indeed a very good tracer of BSS segregation, and can reveal both how advanced BSS segregation is and the extent to which the presence of a DR population has inhibited it. In all the considered

simulations, the parameter assumes comparable values at any fixed fraction of the CC time. Hence, it seems to be a good indicator of the time remaining to the CC of the visible component, reasonably irrespective of the initial concentration and DR content of the system.

On the observational side, we provided the first empirical determination of A^+ in a sample 25 of Galactic GCs, for which the BSS and REF radial distributions have been determined all over the cluster extention, from the central to the external regions, by using ultraviolet observations with the Wide Field Planetary Camera 2 (WFPC2) on board the Hubble Space Telescope (HST) and optical data from wide-field imagers. Where possible, for the internal regions we also used complementary optical observations secured with the HST Advanced Camera for Surveys (ACS).

Clearly, the parameter A^+ defined in Alessandrini et al. (2016) depends (by definition) on the sampled radial distance, and the target GCs have different physical sizes. Hence, for a meaningful cluster-to-cluster comparison, A^+ has been determined from the cumulative distributions of BSSs and REFs computed within the half-mass radius in all the targets (and we therefore refer to it as A^+_{rh}). This choice does not invalidate our results, since A^+ mainly describes the growing of the central peak of the BSS-nDR, which interests the most central regions of the cluster.

We found a good correlation between A^+_{rh} and the minimum of the BSS-nRD (normalized with the core-radius of each cluster) previously used by Ferraro et al. (2012) to define the dynamical clock hand, thus indicating that these two parameters are mutually linked, and both trace the same phenomenon. In particular, A^+_{rh} has been observed to be ~ 0 for ω Cen and very small ($A^+_{rh} < 0.05$) for the other sampled clusters which have a non-segregated BSS population (Palomar 14, NGC 2419 and NGC 6101), while it assumes larger values for the other GCs in the sample, up to the case of M30 which has $A^+_{rh} = 0.52$, in accordance with its definition of dynamically-old system. Qualitatively, this is exactly the behavior expected from a reliable indicator of BSS segregation, suggesting that this new parameter could be used as an alternative indicator of the level of dynamical evolution experienced by star clusters since their formation.

We have also found a correlation between A^+_{rh} and the central relaxation time of the clusters (t_{rc}) empirically estimated by following Djorgovski (1993), further confirming that A^+_{rh} is a powerful indicator of cluster dynamical evolution and, once properly calibrated, it promises to be usable as an alternative, and hopefully more precise, measure of the central relaxation time of GCs.

From the observational point of view, this new clock hand is easier to measure and less "fragile" than the position of the BSS-nRD minimum. In fact, for determining $r_{\rm min}$ it is necessary to sample the entire cluster radial extension, while only the central regions within the half-mass radius are sufficient to measure A^+_{rh}. Moreover, it does not require any (somehow arbitrary) assumption on the radial binning (at

odds with BSS-nRD which needs it). Finally, from its own definition, $r_{\rm min}$ is located in a region of "low signal", where DF causes a depletion of BSSs (and heavy stars in general), which, in turn, reach their minimum; A^+_{rh} is instead measured in a "high signal" region, where DF accumulates heavy stars and the BSS number reaches its maximum. Thus, the proposed change of clock hand makes the reading of the dynamical clock easier and less subject to low statistics uncertainties.

More realistic N-body simulations are now required to provide a calibration of A^+ as a function of the cluster dynamical age expressed in Gyr. We emphasize that, while this seems to be within the range of performances of the current generation of N-body simulations, such an aim requires simulations including virtually all the known ingredients (as dark remnants, primordial binaries, external tidal field, etc.).

These are indeed the future perspectives of this Thesis project, and we already started to work in this direction. In fact, we generated the initial conditions for a new set of simulations similar to the previous ones (containing 10^5 particles and different fractions of heavy DRs, as in Alessandrini et al., 2016), but with an additional level of complexity and realism: a primordial population of binary systems, to which also BSSs belong (instead of being modeled point-mass particles). In particular, we adopted a primordial binary fraction $f_{\rm bin} = 3\%$ and we labeled as BSSs all binaries having a hardness ratio[1] $\sim 700 - 800$. The work is still in progress, with a few run already ended, some simulations still running and the analysis of the outputs ongoing.

[1]The hardness ratio is the ratio between the binary binding energy and the cluster mean kinetic energy

Publications

- **Alessandrini E.**, Lanzoni B., Miocchi P., Ciotti L., Ferraro F. R., *Dynamical friction in multi-component evolving globular clusters*, 2014, ApJ, 795, 169.
- Miocchi P., Pasquato M., Lanzoni B., Ferraro F. R., Dalessandro E., Vesperini E., **Alessandrini E.**, Lee Y.-W., *Probing the role of dynamical friction in shaping the BSS radial distribution. I. semi-analytical models and preliminary N-body simulations*, 2015, ApJ, 799, 44.
- **Alessandrini, E.**, Lanzoni, B., Ferraro, F. R., Miocchi, P., Vesperini, E., *Investigating mass segregation process in globular clusters with Blue Straggler Stars: the impact of dark remnants*, 2016, ArXiv e-prints.
- Lanzoni, B., Ferraro, F.R., **Alessandrini, E.**, Dalessandro, E., Vesperini, E., Raso, S., *The dynamical clock reloaded: defining a new clock-hand*, 2016, *ApJ Submitted.*

Bibliography

Aarseth S. J., 1999, PASP, 111, 1333

Aarseth S. J., 2003, Gravitational N-Body Simulations. p. 430

Aarseth S. J., Heggie D. C., 1998, MNRAS, 297, 794

Alessandrini E., Lanzoni B., Miocchi P., Ciotti L., Ferraro F. R., 2014, ApJ, 795, 169

Alessandrini E., Lanzoni B., Rosario Ferraro F., Miocchi P., Vesperini E., 2016, ArXiv e-prints

Anderson J., 2002, in Astronomical Society of the Pacific Conference Series, Vol. 265, Omega Centauri, A Unique Window into Astrophysics, van Leeuwen F., Hughes J. D., Piotto G., eds., p. 87

Applegate J. H., 1986, ApJ, 301, 132

Arca-Sedda M., Capuzzo-Dolcetta R., 2014, ApJ, 785, 51

Arena S. E., Bertin G., Liseikina T., Pegoraro F., 2006, A&A, 453, 9

Armandroff T. E., 1989, AJ, 97, 1532

Auriere M., Lauzeral C., Ortolani S., 1990, Nature, 344, 638

Bailyn C. D., 1995, ARA&A, 33, 133

Banerjee S., Baumgardt H., Kroupa P., 2010, MNRAS, 402, 371

Barnes J., Hut P., 1986, Nature, 324, 446

Baumgardt H., 2001, MNRAS, 325, 1323

Baumgardt H., Hut P., Heggie D. C., 2002, MNRAS, 336, 1069

Baumgardt H., Kroupa P., 2007, MNRAS, 380, 1589

Baumgardt H., Makino J., 2003, MNRAS, 340, 227

Baumgardt H., Makino J., Ebisuzaki T., 2004, ApJ, 613, 1143

Beccari G., Dalessandro E., Lanzoni B., Ferraro F. R., Sollima A., Bellazzini M., Miocchi P., 2013, ApJ, 776, 60

Beccari G., Sollima A., Ferraro F. R., Lanzoni B., Bellazzini M., De Marchi G., Valls-Gabaud D., Rood R. T., 2011, ApJL, 737, L3

Bedin L. R., Piotto G., Anderson J., Cassisi S., King I. R., Momany Y., Carraro

G., 2004, ApJL, 605, L125

Bertin G., 2000, Dynamics of Galaxies. p. 430

Bertin G., Liseikina T., Pegoraro, 2003, A&A, 405, 73

Bertin G., Liseikina T., Pegoraro F., 2004, in American Institute of Physics Conference Series, Vol. 703, Plasmas in the Laboratory and in the Universe: New Insights and New Challenges, Bertin G., Farina D., Pozzoli R., eds., pp. 314–317

Bettwieser E., Sugimoto D., 1984, MNRAS, 208, 493

Binney J., 1977, MNRAS, 181, 735

Binney J., Tremaine S., 2008, Galactic Dynamics: Second Edition. Princeton University Press

Boily C. M., Kroupa P., 2003a, MNRAS, 338, 665

Boily C. M., Kroupa P., 2003b, MNRAS, 338, 673

Bontekoe T. R., van Albada T. S., 1987, MNRAS, 224, 349

Breen P. G., Heggie D. C., 2012a, MNRAS, 425, 2493

Breen P. G., Heggie D. C., 2012b, MNRAS, 420, 309

Breen P. G., Heggie D. C., 2013a, MNRAS, 432, 2779

Breen P. G., Heggie D. C., 2013b, MNRAS, 436, 584

Buonanno R., Corsi C. E., Buzzoni A., Cacciari C., Ferraro F. R., Fusi Pecci F., 1994, A&A, 290, 69

Cackett E. M. et al., 2006, MNRAS, 369, 407

Capuzzo-Dolcetta R., Vicari A., 2005, MNRAS, 356, 899

Carretta E., Bragaglia A., Gratton R., Lucatello S., 2009a, A&A, 505, 139

Carretta E. et al., 2009b, A&A, 505, 117

Chaboyer B., Demarque P., Kernan P. J., Krauss L. M., 1998, ApJ, 494, 96

Chandrasekhar S., 1943, ApJ, 97, 255

Chandrasekhar S., 1960, Principles of stellar dynamics

Chandrasekhar S., von Neumann J., 1942, ApJ, 95, 489

Chandrasekhar S., von Neumann J., 1943, ApJ, 97, 1

Chatterjee S., Rasio F. A., Sills A., Glebbeek E., 2013a, ApJ, 777, 106

Chatterjee S., Rodriguez C. L., Rasio F. A., 2016, ArXiv e-prints

Chatterjee S., Umbreit S., Fregeau J. M., Rasio F. A., 2013b, MNRAS, 429, 2881

Chernoff D. F., Djorgovski S., 1989, ApJ, 339, 904

Chernoff D. F., Shapiro S. L., 1987, ApJ, 322, 113

Chernoff D. F., Weinberg M. D., 1990, ApJ, 351, 121

Chomiuk L., Strader J., Maccarone T. J., Miller-Jones J. C. A., Heinke C., Noyola

E., Seth A. C., Ransom S., 2013, ApJ, 777, 69

Ciotti L., 2000, Lecture notes on stellar dynamics

Ciotti L., 2010, in American Institute of Physics Conference Series, Vol. 1242, American Institute of Physics Conference Series, Bertin G., de Luca F., Lodato G., Pozzoli R., Romé M., eds., pp. 117–128

Ciotti L., Binney J., 2004, MNRAS, 351, 285

Cohn H., 1980, ApJ, 242, 765

Cohn H., Hut P., Wise M., 1989, ApJ, 342, 814

Contreras Ramos R., Ferraro F. R., Dalessandro E., Lanzoni B., Rood R. T., 2012, ApJ, 748, 91

Dalessandro E., Ferraro F. R., Lanzoni B., Schiavon R. P., O'Connell R. W., Beccari G., 2013a, ApJ, 770, 45

Dalessandro E., Ferraro F. R., Massari D., Lanzoni B., Miocchi P., Beccari G., 2015, ApJ, 810, 40

Dalessandro E. et al., 2013b, ApJ, 778, 135

Dalessandro E., Lanzoni B., Ferraro F. R., Vespe F., Bellazzini M., Rood R. T., 2008, ApJ, 681, 311

Davies M. B., Hansen B. M. S., 1998, MNRAS, 301, 15

Davies M. B., Piotto G., de Angeli F., 2004, MNRAS, 349, 129

Di Cecco A. et al., 2013, AJ, 145, 103

Djorgovski S., 1993, in Astronomical Society of the Pacific Conference Series, Vol. 50, Structure and Dynamics of Globular Clusters, Djorgovski S. G., Meylan G., eds., p. 373

Djorgovski S., King I. R., 1986, ApJL, 305, L61

Djorgovski S., Meylan G., 1994, AJ, 108, 1292

Dotter A., Sarajedini A., Yang S.-C., 2008, AJ, 136, 1407

Dressler A., 1979, ApJ, 231, 659

Drukier G. A., 1996, MNRAS, 280, 498

El-Zant A. A., 2008, ApJ, 681, 1058

Fellhauer M., Kroupa P., Baumgardt H., Bien R., Boily C. M., Spurzem R., Wassmer N., 2000, New Astronomy, 5, 305

Ferraro F. R. et al., 2009, Nature, 462, 1028

Ferraro F. R., Beccari G., Rood R. T., Bellazzini M., Sills A., Sabbi E., 2004, ApJ, 603, 127

Ferraro F. R. et al., 2012, Nature, 492, 393

Ferraro F. R., Lanzoni B., Dalessandro E., Mucciarelli A., Lovisi L., 2015, Blue

Straggler Stars in Globular Clusters: A Powerful Tool to Probe the Internal Dynamical Evolution of Stellar Systems, Boffin H. M. J., Carraro G., Beccari G., eds., p. 99

Ferraro F. R. et al., 1997, A&A, 324, 915

Ferraro F. R., Pecci F. F., Cacciari C., Corsi C., Buonanno R., Fahlman G. G., Richer H. B., 1993, AJ, 106, 2324

Ferraro F. R., Possenti A., Sabbi E., Lagani P., Rood R. T., D'Amico N., Origlia L., 2003a, ApJ, 595, 179

Ferraro F. R. et al., 2006a, ApJL, 647, L53

Ferraro F. R., Sills A., Rood R. T., Paltrinieri B., Buonanno R., 2003b, ApJ, 588, 464

Ferraro F. R., Sollima A., Rood R. T., Origlia L., Pancino E., Bellazzini M., 2006b, ApJ, 638, 433

Fiorentino G., Lanzoni B., Dalessandro E., Ferraro F. R., Bono G., Marconi M., 2014, ApJ, 783, 34

Fukushige T., Ebisuzaki T., Makino J., 1992, PASJ, 44, 281

Fukushige T., Heggie D. C., 1995, MNRAS, 276, 206

Fukushige T., Heggie D. C., 2000, MNRAS, 318, 753

Geller A. M., Mathieu R. D., 2011, Nature, 478, 356

Giersz M., 1998, MNRAS, 298, 1239

Giersz M., Heggie D. C., 1994, MNRAS, 268, 257

Gill M., Trenti M., Miller M. C., van der Marel R., Hamilton D., Stiavelli M., 2008, ApJ, 686, 303

Gilliland R. L., Bono G., Edmonds P. D., Caputo F., Cassisi S., Petro L. D., Saha A., Shara M. M., 1998, ApJ, 507, 818

Gnedin O. Y., Lee H. M., Ostriker J. P., 1999, ApJ, 522, 935

Gnedin O. Y., Ostriker J. P., 1997, ApJ, 474, 223

Goodman J., 1987, ApJ, 313, 576

Gosnell N. M., Mathieu R. D., Geller A. M., Sills A., Leigh N., Knigge C., 2014, ApJL, 783, L8

Gosnell N. M., Mathieu R. D., Geller A. M., Sills A., Leigh N., Knigge C., 2015, ApJ, 814, 163

Gratton R., Sneden C., Carretta E., 2004, ARA&A, 42, 385

Gratton R. G., Fusi Pecci F., Carretta E., Clementini G., Corsi C. E., Lattanzi M., 1997, ApJ, 491, 749

Greengard L., Rokhlin V., 1987, J. Comput. Phys., 73, 325

Greengard L., Rokhlin V., 1997, Acta Numerica, 6, 229

Gürkan M. A., Freitag M., Rasio F. A., 2004, ApJ, 604, 632

Haghi H., Hoseini-Rad S. M., Zonoozi A. H., Küpper A. H. W., 2014, MNRAS, 444, 3699

Heggie D., Hut P., 2003, The Gravitational Million-Body Problem: A Multidisciplinary Approach to Star Cluster Dynamics

Heggie D. C., 1975, MNRAS, 173, 729

Heggie D. C., 2001, in Astronomical Society of the Pacific Conference Series, Vol. 228, Dynamics of Star Clusters and the Milky Way, Deiters S., Fuchs B., Just A., Spurzem R., Wielen R., eds., p. 29

Heggie D. C., 2014, MNRAS, 445, 3435

Heggie D. C., Giersz M., 2008, MNRAS, 389, 1858

Heggie D. C., Mathieu R. D., 1986, in Lecture Notes in Physics, Berlin Springer Verlag, Vol. 267, The Use of Supercomputers in Stellar Dynamics, Hut P., McMillan S. L. W., eds., p. 233

Hénon M., 1961, Annales d'Astrophysique, 24, 369

Hénon M., 1975, in IAU Symposium, Vol. 69, Dynamics of the Solar Systems, Hayli A., ed., p. 133

Hills J. G., 1980, ApJ, 235, 986

Hills J. G., Day C. A., 1976, ApL, 17, 87

Hockney R. W., 1965, J. ACM, 12, 95

Hockney R. W., Eastwood J. W., 1988, Computer simulation using particles

Hurley J. R., Pols O. R., Tout C. A., 2000, MNRAS, 315, 543

Hurley J. R., Sippel A. C., Tout C. A., Aarseth S. J., 2016, PASA, 33, e036

Hurley J. R., Tout C. A., Pols O. R., 2002, MNRAS, 329, 897

Hut P., Murphy B. W., Verbunt F., 1991, A&A, 241, 137

Joshi K. J., Rasio F. A., Portegies Zwart S., 2000, ApJ, 540, 969

Kalirai J. S., Richer H. B., 2010, Philosophical Transactions of the Royal Society of London Series A, 368, 755

Kashlinsky A., 1987, ApJ, 312, 497

Khalisi E., Amaro-Seoane P., Spurzem R., 2007, MNRAS, 374, 703

Kim W.-T., El-Zant A. A., Kamionkowski M., 2005, ApJ, 632, 157

King I. R., 1966, AJ, 71, 64

Kirsten F., Vlemmings W., Freire P., Kramer M., Rottmann H., Campbell R. M., 2014, A&A, 565, A43

Knigge C., Leigh N., Sills A., 2009, Nature, 457, 288

Kroupa P., 2001, MNRAS, 322, 231

Kulkarni S. R., Hut P., McMillan S., 1993, Nature, 364, 421

Küpper A. H. W., Maschberger T., Kroupa P., Baumgardt H., 2011, MNRAS, 417, 2300

Lanzoni B., Dalessandro E., Ferraro F. R., Miocchi P., Valenti E., Rood R. T., 2007a, ApJL, 668, L139

Lanzoni B., Ferraro F. R., Alessandrini E., Dalessandro E., Vesperini E., Raso S., 2016, ApJ Submitted

Lanzoni B. et al., 2007b, ApJ, 663, 1040

Larson R. B., 1970a, MNRAS, 147, 323

Larson R. B., 1970b, MNRAS, 150, 93

Lee E. P., 1969, ApJ, 155, 687

Leigh N., Knigge C., Sills A., Perets H. B., Sarajedini A., Glebbeek E., 2013, MNRAS, 428, 897

Leigh N., Sills A., Knigge C., 2007, ApJ, 661, 210

Leigh N., Sills A., Knigge C., 2011, MNRAS, 415, 3771

Lovisi L. et al., 2010, ApJL, 719, L121

Lovisi L., Mucciarelli A., Lanzoni B., Ferraro F. R., Gratton R., Dalessandro E., Contreras Ramos R., 2012, ApJ, 754, 91

Lynden-Bell D., Eggleton P. P., 1980, MNRAS, 191, 483

Lynden-Bell D., Wood R., 1968, MNRAS, 138, 495

Maccarone T. J. et al., 2016, MNRAS, 458, 3633

Mackey A. D., Wilkinson M. I., Davies M. B., Gilmore G. F., 2007, MNRAS, 379, L40

Mackey A. D., Wilkinson M. I., Davies M. B., Gilmore G. F., 2008, MNRAS, 386, 65

Makino J., 1996, in IAU Symposium, Vol. 174, Dynamical Evolution of Star Clusters: Confrontation of Theory and Observations, Hut P., Makino J., eds., p. 151

Makino J., Taiji M., 1998, Scientific Simulations with Special-Purpose Computers–the GRAPE Systems. p. 248

Mapelli M., Ripamonti E., Battaglia G., Tolstoy E., Irwin M. J., Moore B., Sigurdsson S., 2009, MNRAS, 396, 1771

Mapelli M., Sigurdsson S., Colpi M., Ferraro F. R., Possenti A., Rood R. T., Sills A., Beccari G., 2004, ApJL, 605, L29

Mapelli M., Sigurdsson S., Ferraro F. R., Colpi M., Possenti A., Lanzoni B., 2006, MNRAS, 373, 361

Marín-Franch A. et al., 2009, ApJ, 694, 1498

Mastrobuono-Battisti A., Capuzzo-Dolcetta R., 2012, in Astronomical Society of the Pacific Conference Series, Vol. 453, Advances in Computational Astrophysics: Methods, Tools, and Outcome, Capuzzo-Dolcetta R., Limongi M., Tornambè A., eds., p. 237

Mathieu R. D., Geller A. M., 2009, Nature, 462, 1032

McCrea W. H., 1964, MNRAS, 128, 147

Meylan G., Heggie D. C., 1997, A&ARv, 8, 1

Miller-Jones J. C. A. et al., 2015, MNRAS, 453, 3918

Milone A. P. et al., 2008, ApJ, 673, 241

Milone A. P. et al., 2012, A&A, 540, A16

Milosavljević M., Merritt D., 2001, ApJ, 563, 34

Miocchi P. et al., 2013, ApJ, 774, 151

Miocchi P., Pasquato M., Lanzoni B., Ferraro F. R., Dalessandro E., Vesperini E., Alessandrini E., Lee Y.-W., 2015, ApJ, 799, 44

Monelli M. et al., 2012, ApJ, 744, 157

Moody K., Sigurdsson S., 2009, ApJ, 690, 1370

Moretti A., de Angeli F., Piotto G., 2008, A&A, 483, 183

Morscher M., Pattabiraman B., Rodriguez C., Rasio F. A., Umbreit S., 2015, ApJ, 800, 9

Morscher M., Umbreit S., Farr W. M., Rasio F. A., 2013, ApJL, 763, L15

Mucciarelli A., Lovisi L., Ferraro F. R., Dalessandro E., Lanzoni B., Monaco L., 2014, ApJ, 797, 43

Murphy B. W., Cohn H. N., Durisen R. H., 1991, ApJ, 370, 60

Nipoti C., Ciotti L., Binney J., Londrillo P., 2008, MNRAS, 386, 2194

Nipoti C., Treu T., Ciotti L., Stiavelli M., 2004, MNRAS, 355, 1119

Nitadori K., Aarseth S. J., 2012, MNRAS, 424, 545

O'Leary R. M., Rasio F. A., Fregeau J. M., Ivanova N., O'Shaughnessy R., 2006, ApJ, 637, 937

Ostriker E. C., 1999, ApJ, 513, 252

Ostriker J. P., Tremaine S. D., 1975, ApJL, 202, L113

Peuten M., Zocchi A., Gieles M., Gualandris A., Hénault-Brunet V., 2016, MNRAS, 462, 2333

Pfahl E., Rappaport S., Podsiadlowski P., 2002, ApJ, 573, 283

Piotto G., 2015, IAU General Assembly, 22, 2225260

Piotto G. et al., 2007, ApJL, 661, L53

Piotto G. et al., 2004, ApJL, 604, L109

Plummer H. C., 1911, MNRAS, 71, 460

Podsiadlowski P., Pfahl E., Rappaport S., 2005, in Astronomical Society of the Pacific Conference Series, Vol. 328, Binary Radio Pulsars, Rasio F. A., Stairs I. H., eds., p. 327

Portegies Zwart S. F., Hut P., Makino J., McMillan S. L. W., 1998, A&A, 337, 363

Renzini A., Fusi Pecci F., 1988, ARA&A, 26, 199

Repetto S., Davies M. B., Sigurdsson S., 2012, MNRAS, 425, 2799

Salmon J. K., Warren M. S., 1994, Journal of Computational Physics, 111, 136

Sandage A. R., 1953, AJ, 58, 61

Sanna N., Dalessandro E., Ferraro F. R., Lanzoni B., Miocchi P., O'Connell R. W., 2014, ApJ, 780, 90

Sarajedini A. et al., 2007, AJ, 133, 1658

Shara M. M., Saffer R. A., Livio M., 1997, ApJL, 489, L59

Sigurdsson S., Davies M. B., Bolte M., 1994, ApJL, 431, L115

Sigurdsson S., Hernquist L., 1993, Nature, 364, 423

Sills A., Glebbeek E., Chatterjee S., Rasio F. A., 2013, ApJ, 777, 105

Sills A., Karakas A., Lattanzio J., 2009, ApJ, 692, 1411

Simunovic M., Puzia T. H., 2014, ApJ, 782, 49

Simunovic M., Puzia T. H., 2016, MNRAS, 462, 3401

Simunovic M., Puzia T. H., Sills A., 2014, ApJL, 795, L10

Sippel A. C., Hurley J. R., 2013, MNRAS, 430, L30

Sollima A., Lanzoni B., Beccari G., Ferraro F. R., Fusi Pecci F., 2008, A&A, 481, 701

Spitzer L., 1987, Dynamical evolution of globular clusters

Springel V., Yoshida N., White S. D. M., 2001, New Astronomy, 6, 79

Spurzem R., 1999, Journal of Computational and Applied Mathematics, 109, 407

Strader J., Chomiuk L., Maccarone T. J., Miller-Jones J. C. A., Seth A. C., 2012, Nature, 490, 71

Takahashi K., Portegies Zwart S. F., 2000, ApJ, 535, 759

Thorne R. M., 1968, ApJ, 151, 671

Tian B., Deng L., Han Z., Zhang X. B., 2006, A&A, 455, 247

Tremaine S., Weinberg M. D., 1984, MNRAS, 209, 729

Tremaine S. D., Ostriker J. P., Spitzer, Jr. L., 1975, ApJ, 196, 407

Trenti M., Ardi E., Mineshige S., Hut P., 2007, MNRAS, 374, 857

Trenti M., Hut P., 2008, ArXiv e-prints

Trenti M., Vesperini E., Pasquato M., 2010, ApJ, 708, 1598

VanDalfsen M. L., Harris W. E., 2004, AJ, 127, 368

Vecchio A., Colpi M., Polnarev A. G., 1994, ApJ, 433, 733

Vesperini E., 2010, Philosophical Transactions of the Royal Society of London Series A, 368, 829

Vesperini E., Heggie D. C., 1997, MNRAS, 289, 898

Vesperini E., McMillan S. L. W., Portegies Zwart S., 2009, ApJ, 698, 615

von Hoerner S., 1960, Z. Astrophys., 50

Wang S., Ma J., 2013, AJ, 146, 20

White M. L., 1949, ApJ, 109, 159

White S. D. M., 1976, MNRAS, 174, 19

Wilson C. P., 1975, AJ, 80, 175

Xin Y., Ferraro F. R., Lu P., Deng L., Lanzoni B., Dalessandro E., Beccari G., 2015, ApJ, 801, 67

Zinn R., 1985, ApJ, 293, 424

Zinn R., Searle L., 1976, ApJ, 209, 734

List of Figures and Tables